Heat Transfer Enhancements Using Laminate Film Encapsulation for Phase Change Heat Storage Materials

by

Louis Desgrosseilliers

Submitted in partial fulfilment of the requirements
for the degree of Master of Applied Science

at

Dalhousie University
Halifax, Nova Scotia
July 2012

DALHOUSIE UNIVERSITY

DEPARTMENT OF MECHANICAL ENGINEERING

The undersigned hereby certify that they have read and recommend to the Faculty of Graduate Studies for acceptance a thesis entitled “Heat Transfer Enhancements Using Laminate Film Encapsulation for Phase Change Heat Storage Materials” by Louis Desgrosseilliers in partial fulfilment of the requirements for the degree of Master of Applied Science.

Dated: July 27, 2012

Co-Supervisors: _____

_____

Readers: _____

_____

DALHOUSIE UNIVERSITY

DATE: July 27, 2012

AUTHOR: Louis Desgrosseilliers

TITLE: Heat Transfer Enhancements Using Laminate Film Encapsulation for Phase Change Heat Storage Materials

DEPARTMENT OR SCHOOL: Department of Mechanical Engineering

DEGREE: MASc CONVOCATION: October YEAR: 2012

_____

Signature of Author

TABLE OF CONTENTS

LIST OF TABLES

LIST OF FIGURES

ABSTRACT

A model is proposed to predict the heat spreading behaviour experienced by laminate materials when heated over only a part of the domain, which is broken up into two regions, known as the heated and fin regions. The 2D, steady-state, two-region fin model is unique in its treatment of multilayer conduction heat transfer, giving the exact solution in the heat-spreading layer only, in both Cartesian and cylindrical coordinates. The experimentally and numerically validated two-region fin model can help designers to assess improved heat transfer rates for laminate pouches for use to encapsulate supercooled salt hydrate phase change materials for long-term heat storage. Waste aseptic cartons (e.g. Tetra Brik) are a potentially useful resource for making laminate heat storage pouches since value-added end-uses are largely absent in Canada and in many other countries. The model is also useful for assessing improved temperature uniformity in heat spreading devices with applied heat fluxes.

LIST OF SYMBOLS USED

Dimensional variables

A	Surface area (m^2)
$\dot{A}$	Surface area rate of growth ($m^2\ s^{-1}$)
C_1	Coefficient of the complementary solution
C_2	Coefficient of the complementary solution
C_3	Coefficient of the particular solution
C_4	Coefficient of the particular solution
C_5	Coefficient of the particular solution
C_p	Heat capacity ($kJ\ kg^{-1}$)
dT_V	Contribution to the differential dT from V, $(\partial T/\partial V)dV$ (K)
dT_{Tinf}	Contribution to the differential dT from T_{inf}, $(\partial T/\partial T_{inf})dT_{inf}$ (K)
dT_{t1}	Contribution to the differential dT from t, $(\partial T/\partial t)dt$ (K)
dT_{t2}	Contribution to the differential dT from t_2, $(\partial T/\partial t_2)dt_2$ (K)
dT_x	Contribution to the differential dT from x, $(\partial T/\partial x)dx$ (K)
dT_r	Contribution to the differential dT from r, $(\partial T/\partial r)dr$ (K)
dT_L	Contribution to the differential dT from L, $(\partial T/\partial L)dL$ (K)
$\dot{E}$	System thermal energy accumulation (W)
h	Convection heat transfer coefficient ($W\ m^{-2}\ K^{-1}$)
h_h	Natural convection heat transfer coefficient in the heated region only ($W\ m^{-2}\ K^{-1}$)
h_f	Natural convection heat transfer coefficient in the fin region only ($W\ m^{-2}\ K^{-1}$)
k	Thermal conductivity ($W\ m^{-1}\ K^{-1}$)
L	Heated boundary length at $x,r = 0$ (m)
$\dot{L}$	Heated boundary length rate of growth ($m\ s^{-1}$)
M	Salt hydrate cation
n	Number of waters of hydration
P	Heater rated power ($W\ m^{-2}$)
q_o''	Applied finite heat flux ($W\ m^{-2}$)
Q_{fin}	Rate of fin region heat transfer (Heat transfer rate in the fin region, W)

Q_{lam}	Laminate body rate of heat transfer (W)
Q_{simple}	Rate of heat transfer of laminate body without heat spreading layer (W)
r	Radial position (m)
R	Thermal resistance above the highly conductive metal core (m^2 K W^{-1})
R_3	Thermal resistance below the highly conductive metal core (m^2 K W^{-1})
R_h	Heated region thermal resistance above the highly conductive metal core (m^2 K W^{-1})
R_f	Fin region thermal resistance above the highly conductive metal core (m^2 K W^{-1})
t	Layer thickness (m)
T	Temperature (K)
T_i	Applied temperature heat source (K)
T_{inf}	Free stream temperature (K)
T_m	Equilibrium melting temperature (K)
T_{sup}	Supercooled temperature (K)
T_o	Boundary temperature at $x,r = L$ (K)
V	Heater operating voltage (V)
x	Cartesian axial position (m)
Y	Salt hydrate anion

Greek symbols

α	Heated region constant (m^{-1})
β	Heated region particular solution (K)
ΔT	Variable substitution for the applied temperature driving force (K)
γ	Fin region constant (m^{-1})
λ	Dimensionless position
η	Heat transfer effectiveness
ρ	Density (kg m^{-3})
τ	Dimensionless temperature
Ω_α	Dimensionless thermal resistance factor in the heated region
Ω_γ	Dimensionless thermal resistance factor in the fin region

Ω_κ	Dimensionless thermal resistance ratio of the bottom and upper layers
ϕ_o	Variable substitution for T_o in the fin region (K)
θ_o	Variable substitution for T_o in the heated region (K)

Subscripts

ave	Mixture average property
axial	Axial path (*x* or *r* axis) for heat conduction
c	Complementary solution to the ODE
p	Particular solution to the ODE
planar	Planar normal path for heat conduction (*y* or *z* axis)
sat	Saturated conditions in the fin region
1	High conductivity metal core
2	Top thermally resistive layer
3	Bottom thermally resistive layer

Superscript

’	Linear flux

ACKNOWLEDGEMENTS

First and foremost, I thank my partner, Jill, for leaving our home in Toronto to start a new life in Nova Scotia on the single prospect that I would be a graduate student. Without her, I would have been a miserable mess all this time. Our cats, Rocky, George, Bridget, and Blacky all remind me how my time is best served lavishing them with attention, so thank you all.

I am also grateful for the continued love and support from my parents who welcomed us to Halifax in 2010. My dad even agreed to assist me in the lab a few times this year. Although Pete, the beagle, is no longer with us, I do remember his occasional, but very eager, companionship with warm feelings.

Dominic and Mary Anne, thank you both for your guidance these past two years and your continued support to supervise my upcoming PhD enrolment. Also, thanks to my committee members, Dr. Swan and Dr. Watts.

Thanks to all of my office mates in both labs: Robynne, Chang, Ben, Farid, Gina, Cathy, Paul, Alex, Carl (and Courtney), Kim, and Mike. Thanks to Rachael and Dylan for their hospitality and friendship, as well as Hesam for his enduring friendship and much needed quarterly squash matches!

I am very lucky to have received assistance in the lab from Mohktar, whose help was instrumental in completing my work. Thanks to his supervisors, Dr. Warkentin and Dr. Bauer, for letting him set me up with their IR camera. I am also very grateful for the opportunity awarded to me from RRFB Nova Scotia, with a special thanks to Brennan Gillis. Their funding programme helped me explore the material reclamation aspect to my work and interact with industry experts on my trip to Piracicaba, Brazil. Of course, thanks to my hosts in Brazil, starting with Christiane Paiva and her colleagues at Klabin, but also Tetra Pak Brazil, and EET.

A special thanks to Gary Zakaib, whose mentoring at AECL did well to prepare me for graduate studies, but also to care deeply about my overall contributions to the engineering profession. It is that which motivates me to teach young undergraduate engineers here at Dalhousie.

Thanks also to the Mechanical Engineering Office at Dalhousie University: Michelle, Morgyn, and formerly, Sandra. Another thanks goes out to Janet at DREAMS and my DREAMS colleagues, DREAMS professors, and for the funding awarded to me from the DREAMS program.

CHAPTER 1: INTRODUCTION

1.1 BACKGROUND AND MOTIVATION

Space heating has long remained the dominant end-use for domestic energy consumption in Canadian homes; it has accounted for 54.6% of all domestic energy consumption in the period of 1990 to 2009 (NRCAN, 2012). The proportion of home energy use is larger still when one includes the domestic hot water heating over the same period, totalling 71.0% (NRCAN, 2012). This combined value is representative of Canadian homes that use combined domestic hot water/hot water radiant heating (or steam radiant heating), accounting for 51 and 24% of all homes in Prince Edward Island and Nova Scotia in 2007 (Statistics Canada, 2010), respectively. Although consistent in a proportional sense, domestic space heating has increased by 12% (NRCAN, 2012) over the entire period, a change equal to 100 PJ (peta = 10^{18}) (NRCAN, 2012), but keeping pace with a national population growth rate of ~16% over the same period (Statistics Canada, 2008).

Such increases in home heating energy consumption invariably cause the national emissions of greenhouse gases to increase, since 63% of all home space heating is derived from the direct combustion of hydrocarbon fuels (Statistics Canada, 2010). This contribution becomes more acute when also considering the indirect combustion of hydrocarbons in thermal electricity generation in Canada, equal to 25.3% in 2007 (Statistics Canada, 2009).

The volatility of fuel prices in the global market makes households using hydrocarbon fuel sources for heating particularly vulnerable, made apparent by the energy crisis of the 1970s (Lane, 1983, 1985). Furthermore, net imports of energy resources puts citizens at particular risk of supply disruptions, making heat a topic of national security. Naturally, research into materials for heat storage and heat storage systems, and the deployment of solar heating technologies has intensified in Nordic countries (Wettermark et al., 1979) and large import markets for hydrocarbon fuels (Lane, 1983) since the 1970s. Net energy importing regions, such as Nova Scotia, have also intensified their solar heating deployment in homes and institutions using incentive programmes and initiatives such as the Solar City initiative in Halifax, NS (Halifax Regional Municipality, 2012).

Conventional domestic solar hot water (DSHW) heating utilizes heat collection in panels (either flat plate or evacuated tube (Bédard and Leduc, 2011)) and stores heat in a sensible heat storage material (e.g. water, rock, or brick (Farid et al., 2004; Pinel et al., 2011)) by heat exchange with the collection panel fluid. Typical installations using water tanks utilize only short-term heat stores (Bédard and Leduc, 2011; Desgrosseilliers et al., 2011; Hirano and Saitoh, 2002a, 2002b, 2009; Murray et al., 2011; Pinel et al., 2011) and can only satisfy a fraction of the hot water heating needs (called solar fraction). Bédard and Leduc (2011) reported a maximum of 50% solar fraction during cold winter periods for domestic hot water consumption and an average solar fraction of < 38% for various installation types. They also found that during periods of severe system underutilization, such as would be experienced during long summer absences, the hot water storage tank fails to provide enough heat dissipation from the solar collectors, causing the glycol in the heat exchange fluid to degrade due to elevated temperatures (Bédard and Leduc, 2011). The maximum short-term utilization (i.e., diurnal) for space heating is generally considered to be around 50% (Pinel et al., 2011).

Increasing heat stores using sensible heat storage materials requires excessively large volumes (Scotian Windfields, 2009; Hirano and Saitoh, 2002a, 2002b), which often challenges the integrity of support structures in retrofitted buildings (Desgrosseilliers et al., 2011; Murray et al., 2011). Although more efficient with respect to heat transfer processes at relatively constant temperature and significantly reduced storage volume (Desgrosseilliers et al., 2011; Farid et al., 2004; Lane, 1983, 1980, 1985; Hirano and Saitoh, 2002a, 2002b; Murray et al., 2011; Wettermark et al., 1979), phase change materials (PCMs) used for latent heat storage are also only typically used for short-term heat storage (e.g. days) due to insulation requirements to maintain the heat stores (Pinel et al., 2011; Hirano and Saitoh, 2009). PCMs encompass materials that undergo reversible equilibrium phase-change processes in which there is only small volume change: these can be solid-liquid, and solid-solid systems. Consequently, the properties of numerous PCMs have been catalogued in several books and reviews (Abhat, 1983; Agyenim et al., 2010; Farid et al., 2004; Garg et al., 1985; Kenisarin and Makhamov, 2007; Khudhair and Farid, 2004; Lane, 1983; Zalba et al., 2003).

Long-term heat storage (including seasonal heat storage) can theoretically provide improved solar heat utilization over short-term storage (i.e., larger solar fraction of home heating needs) (Drake Landing Solar Community, 2012; Pinel et al., 2011; Wettermark et al., 1979) and decrease the required collector area (Pinel et al., 2011). The nature of long-term heat storage (LTHS) itself diminishes the requirement for high heat collection rates and reduces the required collector area, since the collection of heat is completely decoupled from its consumption. Due to the self-discharging characteristics of conventional sensible and latent heat storage materials, only large-scale, long-term, heat storage systems are ever practical using these materials (Pinel et al., 2011). The borehole thermal storage system at Drake Landing Solar Community (Drake Landing Solar Community, 2012; Pinel et al., 2012) is one example of successful implementation of long-term sensible heat storage, capable of achieving an 85.6% solar fraction after 4 years of operation (designed for 90% after 5 years) (Drake Landing Solar Community, 2012; Sibbit et al., 2011).

A more fitting technology for LTHS might be one that requires no insulation at all, making this type of heat storage more akin to electrical energy storage in electrochemical cells. Supercooled salt hydrates can perform this task since they can exist below their equilibrium freezing point temperature[1] in a metastable, supersaturated, liquid state (Araki et al., 1995; Lane, 1983), effectively storing latent heat at room temperature or even at much lower temperature with delayed heat release for months or even years (Hirano and Saitoh, 2002a, 2002b, 2009; Pinel et al., 2011; Sandnes, 2003; Wei and Ohsasa, 2010). Figure 1.1 shows the typical enthalpy (stored energy) temperature profile for a congruent melting salt hydrate that is nucleated after 33˚C of supercooling, indicating the separate paths of melting, supercooling (metastable liquid), and nucleation.

[1] Salt hydrates are often considered incongruent melting systems, especially if unrecoverable anhydrous formation at the peritectic point is to be avoided (Lane, 1983; Sandnes, 2003).

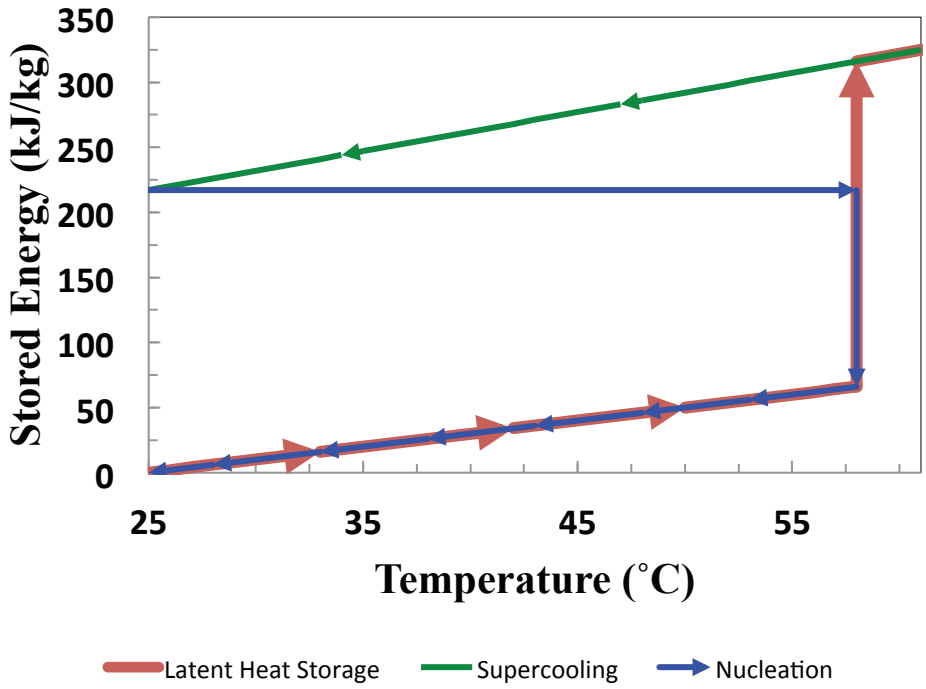

Figure 1.1: Enthalpy-temperature profile for a congruent melting salt hydrate with nucleation initiated after 33˚C of supercooling.

Hirano and Saitoh (2009) performed long-term heat storage experiments and reported 48.8% recovery of the total heat stored (latent and sensible heats) in disodium hydrogen phosphate dodecahydrate after 204 days. The PCM heat storage was initially heated to 65.9˚C and allowed to cool to 22.5˚C (room temperature), while the PCM's equilibrium freezing temperature is 35.5˚C (Hirano and Saitoh, 2009). Just pertaining to the amount of latent heat storage in their experiments, Hirano and Saitoh (2009) show data suggesting a recovery around 76% of the stored latent heat with 13˚C of supercooling. Sandnes (2003) also explained the principle that each supercooled salt hydrate PCM has an optimal range of supercooling for useful heat recovery, since some latent heat is always consumed to simply elevate the temperature of the PCM to its equilibrium freezing temperature (equal to the sensible heat lost to the surroundings during supercooling). The inherent ability to store heat in supercooled salt hydrates at ambient conditions could open new avenues for heat storage, whereby the storage and consumption of heat would be completely decoupled by utilizing large-scale heat storage operations (i.e., solar farms) and local delivery of modular heat stores to clients.

For every heat storage material, packaging or encapsulation is essential in every application, differing in scale (macro, micro, and bulk) and in some of its functions. For instance, microencapsulation is used to disperse a heat storage material in a carrier solid to obtain high surface area for improved heat transfer (Lane, 1985). Macroencapsulation can include long tubes of polymer or metal, small spheres, or panels to be used in modular heat storage systems (Lane, 1985). Bulk encapsulation includes all forms of tank storage for the simplest, yet robust designs (Lane, 1985). Design requirements for encapsulation must address mechanical durability and integrity (leak proof), good heat transfer characteristics, vapour impermeability, and chemical compatibility (Lane, 1980, 1985).

Supercooled salt hydrate PCMs for LTHS behave fundamentally different from all other conventional PCMs and consequently impose different encapsulation requirements than do conventional PCMs and sensible heat storage materials. Their transition from solid to liquid resembles a chemical process (Garg et al., 1985) rather than a strict physical change, as the solid decomposes at an elevated temperature and the anhydrous salt dissolves, though not always completely[2], in its own water of hydration:

$$MY \cdot n\mathrm{H_2O(s)} \leftrightharpoons MY(\mathrm{aq}) + n\mathrm{H_2O(l)}\ , \qquad (1.1)$$

where M represents the salt hydrate cation, Y the anion, and n is the number of waters of hydration. To extract the heat when desired, solidification is initiated using a nucleation trigger (Anthony et al., 1990; Sandnes, 2003, 2008), and proceeds in two steps: first, the PCM rapidly nucleates and exothermically raises its temperature to the melting point (panels 1 and 2 in Fig.1.2), then solidification continues only as quickly as heat is extracted to the outside (panels 3 and 4 in Fig.1.2) (Hirano and Saitoh, 2002a, 2002b, 2009; Sandnes, 2003), provided that the process is not limited by the rate of crystallization[3]. This behaviour introduces yet another design requirement for encapsulation of these materials: incorporation of a solidification trigger (often a flexible, scored metal disk or a stiff spring retaining stable solid crystals in high pressure contact junctions (Sandnes, 2003, 2008; Yang, 2001)).

[2] Peritectic salt hydrate systems do not dissolve completely in the water of hydration, so the extra water method is usually used to promote complete dissolution (Sandnes, 2003).
[3] Salt hydrate PCMs have been typically selected on the basis of rapid crystallization (Lane, 1983).

Figure 1.2: Solidification of supercooled $NaCOOH \cdot 3H_2O$ with nucleation initiated through the capillary at the top of the container using a seed crystal of the same material (courtesy of Sandes (2003)).

Except for some stainless steels, metal encapsulation is generally incompatible with salt hydrate PCMs (salt hydrates are corrosive to most metals) (Lane, 1985) and typical rigid plastics cannot easily accommodate a solidification trigger, which must be externally activated. Although largely unexplored for long-term heat storage PCM encapsulation, laminated pouches of plastic and metal foil seem to satisfy all of the design requirements and are flexible enough to incorporate a solidification trigger. Laminate packaging, that is to say layered materials made of PE/Al (PE = polyethylene and sometimes polyester, Al = aluminium), are used in many food storage solutions and represent an important source of material waste. Although they do not account for much of the mass sent to landfills (< 0.1 wt% of packaging waste in the US in 1992 (Stessel, 1996)), they represent a significant investment in the embodied energy of materials. It would be advantageous to reclaim these waste materials for heat storage encapsulation.

Beyond the added requirement to incorporate a seed trigger for supercooled salt hydrate PCMs for LTHS, improvement in the rate of heat transfer during discharge from PCMs is a very desirable quality in an encapsulation technology (Lane, 1985). Numerous attempts have been made to enhance the heat discharge rate during conventional PCM solidification using fins and highly dispersed materials (Desgrosseilliers et al., 2011; Kenisarin and Mahkamov, 2007; Murray et al., 2011; Ogoh, 2010). However, these

designs are not well suited for supercooled salt hydrate encapsulations since fins are primarily incorporated into bulk encapsulation (large inventories risk spontaneous nucleation of supercooled salt hydrates and the unintended loss of heat stores) and micro-encapsulation dispersion could not accommodate individual seed triggers with external activation.

The opportunity for heat transfer enhancements in supercooled salt hydrate PCM LTHS could actually come from their distinctive feature, triggered nucleation. That is to say, a successful heat transfer enhancement technology should be adapted, even optimized, using this process. Heat spreading, as it is commonly called, occurs in layered composite bodies such as in multi-ply cookware (Groll, 2001, 2005; Woolf, 1985) and in electronics cooling devices and is the process by which two paths for heat conduction are at play (Haji-Sheikh et al., 2002, 2003): heat conduction either occurs in the surface normal direction of the heated contact (through the layered body) or parallel to the composite layers (then dissipated in the surface normal direction, similar to fin heat transport). Therefore, with careful design considerations, a supercooled salt hydrate PCM LTHS encapsulation could improve the rate of heat transfer during discharge by passive heat spreading wherever nucleation sites are present. In fact, laminated pouches, such as layered PE/Al encapsulation mentioned above, could substantially improve the discharge heat transfer rate in supercooled salt hydrate solutions as well as provide a very suitable encapsulation material for LTHS PCMs.

1.2 TOPICAL REVIEW

1.2.1 PCM ENCAPSULATION

Lane (1985) emphasizes the importance and care of PCM encapsulation selection and how it is essential to commercial success. He describes the primary qualities that are required from encapsulation technologies: mechanical durability and integrity, good heat transfer, chemical compatibility, and vapour impermeability (Lane, 1980, 1985), with added considerations to cost and ease of manufacture (Lane et al., 1978).

Conventional packaging laminates (thermoplastic and metal foil) can add heat transfer enhancements to some of the emerging, novel heat-storage technologies using phase change materials. Metallized foil packaging is widely used in low-cost, lightweight, food and electronics packaging due to their good shape conformability and

excellent barrier properties (Carton Council of Canada, 2012; Elopak, 2009; Lane et al., 1978; Stessel, 1996; Tetra Pak, 2011). Lane (1978, 1980, 1985) reported promising characteristics for 0.18 mm thick laminated polyethylene/Al/polyester (76 μm/89 μm/13 μm layers, respectively) pouches as salt hydrate PCM encapsulation for heat exchange with air. Furbo and Schultz (2007) used 0.113 mm thick laminated pouches (9 μm thick Al foil) for their LTHS PCM experiments (using supercooled $NaCOOH•3H_2O$). Lane (1985) neglected considerations of any enhancements from the laminated film since the heat transfer medium, air, was the limiting factor and the PCMs under study were only of the conventional, non-supercooling kind, while Furbo and Schultz (2007) made their selection based on flexibility and shelf stability alone.

Although Lane (1978) reported on the mechanical and bulk thermal and physical properties of the 0.18 mm laminate pouch (R-2 retort pouch used in military ration packaging) used in PCM heat-storage testing, there have been no studies of the potential heat transfer benefits they could offer to supercooled salt hydrate solutions used in PCM LTHS systems. In fact, other PCM LTHS experiments using supercooled salt hydrates have used either bulk or microencapsulated PCM in rigid plastic (Hirano and Saitoh, 2002b, 2009) and have not sought improvements to the heat transfer rate during discharge by heat spreading. The current research aims to address this point by demonstrating the conduction mechanism by which laminate films can enhance the heat transfer rate from encapsulated supercooled salt hydrate PCMs.

1.2.2 LAMINATE HEAT CONDUCTION

Overall, the use of laminates (layered composites) is extensive for the preservation of product shelf life. In one other application, mainly stovetop cookware fabrication, the laminates in question are composed of outer layers of tough, corrosion-resistant, but typically low thermal conductivity metals (e.g. stainless steels) with inner layers (sometimes up to 9 layers in total) of highly conductive metals, e.g. copper (Cu) or Al (Groll, 2001, 2005; Woolf, 1985). Considering their heat transfer characteristics, there are other applications that could benefit from using laminate materials.

As an illustration of laminate heat transfer, cookware is available in an assortment of multi-ply designs with the aim of improving the temperature uniformity of the cooking surface on what are otherwise non-uniform heat sources. These range from ceramic coil

heating elements to halogen lamps, wood fire, propane or natural gas burners, and now induction elements. Hot spots cause food to burn or stick, and significant cookware overheating causes irreparable damage resulting from non-uniform thermal expansion of the various metals (Groll, 2001, 2005; Woolf, 1985). Temperature uniformity is made possible through the careful combination of the wear resistant, but low thermal conductivity outer layers with highly conducting inner layers, a technique that is primarily represented by cookware patents (Groll, 2001, 2005; Woolf, 1985). These cookware patents suggest that while the outermost layer becomes quickly saturated by carrying heat from the heating element to the cooking surface in the direction of the surface normal, the better conducting inner layers can convey excess heat from the source in the transverse direction (heat spreading), resulting in heating more of the upper surface than what was directly overtop the heat source (Groll, 2001, 2005; Woolf, 1985).

On the other hand, theoretical and numerical models of heat spreading behaviour in electronics cooling devices and multilayer metal mirrors used in lasers have been presented in the literature. Heat transfer studies concerning composite materials have been largely motivated by fibre-reinforced composites (Matysiak and Woźniak, 1984), two-layered heat sinks for electronics cooling (Haji-Sheikh et al., 2002, 2003), volumetric heating and fuel simulation (Singh et al., 2008; Sun and Wichman, 2004), and femto to nanosecond laser pulse heating of multilayer Au mirrors (Karakas et al., 2010; Liu, 2007; Naqavi et al., 2005). Some salient points are:

1. Applications of layered metals have been considered at the near exclusion of polymers or other thermally resistive layers;
2. Laser pulses only apply to extreme local heat fluxes (Karakas et al., 2010; Liu, 2007; Naqavi et al., 2005);
3. Researchers have been motivated by the thermal stress and contact resistance between dissimilar metals (Haji-Sheikh et al., 2003; Naqavi et al., 2005), less so for the heat transfer attributes alone;
4. The solutions presented for electronics cooling are too inclusive of all manner of non-uniform heat sources and all of the material domains. These solutions are too complex for most common applications, i.e. eigenvalues must be

computed for series solutions and triple integrals solved for the source terms (Haji-Sheikh et al., 2002, 2003);

5. The most fundamental solutions only considered uniform boundary conditions and solutions spanning the planar normal direction (de Monte, 2002; Singh et al., 2008; Sun and Wichman, 2004).

These studies have only looked at the solutions to the temperature profiles (interested mainly in temperature uniformity and locating hot spots) and have not identified the benefit of increased heat transfer rate in supercooled phase change systems.

Although the solutions for bi-layered metallic bodies presented by Haji-Sheikh, Beck (2002), and Agonafer (2003) have left the exact distribution of the heat source unspecified so that all possible distributions, including circular ones, could be incorporated, their solutions were only formulated in Cartesian coordinates, thus making it difficult to adapt the math for cylindrical coordinates. Only Singh, Jain, and Rizwan-uddin (2008) and de Monte (2002) have obtained 1D solutions to layered bodies in cylindrical coordinates, however, neither group has considered non-uniform boundary conditions and the layers alternated in the radial direction.

For the purposes of modelling the conduction heat transfer in laminate encapsulation for supercooled salt hydrate PCMs, iterative approaches should not be required to achieve a correct solution, the equations should all be explicit, and the model equations should be derived in both Cartesian and cylindrical coordinates in order to adapt easily to the desired situation. Since the other models presented in the literature do not fit these criteria, the current research proposes a laminate heat conduction model that does; it might also find application in heat transfer modelling for cookware and electronics cooling.

1.2.3 LAMINATE FILM RECLAMATION

Amongst the existing packaged materials containing laminated PE/Al, aseptic carton waste (e.g. Tetra Pak, Elopak, and Combibloc) appears to be the most suitable for immediate exploitation. These waste items have collection/sorting systems already in place in Nova Scotia, and throughout many other jurisdictions in Canada, the US, South America, Europe, and Asia (Abreu, 2000; Carton Council of Canada, 2012; Elopak, 2008; Pedroso and Bastos, 2006; Tetra Pak, 2011). The recycling rate of aseptic cartons

worldwide is 20% (Tetra Pak, 2011); 38% (Carton Council of Canada, 2012) and 23% (Pedroso and Bastos, 2006) in Canada (2011) and Brazil (2005), respectively, with global annual raw material consumption exceeding 0.75 Mt (Tetra Pak, 2011). While the laminate in aseptic cartons only accounts for ~26% of the mass on average (Carton Council of Canada, 2012), it accounts for 55-58% of the embodied energy (embodied energy material and processing data taken from Ashby (2009)). However, due to their small mass and the fact that aseptic cartons cannot be reused in new aseptic packaging, the recovery of laminates from aseptic cartons accounts for only a small decrease in the original package's global warming potential (Mourad et al., 2008).

Research by Tetra Pak and its partners in Brazil (Von Zuben et al. 2007; Pedroso and Bastos, 2006) reveals that there are often only marginal economic gains from the paper recovery of cartons alone, but that greater success and profitability can be achieved when valuable end-uses are found for the laminate material that is left over after pulping. Dunais (2009) also emphasizes the importance of finding value added end-uses to generate profit from carton recycling.

Despite the substantial investment that is put in the original manufacture of the laminate film for aseptic cartons and the meagre profit margin from pulp sales, only few companies seek to recover it at all. In Brazil, EET purchases the waste laminates from carton pulping at the neighbouring mill owned by Klabin and either agglomerates the material to sell as feedstock for injection and compression moulding consumer products, or separates the Al from the low-density polyethylene (LDPE) in a high-temperature, controlled atmosphere process (Pedroso and Bastos, 2006) and sells Al flakes and paraffin oil to industrial users. The Canadian company Groupe RCM has begun making commercial and industrial products from homogenized carton PE/Al blends (Tetra Pak, 2011). Elsewhere in the world, used aseptic cartons are burned for their heating value, incinerated just to reduce the mass sent to landfills (Elopak, 2008), dumped in landfills (Grant et al., 2001), or the Al and LDPE are separated through pyrolysis or a mechanical process (Elopak, 2008). Researchers have identified potential wet chemistry pathways for the material separation of laminate films (Ji-Fei et al., 2009), and uses in either blended plastics (Avella et al., 2009; Lopes et al., 2007) or compost operation substrates (Rodriguez et al., 1995).

Other laminated packaging waste resources that might be suitable, but lack current collection infrastructure (e.g. currently in mixed solid waste) or sufficient quantities are: Li-ion polymer battery packs for automotive (e.g. Chevy Volt) and shelf stable, sealed food bags (e.g. dry pet food bags and bulk wines/juices). Selection of a candidate waste material for supercooled salt hydrate PCM encapsulation must consider packaging sizes sufficient to produce moderate to large surface area (nominally $\geq$ 10x10 cm^2), and materials that are thin, and durable under tension and flexural strain.

Li-ion battery packs in next generation electric vehicles could potentially supply high-quality, durable, laminated sheets for PCM encapsulation. However, existing recovery methods for cell-phone batteries (having the same composition and basic construction as the automotive batteries) destroy the laminate encapsulation by shredding cryogenically frozen batteries and burning the remainder to optimize recovery of the valuable and sometimes toxic cathode minerals (Castillo et al., 2002; Espinosa et al., 2004; Ra and Han, 2006; Xu et al., 2008). Despite the destruction of the laminate encapsulations, Li-ion battery collection is largely conducted through electronic stewardship programs of consumer electronics (and soon automobiles), so waste concentration and recovery are potentially attractive, but suffer collection delays due to hoarding of defunct electronics (Bernardes et al., 2004).

Ultimately, the quality of the reclaimed materials, their post-consumer accessibility in the marketplace, and the profitability of the waste resource must be sufficient to be considered as an encapsulation for supercooled salt hydrate PCMs. Aseptic cartons are the present choice due to their availability in the post-consumer market; as such, their films are evaluated in the experiments to validate the two-region fin model.

1.3 RESEARCH STATEMENT

The research areas of PCM encapsulation science and layered composite heat transfer are not yet at a state for which an improved supercooled salt hydrate PCM LTHS encapsulation using laminate pouches could be proposed with claims of increased heat transfer rate during heat discharge without significant computational effort. It is therefore the intent of the current research to derive and validate (experimentally and numerically) a 2D, steady state, layered composite heat conduction model for rectangular (Cartesian

coordinates) and circular (cylindrical coordinates) heat source geometries to be used in predicting the rate of heat transfer due to heat spreading in LTHS PCM applications.

The proposed theoretical layered composite heat conduction model presented in Chapter 2 provides explicit solutions to the differential heat balance equations in order to allow straightforward implementation into spreadsheets and modelling software, requiring only little computational effort (i.e. non-iterative). Key model assumptions achieve the goal of reducing the solution complexity by only solving 1D differential heat balance equations in two adjacent domains, henceforth called the "two-region fin model". Provisions are also given to identify two-region fin model suitability for any given system as well as allowing for pseudo steady-state analysis in some circumstances. The two-region fin model includes a constant temperature boundary condition heat source (PCM) as well as constant heat flux (electric heating) with the intent of allowing the two-region fin model to be applied to cookware and electronics cooling applications. Finite element simulations provide the bases for numerical validation of the two-region fin model and are presented herein.

Experimental validation is presented in Chapter 3, whereby IR thermography was used to obtain high-resolution temperature measurements from a laminate film mounted on polystyrene foam, heated from behind using either a rectangular or circular electric heater, and externally cooled by either natural or forced convection. The two-region model was fit to experimental temperature measurements using two-parameter optimization in Matlab and assessed for prediction accuracy. Furthermore, measurement uncertainties were quantified and the two-region fin model error propagation was evaluated to aid in assessing the extent of the experimental validation.

Chapter 4 discusses the merits of material reclamation for laminate pouch encapsulation for supercooled salt hydrate LTHS PCMs. Promising post-consumer material resources are identified and assessed for material quality and ease of exploitation (material availability and supply chains), and some evidence of the profitability of resource recovery enterprises is provided.

Finally, Chapter 5 presents the conclusions to the research presented, and a discussion of future work is also included.

CHAPTER 2: LAMINATE HEAT CONDUCTION

2.1 INTRODUCTION

The principal work of this thesis is presented in these next sections. A detailed description of the postulation and complete derivation of the two-region fin model is given and its defining features explained. Non-dimensional derivations are also presented since they would more easily reveal the inherent qualities of the model than would a dimensional approach. A validation against finite element solutions in 2D (Cartesian) and axi-symmetric space (cylindrical) is also presented and confirmed.

2.2 TWO-REGION FIN MODEL

The system under study is presented in Fig.2.1, in which a layered body has at least three layers: upper (subscript 2) and lower (subscript 3) thermally resistive layers and a high thermal conductivity core (subscript 1) that is responsible for the heat spreading component to the conduction heat transport in the system. The system variables presented in Fig.2.1 are: layer specific thermal conductivity, k; layer specific thickness, t; heated region length and heated boundary x or r axis position, L; convection heat transfer coefficient, h; convection boundary free-stream temperature, T_{inf}; constant temperature heat source, T_i; and, constant heat flux source, q_o''. Subscripts 2 and 3, in Fig.2.1, are ordered as such for convenience when the bottom layer is not being considered in the calculations (see constant heat flux equations for the two-region fin model, section 2.2.4). Although the PCM heat source under consideration, T_i, represents only constant temperature phase changes (congruent systems) and most supercooled salt hydrates are incongruent systems, a constant temperature boundary condition is still deemed appropriate to represent supercooled salt hydrate PCMs. Incongruency in the phase equilibrium of salt hydrates does not typically produce very large temperature differences within the solidifying PCM and T_i can represent the average phase change temperature.

The system in Fig.2.1 can be represented equally in Cartesian or cylindrical coordinates, for which the z-axis always represents the layer heights (thicknesses t_1, t_2, and t_3 are along this axis) while the layers' lengths run along the x or r axis in Cartesian or cylindrical coordinates, respectively.

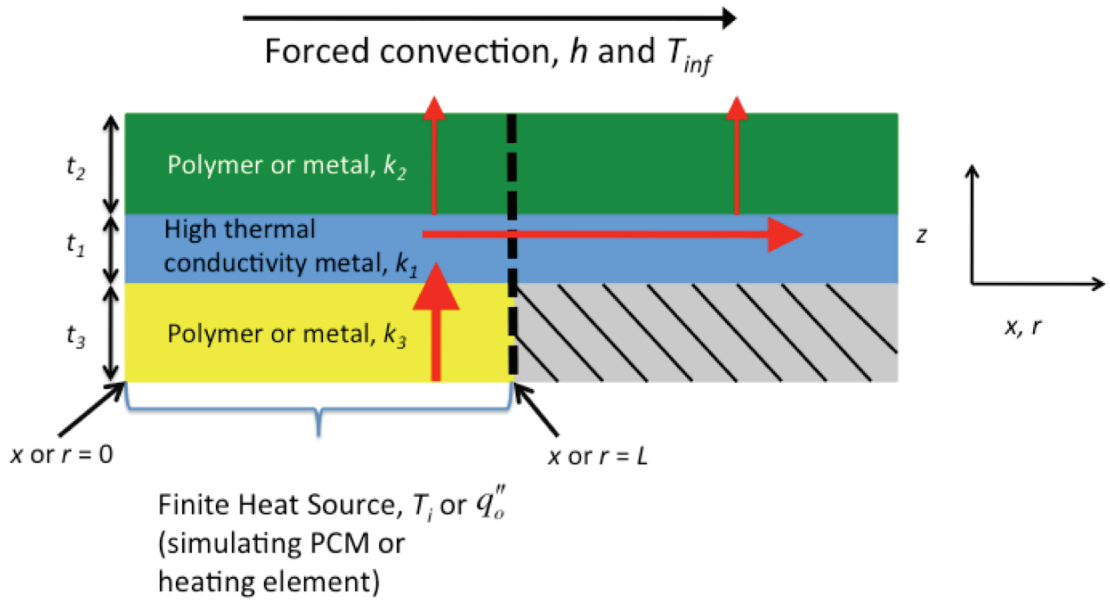

Figure 2.1: Schematic heat transfer model representation of a thin polymer/Al laminate where *k* represents the layers' thermal conductivity, *h* and T_{inf} are the respective convection heat transfer coefficient and free-stream temperature, and T_i and q''_o are the respective constant temperature and constant heat flux heat sources. The heated region is left of the dashed line (*x* or *r* = *L*), while the fin region is to the right.

The red arrows in Fig.2.1 show the directions of conduction heat transfer that are fundamental to the formulation of the two-region fin model. Conduction begins with the heat source covering only part of the bottom thermally resistive layer and passing through it in the *z*-direction (bottom red arrow). Still in the heated region, some heat is conveyed in the *z*-direction (called planar direction, see smaller vertical red arrow in the heated region) through the outer thermally resistive layer (heat exchange with the outside environment). There can also be heat conveyed outward to the unheated region through the high thermal conductivity metal core (red arrow crossing the heated region boundary, x or $r = L$). This thermal energy is dissipated to the environment through the outer thermally resistive layer. Depending on the design of the laminate material, there can be considerably more overall heat exchange due to the portion of heat transported in the unheated region (or fin region, x or $r \geq L$ in Fig.2.1).

With respect to the inner metal layer, the behaviour can be represented as a two-region fin heat transfer problem. To reduce the number of variables that must be solved in the differential heat balance equation, the following simplifying assumptions were applied:

1. The heat transfer problem is symmetric at the domain origin, x or $r = 0$;
2. Assume a planar 2D laminate in Cartesian coordinates and axial-symmetry (rotational symmetry around z) in cylindrical coordinates;
3. Assume that temperature gradient in the z-direction of the bottom layer of the fin region is negligible when compared to T_i - T_{inf}. Therefore, it is treated as being well insulated;
4. Assume only an axial temperature gradient (x or r directions) in the high thermal conductivity metal core;
5. Assume negligible axial heat conduction in the thermally resistive layers;
6. Constant thermal conductivities (non-isotropic), external heat transfer coefficients, and negligible thermal expansion of the materials are assumed.

2.2.1 ANALYTICAL LAMINATE TWO-REGION FIN MODEL

The two-region fin problem reduces a 2D system into a set of 1D symmetric, steady-state heat transfer equations solved only in the inner, high thermal conductivity metal core, but in two parts: the heated region and the fin region. Solutions were obtained in both the Cartesian and cylindrical coordinate systems. While the range of application of the two-region fin model is quite broad, consideration must be given to the implications of the core assumptions in order to justify this claim.

Heat spreading behaviour can be represented as the dominance of axial heat conduction (x or r directions) over planar heat conduction (z-direction) in the high thermal conductivity metal core (assumption #4), conversely that the planar thermal resistance dominates over the axial thermal resistance. In an order of magnitude approach, these are:

$$R_{axial} = L/k_1 \tag{2.1}$$

and

$$R_{planar} = \frac{t_1}{k_1} + \frac{t_2}{k_2} + \frac{1}{h} \tag{2.2}$$

in Cartesian coordinates only. The desired relationship for heat spreading is for

$$R_{axial} \ll R_{planar} \tag{2.3}$$

Consider, for example, a 0.1 mm laminate film with thermally resistive thermoplastic layers ($t_2 = t_3 \approx 0.04$ mm; $k_2 = k_3 \approx 0.4$ W m^{-1} K^{-1}) and Al foil high thermal conductivity

metal core ($t_1 \approx 0.02$ mm and $k_1 \approx 260$ W m^{-1} K^{-1}), externally cooled with air ($h \approx 50$ W m^{-2} K^{-1}) and a heated length (L) equal to 10 mm. To ensure heat spreading, these parameters must satisfy Eq.(2.3). From Eq.(2.1),

$$R_{axial} = \frac{0.01}{260}\frac{\mathrm{m^2K}}{\mathrm{W}} = 4\times10^{-5}\frac{\mathrm{m^2K}}{\mathrm{W}}, \tag{2.4}$$

and from Eq.(2.2),

$$R_{planar} = \left(\frac{0.00002}{260} + \frac{0.00004}{0.4} + \frac{1}{50}\right)\frac{\mathrm{m^2K}}{\mathrm{W}} = 0.02\frac{\mathrm{m^2K}}{\mathrm{W}}, \tag{2.5}$$

so it is clear that Eq.(2.3) is satisfied.

It would benefit to mention that the two-region fin model could also be used in pseudo steady-state analysis of laminate systems provided that the time derivative of the heated length, $\dot{L}$, is sufficiently small when considering the laminate's capacity for heat accumulation ($\dot{E}$). In an order of magnitude approach for a constant heat flux, this is:

$$\dot{E} = \dot{L}\frac{\rho_{ave}C_{p,ave}(t_2+t_3)q_o''}{k_2} \ll q_o'', \tag{2.6}$$

or

$$\dot{E} = \dot{L}\frac{\rho_{ave}C_{p,ave}(t_2+t_3)}{k_2} \ll 1, \tag{2.7}$$

where $C_{p,ave}$ and ρ_{ave} are the laminate body's mass average heat capacity and volume average density. Since laminate bodies are typically thin, pseudo steady-state analysis can often be considered. For example, taking the same laminate described above and $\rho_{ave} = 900$ kg m^{-3} and $C_{p,ave} = 2$ kJ kg^{-1}, a pseudo steady-state analysis would remain valid if

$$\dot{L}\frac{900(2000)(0.0008)}{0.4}\frac{\mathrm{s}}{\mathrm{m}} \ll 1 \tag{2.8}$$

or

$$\dot{L} \ll 0.3\times10^{-3}\frac{\mathrm{m}}{\mathrm{s}} \tag{2.9}$$

For an externally nucleated, supercooled, salt hydrate, this expansion rate could be reasonable for those with the highest latent heat of fusion, since crystal growth becomes heat transfer limited after the initial seeding (Lane, 1985; Sandnes, 2003).

The assumption that the bottom thermally resistive layer can be treated as well insulated in the fin region (assumption #3), although already justified, has its implications when considering the nature of supercooled salt hydrate solidification. Consider the case

of a supercooled salt hydrate nucleation site located directly underneath a simple, thermoplastic encapsulation, with no appreciable heat spreading (Fig.2.2), and the case with a nucleation site located directly underneath a laminate film encapsulation with heat spreading (Fig.2.3). The red arrows represent the magnitude and direction of heat transfer, and the white dashed lines represents the anticipated position of the solidification front after only a short time interval. For the purposes of the two cases presented in Figs.2.2 and 2.3, the supercooling temperature of the PCM, T_{sup}, is also equal to the free stream temperature of the heat transfer fluid, T_{inf}.

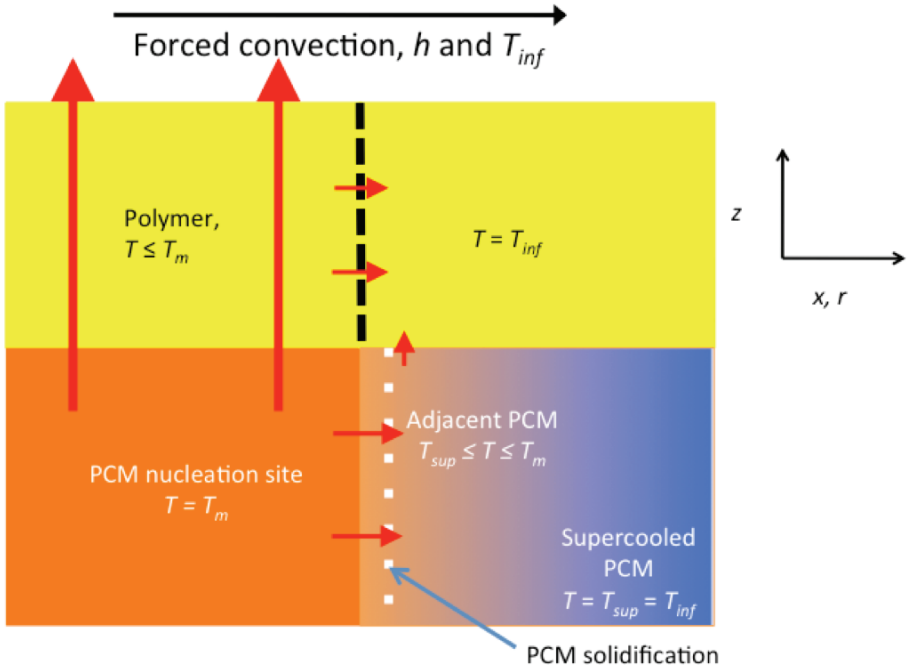

Figure 2.2: PCM solidification with a simple thermoplastic encapsulation and no appreciable heat spreading. The solid PCM is at its equilibrium melting/freezing temperature, T_m, and the remainder of the supercooled PCM is either mildly warm, or at the initial supercooled temperature, $T_{sup} = T_{inf}$. The dashed white line in the PCM shows the progression of the solidification front.

Axial heat conduction would be limited in both the simple thermoplastic encapsulation (Fig.2.2 only) and the liquid, supercooled, salt hydrate PCM (Fig.2.2 and 2.3) when forced convection on the outside of the encapsulation is the path of least resistance. As such, the simple thermoplastic encapsulation with no heat spreading (Fig.2.2) would promote linear growth of the PCM solidification front, since the solid PCM is itself the only heat source for the adjacent supercooled PCM. In this case, both

the supercooled PCM and the encapsulation's fin region – figuratively speaking – are mostly at the same temperature, T_{inf}, therefore would act as though insulated.

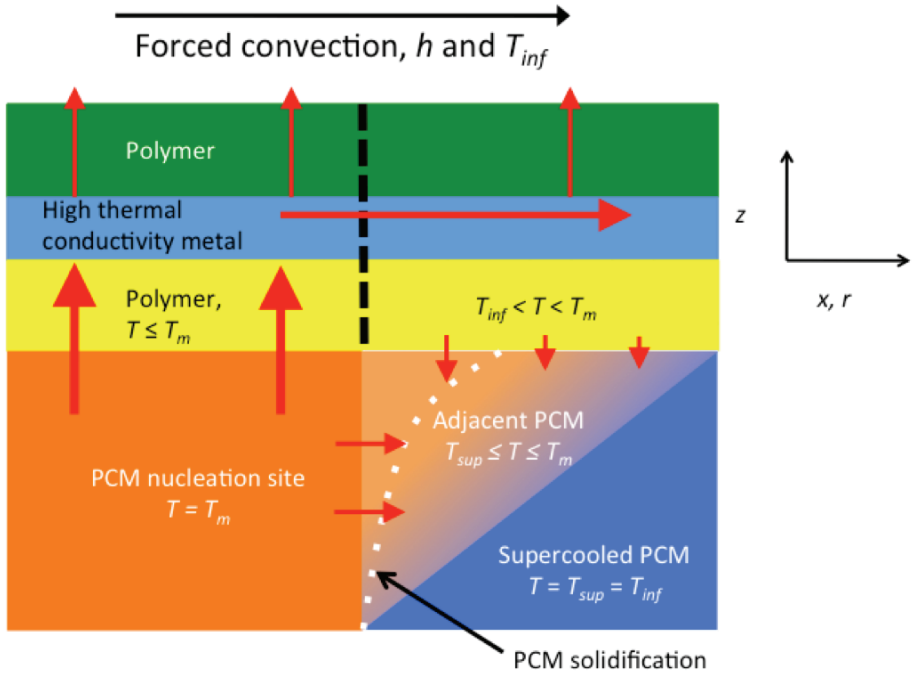

Figure 2.3: PCM solidification with a laminate film encapsulation and heat spreading. The solid PCM is at its equilibrium melting/freezing temperature, T_m, and the remainder of the supercooled PCM is either mildly warm, or at the initial supercooled temperature, T_{sup}. The dashed white line in the PCM shows the progression of the solidification front.

Even with the added effect of heat spreading by the laminate film encapsulation in Fig.2.3, the liquid PCM underneath the encapsulation's fin region should be at a similar temperature to the fin region temperature, $T_{inf} < T < T_m$. This condition minimizes the amount of PCM self-heating provided by the fin region heat conduction and allows the bottom layer of the fin region to act as though mostly well insulated. Figure 2.4 shows these temperature profiles and those of the other materials in the system described in Fig.2.3. However, the temperature profile representing the PCM in Fig.2.3 only shows the bulk average temperature, not the temperature profile of the portion of PCM just below the encapsulation's fin region that was just described.

As it was mentioned above, only a minimal amount of heat loss is expected to occur from the fin region to the cooler, liquid, supercooled PCM underneath it. This amount of heat exchange would alter the path of the solidification front (shown in Fig.2.3), but solidification would still mimic the original progression of the solidification front (Fig.2.2) as experienced on the bottom of the laminate film encapsulation (either in a

straight line, i.e. Cartesian model, or circles, i.e. cylindrical model). Only the projection of the solidification front on the bottom laminate layer has any influence on the two-region fin model heat transfer.

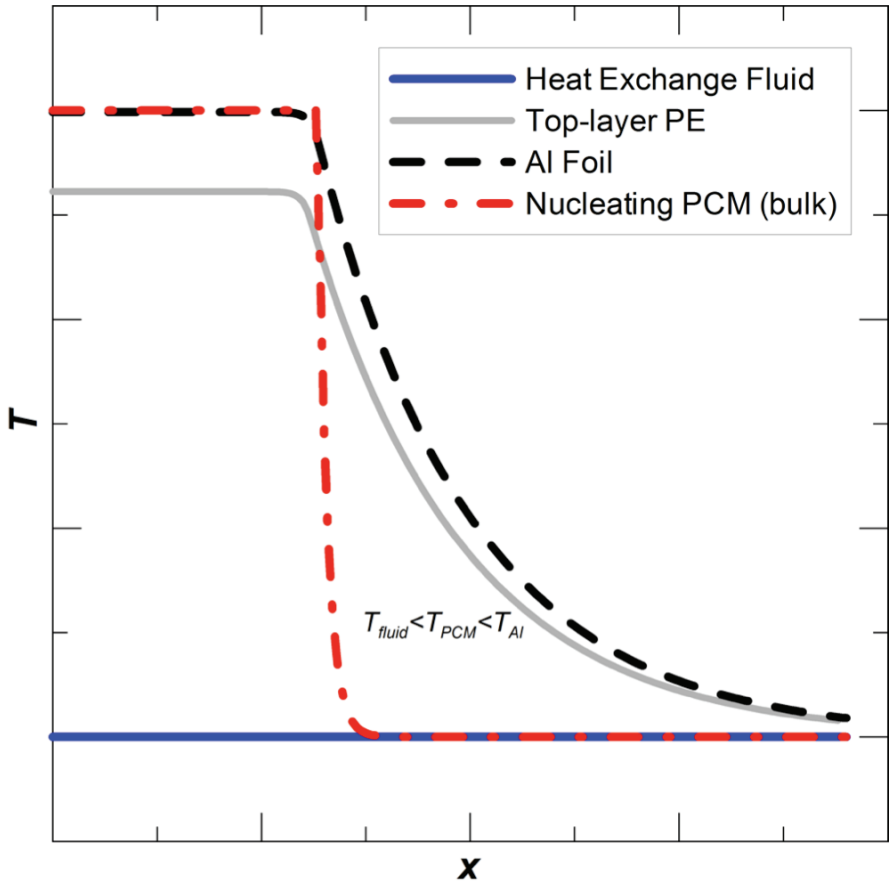

Figure 2.4: Temperature profiles representing nominal conditions for the laminate model shown in Fig. 2.3. Note that the PCM temperature profile represents the axial positions from left to right of the mean, bulk temperature of the PCM.

2.2.2 CARTESIAN COORDINATES (APPLIED TEMPERATURE)

Heated Region:

The Cartesian thermal energy balance equation applied only to the high thermal conductivity metal core in the heated region ($0 \le x \le L$) with a constant applied temperature (T_i) is given by

$$\frac{d^2T}{dx^2} - \frac{k_3}{t_3 t_1 k_1}\left(T - T_i\right) - \frac{1}{R t_1 k_1}\left(T - T_{\inf}\right) = 0\,, \qquad (2.10)$$

where $R = t_2/k_2 + 1/h$. Equation (2.10) is a second-order, linear, non-homogeneous ODE with respect to T and can be rearranged to the general form:

$$\frac{d^2T}{dx^2} - \left(\frac{1}{R} + \frac{k_3}{t_3}\right)\frac{T}{t_1 k_1} = -\frac{1}{t_1 k_1}\left(\frac{T_{\inf}}{R} + \frac{k_3}{t_3}T_i\right). \tag{2.11}$$

Equation (2.11) has to be solved using the following two boundary conditions:

1. $T(x = L) = T_o$ (continuity)

2. $\left.\frac{dT}{dx}\right|_{x=0} = 0$ (symmetry).

The solution has the form $T(x) = T_c + T_p$, where T_c and T_p designate the complementary and particular solutions to $T(x)$ in the heated region, respectively. T_c corresponds to the solution of the homogeneous ODE, as follows,

$$\frac{d^2T_c}{dx^2} - \left(\frac{1}{R} + \frac{k_3}{t_3}\right)\frac{T_c}{t_1 k_1} = 0, \tag{2.12}$$

whose solution is:

$$T_c(x) = C_1 \mathrm{e}^{\alpha x} + C_2 \mathrm{e}^{-\alpha x}, \tag{2.13}$$

and

$$\alpha^2 = \frac{1}{t_1 k_1}\left(\frac{1}{R} + \frac{k_3}{t_3}\right). \tag{2.14}$$

The particular solution is solved using the method of unknown coefficients, for which $T_p(x) = C_3 + C_4 x + C_5 x^2$. Substituting T_p into Eq.(2.11), the coefficients C_3, C_4, C_5 are found to be $C_4 = C_5 = 0$ and

$$C_3 = \frac{t_3 T_{\inf} + R k_3 T_i}{t_3 + R k_3}, \tag{2.15}$$

hence the particular solution is:

$$T_p = \frac{t_3 T_{\inf} + R k_3 T_i}{t_3 + R k_3} = \beta. \tag{2.16}$$

Applying the two boundary conditions, the temperature profile in the heated region is:

$$T(x) = (T_o - \beta)\frac{\cosh(\alpha x)}{\cosh(\alpha L)} + \beta. \tag{2.17}$$

Fin Region:

In the fin region, $x \geq L$, the thermal energy balance applied to the high thermal conductivity metal core, regardless of the heat source (T_i or q_o''), is shown here in the general form of a second-order linear, non-homogeneous ODE with respect to T,

$$\frac{d^2T}{dx^2} - \frac{1}{Rt_1k_1}T = -\frac{1}{Rt_1k_1}T_{\inf} . \tag{2.18}$$

The fin region would obey the following boundary conditions:

1. $T(x = L) = T_o$ (continuity)
2. $\lim_{x\to\infty} T(x) = T_{\inf}$ (equilibrium).

Just as for Eq.(2.11), $T(x) = T_c + T_p$ in the fin region. The method of achieving the complementary solution is the same as it was for Eq.(2.12), so

$$T_c(x) = C_1 \mathrm{e}^{\gamma x} + C_2 \mathrm{e}^{-\gamma x} , \tag{2.19}$$

where

$$\gamma^2 = \frac{1}{Rt_1k_1} . \tag{2.20}$$

The same method and polynomial solution that was used to obtain Eq.(2.16) is also used to solve T_p in the fin region, for which the coefficients for the fin region are $C_3 = T_{inf}$ and $C_4 = C_5 = 0$. Therefore, $T_p = T_{inf}$.

The fin region temperature profile then becomes:

$$T(x) = \left(T_o - T_{\inf}\right)\mathrm{e}^{-\gamma(x-L)} + T_{\inf} . \tag{2.21}$$

The problem has not been fully specified yet since the temperature profiles in both regions have the unknown boundary condition, T_o, that they share at $x = L$. This boundary condition implies heat continuity, so

$$\left.\frac{dT}{dx}\right|_{x=L} = \alpha\left(T_o - \beta\right)\tanh\left(\alpha L\right) \tag{2.22}$$

in the heated region, and

$$\left.\frac{dT}{dx}\right|_{x=L} = \gamma\left(T_{\inf} - T_o\right) \tag{2.23}$$

in the fin region. Equating Eq.(2.22) and Eq.(2.23),

$$\left(T_o-\beta\right)\tanh\left(\alpha L\right)=\left.\frac{dT}{dx}\right|_{x=L}=\gamma\left(T_{\inf}-T_o\right), \tag{2.24}$$

the explicit expression is obtained for the shared boundary condition, T_o, so

$$T_o=\frac{\gamma T_{\inf}+\alpha\beta\tanh\left(\alpha L\right)}{\gamma+\alpha\tanh\left(\alpha L\right)}. \tag{2.25}$$

Cartesian Heat Transfer:

What remains in this exploration of the two-region fin problem are the two aspects of heat transfer: overall linear power density entering and leaving the system, Q'_{lam}, and the fin-only linear power density that crosses the heated region boundary at $x = L$, Q'_{fin}. Their physical representations are both illustrated in Fig.2.5. Note that the Cartesian solution heat transfer calculations must all remain as linear power densities, W m^{-1}, due to the 2D laminate assumption in Cartesian coordinates.

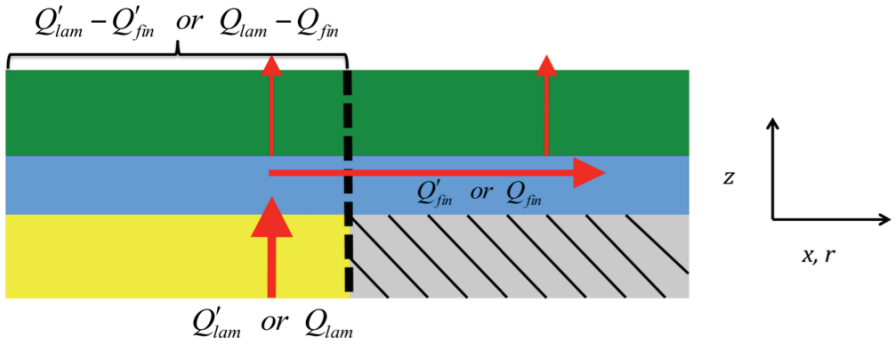

Figure 2.5: Laminate body diagram showing directions of conduction heat transfer for the same representative laminate body in Fig.2.1. The linear power densities (prime notation) refer to the Cartesian model and the overall rates of heat transfer (without prime) relate to the cylindrical model.

Simply stated, these are:

$$Q'_{lam}=\int_0^L\frac{k_3}{t_3}\left(T_i-T\right)dx=\frac{k_3}{t_3}\left[L\left(T_i-\beta\right)-\frac{\left(T_o-\beta\right)}{\alpha}\tanh\left(\alpha L\right)\right] \tag{2.26}$$

and

$$Q'_{fin}=-k_1t_1\left.\frac{dT}{dx}\right|_{x=L}=\left(T_o-T_{\inf}\right)\sqrt{\frac{k_1t_1}{R}}. \tag{2.27}$$

One final notion to discuss, applying only constant temperature heat sources (e.g., PCMs), is the overall laminate heat transfer effectiveness, η, presented below.

$$\eta = \frac{Q'_{lam}}{Q'_{simple}} \tag{2.28}$$

Equation (2.28) is the ratio of the laminate rate of heat transfer over simple encapsulation made of the same durable, but low thermal conductivity outer layers of the laminate and of the same overall thickness as the laminate. The simple encapsulation is assumed to only allow planar heat transfer.

The expression for the simple, non-laminate encapsulation as defined by assumption #5 in section 2.2 is given by

$$Q'_{simple} = \int_0^L \frac{1}{\frac{t_2}{k_2} + \frac{t_3}{k_3} + \frac{1}{h}} \left(T_i - T_{\inf}\right) dx = \frac{L\left(T_i - T_{\inf}\right)}{\frac{t_2}{k_2} + \frac{t_3}{k_3} + \frac{1}{h}}. \tag{2.29}$$

Since the conditions ensuring the accuracy of assumption #5 are not essential for heat spreading, substituting Eq.(2.29) for Q'_{simple} might underestimate the non-laminate rate of heat transfer when 2D conduction is indeed significant and can therefore be substituted with a more accurate solution when one is available.

Substituting Eq.(2.26) and (2.29) into Eq.(2.28) provides a clearer expression of η:

$$\eta = \frac{\left(\frac{t_2}{k_2} + \frac{t_3}{k_3} + \frac{1}{h}\right)\frac{k_3}{t_3}\left[L\left(T_i - \beta\right) - \frac{\left(T_o - \beta\right)}{\alpha}\tanh\left(\alpha L\right)\right]}{L\left(T_i - T_{\inf}\right)} \geq 1. \tag{2.30}$$

Positive contributions > 1 from the terms $(t_2/h_2 + t_3/h_3 + 1/h)\, k_3/t_3$ and $-(T_o-\beta)\tanh(\alpha L)/\alpha$ ($T_o \rightarrow T_{inf}$ at small values of α), in Eq.(2.30), show that laminate heat transfer is usually superior to the homogeneous kind. The maximization of this metric, η, while also satisfying minimum strength requirements and encapsulation weight, is of foremost significance to designing encapsulation for supercooled PCM, long-term heat storage.

2.2.3 CYLINDRICAL COORDINATES (APPLIED TEMPERATURE)

Heated Region:

The mathematical derivation has pertained only to Cartesian coordinates so far. The following will address the problem of an axi-symmetric, 2D laminate body, with a constant temperature heat source, T_i, in the domain $0 \leq r \leq L$. The thermal energy balance equation applied only to the high thermal conductivity metal core in this domain is

$$\pi r t_1 k_1 \left[\frac{1}{r}\frac{d}{dr}\left(r\frac{dT}{dr}\right)\right] - \frac{\pi r}{R}\left(T - T_{\inf}\right) + \frac{\pi r k_3}{t_3}\left(T_i - T\right) = 0\,, \tag{2.31}$$

where $R = t_2/k_2 + 1/h$. Equation (2.31) is a non-homogeous modified Bessel equation of order zero with respect to T, which can be rearranged in the general form:

$$r^2\frac{d^2T}{dr^2} + r\frac{dT}{dr} - \alpha^2 r^2 T = -\frac{r^2}{t_1 k_1}\left(\frac{T_{\inf}}{R} + \frac{T_i k_3}{t_3}\right), \tag{2.32}$$

where

$$\alpha^2 = \frac{1}{t_1 k_1}\left(\frac{1}{R} + \frac{k_3}{t_3}\right). \tag{2.33}$$

Again, the heated region would have the following two boundary conditions:

1. $T(r = L) = T_o$ (continuity)
2. $\left.\frac{dT}{dr}\right|_{r=0} = 0$ (symmetry).

The solution to Eq.(2.32) takes the form $T(r) = T_c + T_p$, where T_c and T_p designate the complementary and particular solutions to the temperature profile in the heated region, respectively. For the complementary solution, which is the solution to the homogeneous modified Bessel equation,

$$r^2\frac{d^2T_c}{dr^2} + r\frac{dT_c}{dr} - \alpha^2 r^2 T_c = 0\,, \tag{2.34}$$

T_c is:

$$T_c(r) = C_1\,\mathrm{I}_0\left(\alpha r\right) + C_2\,\mathrm{K}_0\left(\alpha r\right). \tag{2.35}$$

The particular solution to Eq.(2.32), T_p, is also obtained using the method of unknown coefficients and a 2nd order polynomial. The coefficients are $C_4 = C_5 = 0$ and,

$$C_3 = \frac{t_3 T_{\inf} + R k_3 T_i}{t_3 + R k_3}\,, \tag{2.36}$$

and result in the following solution:

$$T_p = \frac{t_3 T_{\inf} + R k_3 T_i}{t_3 + R k_3} = \beta\,. \tag{2.37}$$

This gives the complete temperature profile in the heated region:

$$T(r) = \left(T_o - \beta\right)\frac{\mathrm{I}_0\left(\alpha r\right)}{\mathrm{I}_0\left(\alpha L\right)} + \beta\,. \tag{2.38}$$

Fin Region:

In the fin region, $r \geq L$, the thermal energy balance applied to the high thermal conductivity metal core, regardless of the heat source (T_i or q_o''), is shown here in the form of a non-homogeneous modified Bessel equation of order zero with respect to T,

$$r^2\frac{d^2T}{dr^2} + r\frac{dT}{dr} - \gamma^2 r^2 T = -\gamma^2 r^2 T_{\inf}\,, \tag{2.39}$$

where

$$\gamma^2 = \frac{1}{Rt_1 k_1}\quad. \tag{2.40}$$

The fin region would still obey the same two boundary conditions:

1. $T(r = L) = T_o$ (continuity)
2. $\lim_{r\to\infty} T(r) = T_{\inf}$ (equilibrium).

Just as for Eq.(2.32), $T(r) = T_c + T_p$ in the fin region. The method of solution for the complementary solution would still be the same as for Eq.(2.34):

$$T_c(r) = C_1\,\mathrm{I}_0\left(\gamma r\right) + C_2\,\mathrm{K}_0\left(\gamma r\right). \tag{2.41}$$

The method of unknown coefficients is again used to obtain T_p, for which $C_4 = C_5 = 0$ and $C_3 = T_{inf}$.

The complete fin region temperature would be:

$$T(r) = \left(T_o - T_{\inf}\right)\frac{\mathrm{K}_0\left(\gamma r\right)}{\mathrm{K}_0\left(\gamma L\right)} + T_{\inf}\,. \tag{2.42}$$

The determination of the unknown boundary condition shared by both domains at $r = L$, T_o, follows the same method as was used in Cartesian coordinates (Eq.(2.22) to Eq.(2.25)). The heat continuity solution expression in the heated region is

$$\left.\frac{dT}{dr}\right|_{r=L} = \left(T_o - \beta\right)\alpha\frac{\mathrm{I}_1\left(\alpha L\right)}{\mathrm{I}_0\left(\alpha L\right)} \tag{2.43}$$

and also in the fin region

$$\left.\frac{dT}{dr}\right|_{r=L} = \left(T_{\inf} - T_o\right)\gamma\frac{\mathrm{K}_1\left(\gamma L\right)}{\mathrm{K}_0\left(\gamma L\right)}\,. \tag{2.44}$$

Since Eqs.(2.43) and (2.44) are equal to one another, then

$$\left(T_o-\beta\right)\alpha\frac{\mathrm{I}_1\left(\alpha L\right)}{\mathrm{I}_0\left(\alpha L\right)}=\left.\frac{dT}{dr}\right|_{r=L}=\left(T_{\inf}-T_o\right)\gamma\frac{\mathrm{K}_1\left(\gamma L\right)}{\mathrm{K}_0\left(\gamma L\right)} \tag{2.45}$$

to obtain the final result:

$$T_o=\frac{\alpha\beta\,\mathrm{I}_1\left(\alpha L\right)\mathrm{K}_0\left(\gamma L\right)+\gamma T_{\inf}\,\mathrm{K}_1\left(\gamma L\right)\mathrm{I}_0\left(\alpha L\right)}{\alpha\,\mathrm{I}_1\left(\alpha L\right)\mathrm{K}_0\left(\gamma L\right)+\gamma\,\mathrm{K}_1\left(\gamma L\right)\mathrm{I}_0\left(\alpha L\right)}. \tag{2.46}$$

Cylindrical Heat Transfer:

In order to evaluate the amount of heat transfer improvement for a constant temperature heat source (e.g., PCM), the rate of heat transfer (for the representative half domain only) for the cylindrical two-region fin problem, Q_{lam}, and the fin-only rate of heat transfer, Q_{fin}, (recall Fig.2.5) are:

$$Q_{lam}=\int_0^L\frac{k_3}{t_3}\left(T_i-T\right)\pi r dr=\frac{k_3\pi L}{t_3}\left[\frac{L}{2}\left(T_i-\beta\right)-\frac{\left(T_o-\beta\right)}{\alpha}\frac{\mathrm{I}_1\left(\alpha L\right)}{\mathrm{I}_0\left(\alpha L\right)}\right] \tag{2.47}$$

$$Q_{fin}=-k_1t_1\pi L\left.\frac{dT}{dr}\right|_{r=L}=k_1t_1\pi L\left(T_o-T_{\inf}\right)\gamma\frac{\mathrm{K}_1\left(\gamma L\right)}{\mathrm{K}_0\left(\gamma L\right)}. \tag{2.48}$$

The resulting rate of heat transfer from the simple encapsulation model, Q_{simple}, and heat transfer effectiveness, η, in cylindrical coordinates are:

$$Q_{simple}=\int_0^L\frac{1}{\frac{t_2}{k_2}+\frac{t_3}{k_3}+\frac{1}{h}}\left(T_i-T_{\inf}\right)\pi r dr=\frac{\pi L^2\left(T_i-T_{\inf}\right)}{2\left(\frac{t_2}{k_2}+\frac{t_3}{k_3}+\frac{1}{h}\right)} \tag{2.49}$$

and

$$\eta=\frac{2\left(\frac{t_2}{k_2}+\frac{t_3}{k_3}+\frac{1}{h}\right)\frac{k_3\pi L}{t_3}\left[\frac{L}{2}\left(T_i-\beta\right)-\frac{\left(T_o-\beta\right)}{\alpha}\frac{\mathrm{I}_1\left(\alpha L\right)}{\mathrm{I}_0\left(\alpha L\right)}\right]}{\pi L^2\left(T_i-T_{\inf}\right)}\geq 1. \tag{2.50}$$

2.2.4 EQUATIONS AND PARAMETERS

The effect of the applied heat flux boundary condition, q_o'', is only present in the heated region of both the Cartesian and cylindrical coordinate models (boundary conditions to solve ODEs remain the same). Shown in this order, their differential heat balances are:

$$\frac{d^2T}{dx^2} - \frac{T}{Rt_1k_1} = -\frac{1}{t_1k_1}\left(\frac{T_{\inf}}{R} + q_o''\right), \tag{2.51}$$

in Cartesian coordinates, and

$$r^2\frac{d^2T}{dr^2} + r\frac{dT}{dr} - \alpha^2r^2T = -\frac{r^2}{t_1k_1}\left(\frac{T_{\inf}}{R} + q_o''\right), \tag{2.52}$$

in cylindrical coordinates, for which $\alpha^2 = (Rt_1k_1)^{-1}$.

The resulting solutions are summarized along with the equivalent equations derived for the nucleated, supercooled, PCM heat source (T_i boundary condition) in Tables 2.1 and 2.2.

Table 2.1: Summary of the two-region fin model in Cartesian coordinates.

Parameter	T_i	q_o''
$T,\ 0 \le x,r \le L$	$T(x) = (T_o - \beta)\dfrac{\cosh(\alpha x)}{\cosh(\alpha L)} + \beta$	
$T,\ x,r \ge L$	$T(x) = (T_o - T_{\inf})\mathrm{e}^{-\gamma(x-L)} + T_{\inf}$	
α	$\alpha^2 = \dfrac{1}{t_1k_1}\left(\dfrac{1}{R} + \dfrac{k_3}{t_3}\right)$	$\alpha^2 = \dfrac{1}{Rt_1k_1}$
γ	$\gamma^2 = \dfrac{1}{Rt_1k_1}$	
β	$\beta = \dfrac{t_3T_{\inf} + Rk_3T_i}{t_3 + Rk_3}$	$\beta = T_{\inf} + Rq_o''$
T_o	$T_o = \dfrac{\gamma T_{\inf} + \alpha\beta\tanh(\alpha L)}{\gamma + \alpha\tanh(\alpha L)}$	
Q'_{lam}	$Q'_{lam} = \dfrac{k_3}{t_3}\left[L(T_i - \beta) - \dfrac{(T_o - \beta)}{\alpha}\tanh(\alpha L)\right]$	$Q'_{lam} = Lq_o''$
Q'_{fin}	$Q'_{fin} = (T_o - T_{\inf})\sqrt{\dfrac{k_1t_1}{R}}$	
Q'_{simple}	$Q'_{simple} = \dfrac{L(T_i - T_{\inf})}{\dfrac{t_2}{k_2} + \dfrac{t_3}{k_3} + \dfrac{1}{h}}$	$Q'_{simple} = Lq_o''$
η	$\eta = \dfrac{Q'_{lam}}{Q'_{simple}} \ge 1$	$\eta = 1$

Table 2.2: Summary of the two-region fin model in cylindrical coordinates.

Parameter	T_i	q_o''
$T,\ 0 \le x,r \le L$	$T(r) = (T_o - \beta)\dfrac{\mathrm{I}_0(\alpha r)}{\mathrm{I}_0(\alpha L)} + \beta$	
$T,\ x,r \ge L$	$T(r) = (T_o - T_{\inf})\dfrac{\mathrm{K}_0(\gamma r)}{\mathrm{K}_0(\gamma L)} + T_{\inf}$	
α	$\alpha^2 = \dfrac{1}{t_1 k_1}\left(\dfrac{1}{R} + \dfrac{k_3}{t_3}\right)$	$\alpha^2 = \dfrac{1}{R t_1 k_1}$
γ	$\gamma^2 = \dfrac{1}{R t_1 k_1}$	
β	$\beta = \dfrac{t_3 T_{\inf} + R k_3 T_i}{t_3 + R k_3}$	$\beta = T_{\inf} + R q_o''$
T_o	$T_o = \dfrac{\alpha\beta\,\mathrm{I}_1(\alpha L)\mathrm{K}_0(\gamma L) + \gamma T_{\inf}\,\mathrm{K}_1(\gamma L)\mathrm{I}_0(\alpha L)}{\alpha\,\mathrm{I}_1(\alpha L)\mathrm{K}_0(\gamma L) + \gamma\,\mathrm{K}_1(\gamma L)\mathrm{I}_0(\alpha L)}$	
Q_{lam}	$Q_{lam} = \dfrac{k_3 \pi L}{t_3}\left[\dfrac{L}{2}(T_i - \beta) - \dfrac{(T_o - \beta)}{\alpha}\dfrac{\mathrm{I}_1(\alpha L)}{\mathrm{I}_0(\alpha L)}\right]$	$Q_{lam} = \dfrac{1}{2}\pi L^2 q_o''$
Q_{fin}	$Q_{fin} = k_1 t_1 \pi L (T_o - T_{\inf})\gamma\dfrac{\mathrm{K}_1(\gamma L)}{\mathrm{K}_0(\gamma L)}$	
Q_{simple}	$Q_{simple} = \dfrac{\pi L^2 (T_i - T_{\inf})}{2\left(\dfrac{t_2}{k_2} + \dfrac{t_3}{k_3} + \dfrac{1}{h}\right)}$	$Q_{simple} = \dfrac{1}{2}\pi L^2 q_o''$
η	$\eta = \dfrac{Q_{lam}}{Q_{simple}} \ge 1$	$\eta = 1$

The element that sets apart the solutions in the two coordinate systems is the area for heat transfer in the fin region, which is far better enhanced in cylindrical coordinates compared to Cartesian coordinates. This supposition was further proven in the analyses of the limits of $Q_{fin}^{'}$ (Eq.(2.27)) and Q_{fin} (Eq.(2.48)) as the heated length, L, approaches infinity. In Cartesian coordinates, the limit becomes

$$Q'_{fin,sat} = \lim_{L\to\infty} Q'_{fin} = \left(\frac{\gamma T_{\inf} + \alpha\beta\tanh(\alpha\infty)}{\gamma + \alpha\tanh(\alpha\infty)} - T_{\inf}\right)\sqrt{\frac{k_1 t_1}{R}} \tag{2.53}$$

and reduces to the following explicit expression

$$Q'_{fin,sat} = \left(\frac{\gamma T_{\inf} + \alpha\beta}{\gamma + \alpha} - T_{\inf} \right) \sqrt{\frac{k_1 t_1}{R}} \,. \tag{2.54}$$

As for the limit in cylindrical coordinates,

$$Q_{fin,sat} = \lim_{L\to\infty} Q_{fin} = k_1 t_1 \pi\infty \left(\frac{\alpha\beta \, \mathrm{I}_1(\infty)\mathrm{K}_0(\infty) + \gamma T_{\inf} \, \mathrm{K}_1(\infty)\mathrm{I}_0(\infty)}{\alpha \, \mathrm{I}_1(\infty)\mathrm{K}_0(\infty) + \gamma \, \mathrm{K}_1(\infty)\mathrm{I}_0(\infty)} - T_{\inf} \right) \gamma \frac{\mathrm{K}_1(\infty)}{\mathrm{K}_0(\infty)} \,, \tag{2.55}$$

where it is known that $\mathrm{I}_0(\infty) = \mathrm{I}_1(\infty)$ and $\mathrm{K}_0(\infty) = \mathrm{K}_1(\infty)$, so the final expression can be given as

$$Q_{fin,sat} = k_1 t_1 \pi\infty \left(\frac{\alpha\beta + \gamma T_{\inf}}{\alpha + \gamma} - T_{\inf} \right) \gamma \to \infty \,. \tag{2.56}$$

In Equations (2.54) and (2.56), the subscript *sat* denotes the maximum theoretical values. The value of Q'_{fin} suffers diminishing returns with every incremental increase in L since the limit exists (hence *sat*, meaning saturation), while Q_{fin} shows no halt in its progression (due to the L multiplier in front). That is not to say that the value of Q_{fin} does not also suffer diminishing returns with increasing L (constant first derivative with respect to L as $L \to \infty$ in Eq.(2.56)), but the limit, $Q_{fin,sat}$, does not exist. In either of the coordinate systems, the value of η does approach 1 with increasing L, as can be seen by the curves representing η in the two coordinate systems for a fixed laminate geometry (0.1 mm thick: two 0.04 mm thick polyethylene layers, and one 0.02 mm thick Al foil layer) and a convection coefficient, h, equal to 25 W m^{-2} K^{-1} in Fig.2.6. The axis variables in Fig.2.6, excluding η, are normalized with respect to the values computed at L_0 = 1 mm, being the first value in the data sets. Most interestingly, the fact that the curve representing Q'_{fin} (shown as the normalized ratio $\frac{Q_{fin}(L)}{Q_{fin}(L_0)}$ on the right axis in Fig.2.6) in the upper panel shows a distinct plateau, which is the true manifestation of $Q'_{fin,\,sat}$, while the lower panel confirms the linear increase in Q_{fin} with increasing values of L (also normalized on the same axis) in cylindrical coordinates.

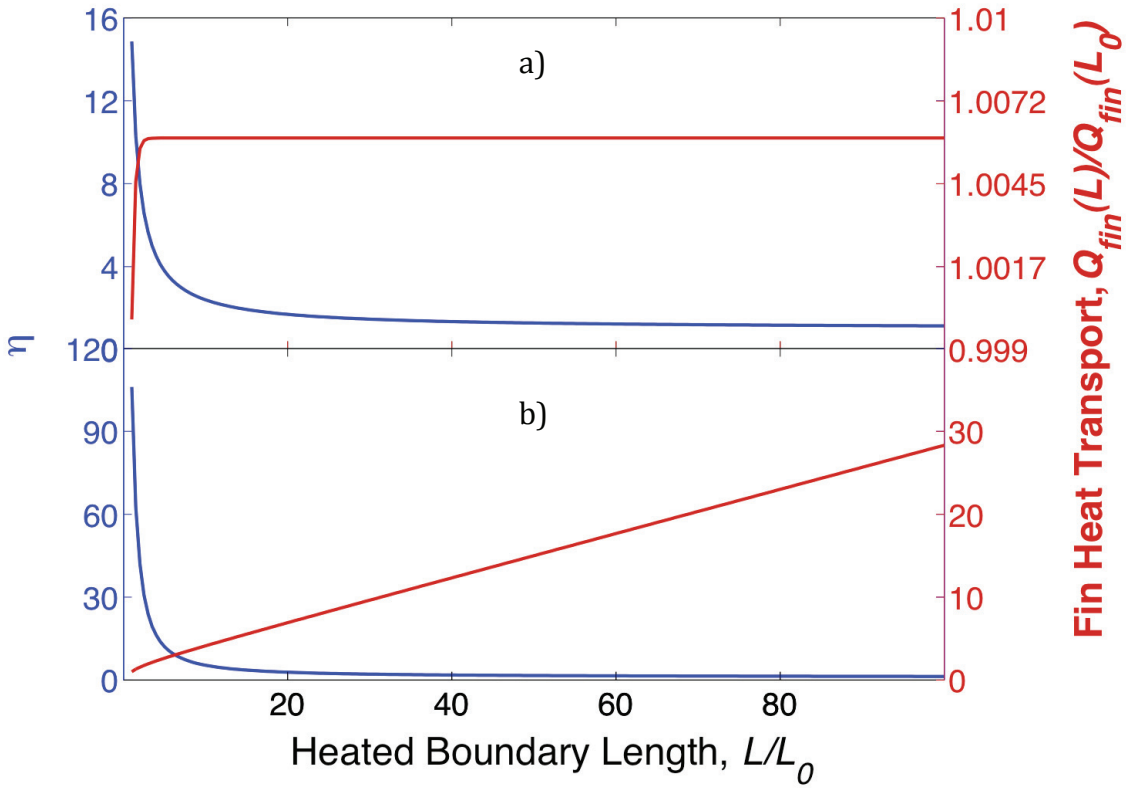

Figure 2.6: Laminate heat transfer effectiveness for applied temperature heat source only: a) Cartesian coordinates and b) cylindrical coordinates. L_o represents the smallest heated region in the solution set (1 mm); the fin heat transport is also relative to the solution at L_o.

Two additional scenarios involving the two-region fin model also use many of the same equations from Tables 2.1 and 2.2, but some of the parameters require adjustments. In the first case, the two regions are cooled by natural convection and their integral average convection coefficients must be assigned separately, simply h_h and h_f (also R_h and R_f) for the heated and fin regions respectively. The solutions presented in Tables 2.1 and 2.2 remain the same, however each region must have either h_h or h_f and R_h and R_f as substitutions for h and R. This method cannot include any greater accuracy of the locally changing convection coefficient within each of the domains, since doing so would add an additional non-linear term in the differential equations and would be coupled to the Navier-Stokes equations to solve for the exact solution of natural convection.

In the second case, consider a well-insulated top surface of the heated section only, so $h = 0$, but the fin region remains cooled by a fluid, so $h \neq 0$. For this case with the applied temperature boundary condition (T_i), the solution in the heated domain is only affected by the solution for β,

$$\beta = T_i, \tag{2.57}$$

while the remainder of the solutions outlined in Tables 2.1 and 2.2 is unchanged. With the applied heat flux boundary condition, however, the differential heat balance equation in the heated region must be solved anew. The solution in Cartesian coordinates to the second-order, separable, non-homogeneous, differential heat balance equation in the heated region ($0 \le x \le L$) for this case becomes:

$$T(x) = \frac{q_o''}{2t_1 k_1}\left(L^2 - x^2\right) + T_o \ . \tag{2.58}$$

The solution to the unknown boundary condition, T_o, must also be evaluated for the solution in Eq.(2.58), for which

$$\left.\frac{dT}{dx}\right|_{x=L} = -\frac{L}{t_1 k_1} q_o'' \tag{2.59}$$

in the heated region, and

$$\left.\frac{dT}{dx}\right|_{x=L} = \gamma\left(T_{\inf} - T_o\right) \tag{2.60}$$

in the fin region, giving

$$-\frac{L}{t_1 k_1} q_o'' = \gamma\left(T_{\inf} - T_o\right) \tag{2.61}$$

to obtain the final result:

$$T_o = T_{\inf} + \frac{L}{t_1 k_1 \gamma} q_o'' \ . \tag{2.62}$$

In the cylindrical coordinates, the solutions corresponding to Eqs. (2.58) and (2.62) are:

$$T(r) = \frac{q_o''}{4t_1 k_1}\left(L^2 - r^2\right) + T_o \tag{2.63}$$

and

$$T_o = T_{\inf} + \frac{\mathrm{K}_0(\gamma L)}{\mathrm{K}_1(\gamma L)} \frac{L}{2t_1 k_1 \gamma} q_o'' \ . \tag{2.64}$$

In both coordinate systems, with the applied heat source q_o'' and the well-insulated top of the heated region, the remaining equations are all identical to those in Tables 2.1 and 2.2.

2.2.5 DIMENSIONLESS EQUATIONS

Dimensionless variables were assigned for the two-region equations in Tables 2.1 and 2.2 in order to reveal the intrinsic qualities of the two-region fin model and to simplify the graphical representation of the solutions. The following treatment is for Cartesian coordinates only; the cylindrical analogues will follow.

In the heated region with the applied temperature boundary condition, the characteristic path length becomes,

$$\alpha x = \lambda\sqrt{\Omega_\alpha}\,, \tag{2.65}$$

where $\lambda = x/L$ (substitute r for x in cylindrical coordinates) and

$$\Omega_\alpha = \frac{L^2}{Rt_1k_1}\left(1+\frac{k_3R}{t_3}\right). \tag{2.66}$$

The new variables λ and Ω_α represent the characteristic length and relative thermal resistance of fin heat transport in the heated domain (indicated by subscript α), respectively.

The same approach is taken in the fin region, and the variable λ is present the same way as it is in Eq.(2.65), but the relative resistance of fin heat transport in the fin region (hence subscript γ), Ω_γ, takes the place of Ω_α. The substitution becomes:

$$\gamma x = \lambda\sqrt{\Omega_\gamma}\,, \tag{2.67}$$

where

$$\Omega_\gamma = \frac{L^2}{Rt_1k_1} \tag{2.68}$$

and for which it is apparent in Eq.(2.66) that $\Omega_\alpha = \Omega_\gamma\,(1+k_3R(t_3)^{-1})$. The term $k_3R(t_3)^{-1}$ is a recurrent one can be represented by the dimensionless variable Ω_κ,

$$\Omega_\kappa = \frac{k_3R}{t_3}\,, \tag{2.69}$$

which accounts for the relative thermal resistance of the bottom and top layers of the laminate body (represented by the subscript κ, usually relating to conductance in the thermal sciences).

Lastly, variable substitutions were also performed on the boundary conditions, the local temperature variable, and the thermal resistance in the bottom layer (all in order):

1. $\phi_o = T_o - T_{inf}$
2. $\theta_o = T_o - \beta$
3. $\tau(x) = [T(x) - T_{inf}] / \phi_o$
4. $\Delta T = T_i - T_{inf}$ or $\Delta T = Rq_o'' - T_{inf}$ with applied heat flux
5. $R_3 = t_3 / k_3$

Tables 2.3 and 2.4 show the result of applying all of the above variable substitutions to obtain dimensionless equations from the equations in Tables 2.1 and 2.2.

Table 2.3: Summary of the dimensionless two-region fin model in Cartesian coordinates

Parameter	T_i	q_o''
$\tau, 0 \le \lambda \le 1$	$\tau(\lambda) = \left(\frac{\cosh\left(\lambda\sqrt{\Omega_\alpha}\right)}{\cosh\left(\sqrt{\Omega_\alpha}\right)} - 1\right)\left(\frac{\phi_o}{\theta_o}\right)^{-1} + 1$	
$\tau, \lambda \ge 1$	$\tau(\lambda) = \frac{e^{\sqrt{\Omega_\gamma}}}{e^{\lambda\sqrt{\Omega_\gamma}}}$	
Ω_α	$\Omega_\alpha = \Omega_\gamma\left(1 + \Omega_\kappa\right)$	$\Omega_\alpha = \frac{L^2}{t_1 k_1}\frac{1}{R}$
Ω_γ	$\Omega_\gamma = \frac{L^2}{t_1 k_1}\frac{1}{R}$	
$\Delta T/\theta_o$	$\frac{\Delta T}{\theta_o} = \left(1 + \frac{1}{\Omega_\kappa}\right)\left(\frac{\phi_o}{\theta_o} - 1\right)$	$\frac{\Delta T}{\theta_o} = 2\frac{\phi_o}{\theta_o} - 1$
ϕ_o/θ_o	$\frac{\phi_o}{\theta_o} = -\sqrt{1+\Omega_\kappa}\tanh\left(\sqrt{\Omega_\alpha}\right)$	$\frac{\phi_o}{\theta_o} = -\tanh\left(\sqrt{\Omega_\alpha}\right)$
Q'_{lam}	$\frac{Q'_{lam}R_3}{\theta_o L} = \left(\frac{\Delta T}{\theta_o} - \frac{\phi_o}{\theta_o} + 1\right) - \frac{1}{\sqrt{\Omega_\alpha}}\tanh\left(\sqrt{\Omega_\alpha}\right)$	-
Q'_{fin}	$\frac{Q'_{fin}R_3}{\theta_o L} = \frac{1}{\Omega_\kappa\sqrt{\Omega_\gamma}}\frac{\phi_o}{\theta_o}$	
Q'_{simple}	$\frac{Q'_{simple}R_3}{\theta_o L} = \frac{1}{\left(\Omega_\kappa + 1\right)}\frac{\Delta T}{\theta_o}$	-

Table 2.4: Summary of the dimensionless two-region fin model in cylindrical coordinates

Parameter	T_i	q_o''
$\tau, 0 \le \lambda \le 1$	$\tau(\lambda) = \left(\frac{I_0\left(\lambda\sqrt{\Omega_\alpha}\right)}{I_0\left(\sqrt{\Omega_\alpha}\right)} - 1 \right)\left(\frac{\phi_o}{\theta_o}\right)^{-1} + 1$	
$\tau, \lambda \ge 1$	$\tau(\lambda) = \frac{K_0\left(\lambda_r\sqrt{\Omega_\gamma}\right)}{K_0\left(\sqrt{\Omega_\gamma}\right)}$	
Ω_α	$\Omega_\alpha = \Omega_\gamma\left(1+\Omega_\kappa\right)$	$\Omega_\alpha = \frac{L^2}{t_1 k_1}\frac{1}{R}$
Ω_γ	$\Omega_\gamma = \frac{L^2}{t_1 k_1}\frac{1}{R}$	
$\Delta T/\theta_o$	$\frac{\Delta T}{\theta_o} = \left(1+\frac{1}{\Omega_\kappa}\right)\left(\frac{\phi_o}{\theta_o}-1\right)$	$\frac{\Delta T}{\theta_o} = 2\frac{\phi_o}{\theta_o} - 1$
ϕ_o/θ_o	$\frac{\phi_o}{\theta_o} = -\sqrt{1+\Omega_\kappa}\frac{I_1\left(\sqrt{\Omega_\alpha}\right)K_0\left(\sqrt{\Omega_\gamma}\right)}{K_1\left(\sqrt{\Omega_\gamma}\right)I_0\left(\sqrt{\Omega_\alpha}\right)}$	$\frac{\phi_o}{\theta_o} = -\frac{I_1\left(\sqrt{\Omega_\alpha}\right)K_0\left(\sqrt{\Omega_\gamma}\right)}{K_1\left(\sqrt{\Omega_\alpha}\right)I_0\left(\sqrt{\Omega_\gamma}\right)}$
Q_{lam}	$\frac{Q_{lam}R_3}{\theta_o L^2} = \frac{\pi}{2}\left(\frac{\Delta T}{\theta_o} - \frac{\phi_o}{\theta_o} + 1\right) - \frac{\pi}{\sqrt{\Omega_\alpha}}\frac{I_1\left(\sqrt{\Omega_\alpha}\right)}{I_0\left(\sqrt{\Omega_\alpha}\right)}$	-
Q_{fin}	$\frac{Q_{fin}R_3}{\theta_o L^2} = \pi\frac{1}{\Omega_\kappa\sqrt{\Omega_\gamma}}\frac{\phi_o}{\theta_o}\frac{K_1\left(\sqrt{\Omega_\gamma}\right)}{K_0\left(\sqrt{\Omega_\gamma}\right)}$	
Q_{simple}	$\frac{Q_{simple}R_3}{\theta_o L^2} = \frac{\pi}{2\left(\Omega_\kappa+1\right)}\frac{\Delta T}{\theta_o}$	-

The non-dimensional temperature profiles obtained from the equations for constant temperature and constant heat flux sources in Cartesian coordinates in Table 2.3, with varying L, are each shown in Fig.2.7. The non-dimensional temperature profiles, τ, in Fig.2.7 represent 0.1 mm thick laminate films with two 0.04 mm thick polyethylene layers and one 0.02 mm thick Al layer and a convection coefficient, h, equal to 25 W m^{-2} K^{-1}.

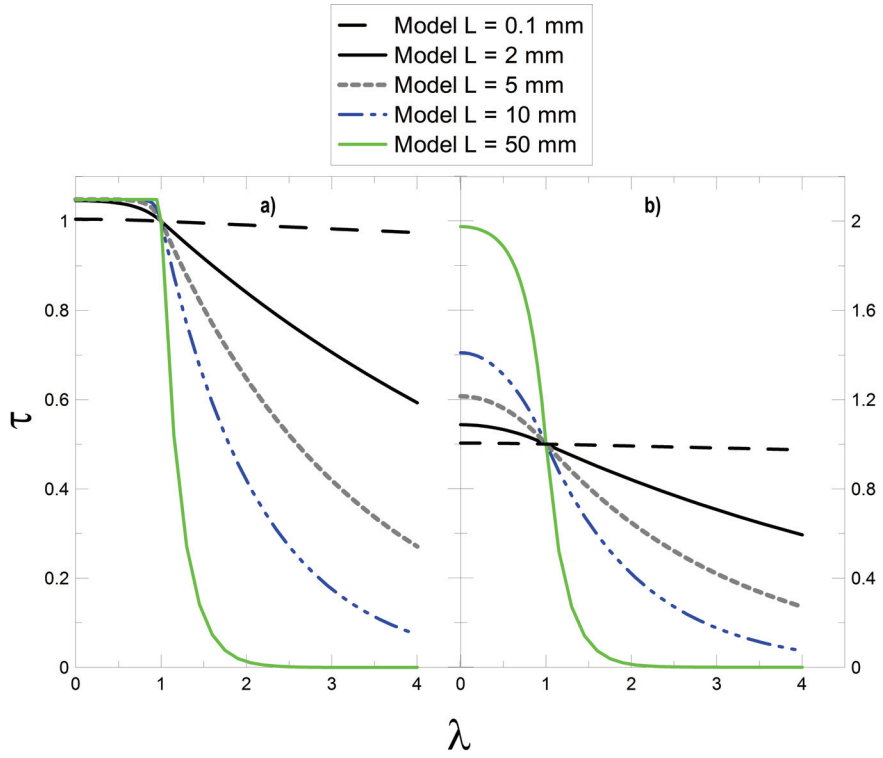

Figure 2.7: Non-dimensional temperature profiles, τ, in Cartesian coordinates with varying L: a) shows the solutions for constant temperature sources and b) shows the solutions for constant heat flux sources. The solutions represent 0.1 mm thick laminate film with two 0.04 mm thick polyethylene layers and one 0.02 mm thick Al foil layer, with h = 25 W m^{-2} K^{-1}.

The solutions with smaller heated lengths, L, in Fig.2.7a) and b) show a greater extent of heat penetration into the fin regions relative to L, therefore emphasizing the observation from Fig.2.6 that the relative contribution from Q'_{fin} to the overall rate of laminate heat transfer (η) diminishes at the larger values of L. Also note that the indirect link between the Al temperature and constant heat flux sources is apparent in Fig.2.7b) in that the value of τ in the heated region increases from $\lambda = 1$ to $\lambda = 0$. The farther away the left edge of the heat source from the heated region boundary, the more inaccessible the local heat flux at the far left edge becomes to the fin region heat transfer. This condition begins to dominate the heated region when the τ profile can be seen to reach a plateau approaching $\lambda = 0$, as it does for L = 50 mm in Fig.2.7b).

The non-dimensional temperature profiles for cylindrical coordinates from the equations in Table 2.4 for constant temperature and constant heat flux sources, with

varying L, are each shown in Fig.2.8. The laminate films of the same thicknesses and composition as in Fig.2.7 are also represented in Fig.2.8.

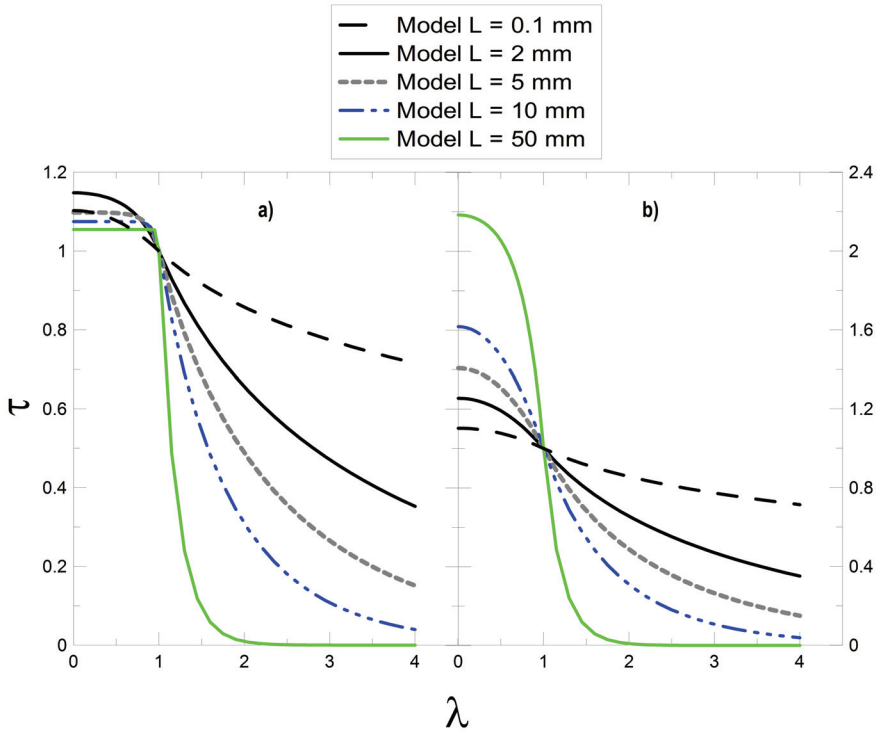

Figure 2.8: Non-dimensional temperature profiles, τ, in cylindrical coordinates with varying L: a) shows the solutions for constant temperature sources and b) shows the solutions for constant heat flux sources. The solutions represent 0.1 mm thick laminate film with two 0.04 mm thick polyethylene layers and one 0.02 mm thick Al foil layer.

Just as it was for the profiles in Cartesian coordinates in Fig.2.7, the non-dimensional temperature profiles for cylindrical coordinates in Fig.2.8 show the same features related to the extent of heat penetration into the fin region at lower values of L as well as the diminishing contribution of Q_{fin} to the overall rate of laminate heat transfer (η). The profiles in Fig.2.8 also show that the cylindrical two-region fin model predicts a larger fin region influence on the respective heated regions compared to the equivalent Cartesian coordinate profiles in Fig.2.7. Plateaux for τ in the cylindrical coordinate heated regions are largely suppressed, imposing strong curvature instead, even in the profiles for constant temperature heat sources. This is largely due to the absence of a saturation limit for Q_{fin} in cylindrical coordinates (section 2.2.4).

Lastly, the relative magnitude of the fin region heat fluxes can be gauged from the profiles in Fig.2.7 and 2.8 when comparing those with the same values of L. Their slopes

at the inflection point, $\lambda = 1$, are equivalent to their magnitudes of dT/dx or dT/dr in dimensional coordinates, therefore representing their magnitudes of Q'_{fin} and Q_{fin} from Eqs.(2.27) and (2.48), respectively.

2.3 RESULTS AND DISCUSSION

Confidence in the two-region fin model predictions is pre-requisite to using them in design calculations for salt hydrate latent heat storage encapsulation, multi-ply cookware, and even heat spreaders for electronics cooling. As the first means of doing so, finite element simulations were evaluated for a thin three-component film (40 μm/20 μm/40 μm polyethylene/Al/polyethylene, the same as the laminate film inside Tetra Brik cartons) in Cartesian and cylindrical coordinates in order to validate the two-region fin model for steady-state and transient, 2D and axi-symmetric solutions.

The finite element models were prepared in COMSOL Multiphysics 4.2a to represent a 100 mm long laminate film of the composition mentioned above. The fundamental equations were added using the heat transfer in solids module included in COMSOL and applying a convective cooling boundary condition on the top surface (with specified h) and either constant temperature or heat flux boundary condition over a portion (L) of the bottom surface. The materials model for polyethylene (all nominal properties) was specified as $C_p = 2\frac{\text{kJ}}{\text{kgK}}$ (NIST, 2012), $k = 0.4\frac{\text{W}}{\text{mK}}$ (Smith, 1998), and $\rho = 900\frac{\text{kg}}{\text{m}^3}$ (Mark, 2009), and the Al as $C_p = 0.9\frac{\text{kJ}}{\text{kgK}}$, $k = 260\frac{\text{W}}{\text{mK}}$, and $\rho = 2{,}700\frac{\text{kg}}{\text{m}^3}$ (Perry and Green, 2008). Mesh convergence was achieved in both models using 48,000 2$^{\text{nd}}$ order quadrilateral mesh elements (see mesh in Fig.2.9), shown by the computed values of Q'_{lam} and Q_{lam} at varying the number of mesh elements. Convergence is shown in Fig.2.10.

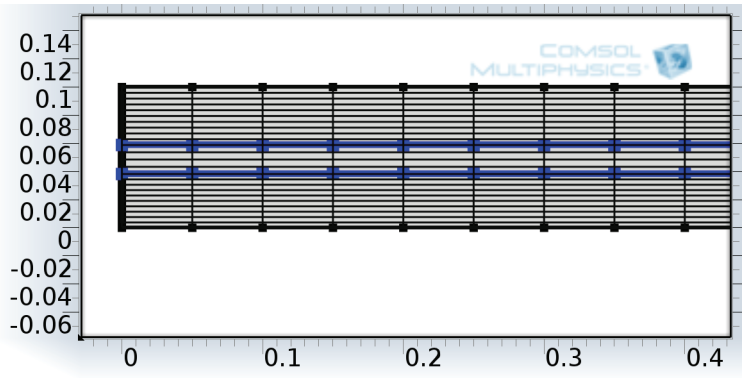

Figure 2.9: Close-up of the Cartesian finite element geometry in COMSOL Multiphysics 4.2a showing the quadrilateral mesh elements (48,000 total) selected from the convergence study. Both axes are in mm.

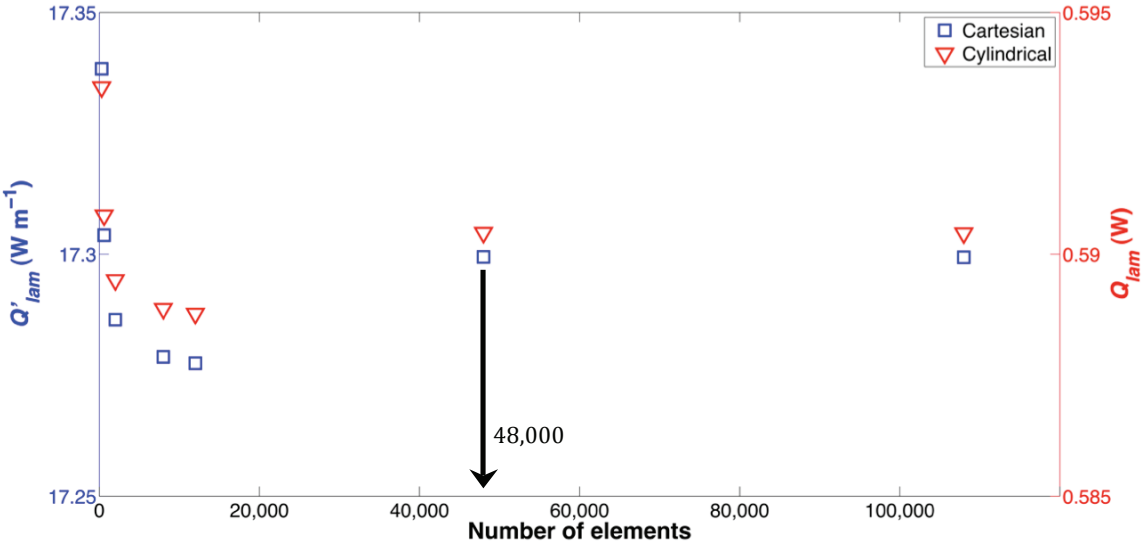

Figure 2.10: Mesh convergence plot for 2D (Cartesian) and axi-symmetric (cylindrical) models in COMSOL Multiphysics 4.2a. Q'_{lam} and Q_{lam} were the chosen for the respective convergence criteria for the constant temperature heat source boundary condition (T_i = 50˚C) and forced cooling in air (h = 25 W m^{-2} K^{-1}) at 20˚C.

A qualitative plot of the resulting 2D laminate heat conduction is shown in Fig.2.11. The red arrows represent the magnitude and direction of conduction heat transfer and the dashed line represents the location of the heated region boundary. Although Fig.2.11 shows the heat conduction results for only one of the simulations in COMSOL Multiphysics, it confirms the strong tendency for the axial heat conduction in the high thermal conductivity metal layer to dominate the overall heat transfer of the system, on which the two-region fin model relies.

Figure 2.11: 2D laminate heat conduction with a constant temperature heat source simulated in COMSOL Multiphysics 4.2a. The red arrows represent the direction and magnitude of conduction heat transfer and the dashed line represents the location of the heated region boundary.

Good agreement between the two-region fin model and the finite element models in COMSOL, with relaxed assumptions, would prove that the simplifying assumptions in section 2.2 are valid in typical cases involving laminate structures with high thermal conductivity metal cores. Figure 2.12 shows the superimposed dimensionless temperature profiles, τ, from the steady-state finite element simulations and the two-region fin model evaluated for L between 2 and 50 mm, constant temperature (left) and constant heat flux heat sources (right), and for the Cartesian and cylindrical coordinate systems. Their agreement is exact in all cases, thus achieving high accuracy validation for the results from the two-region fin model in the applicable conditions for assumption #4, as discussed in section 2.2.1.

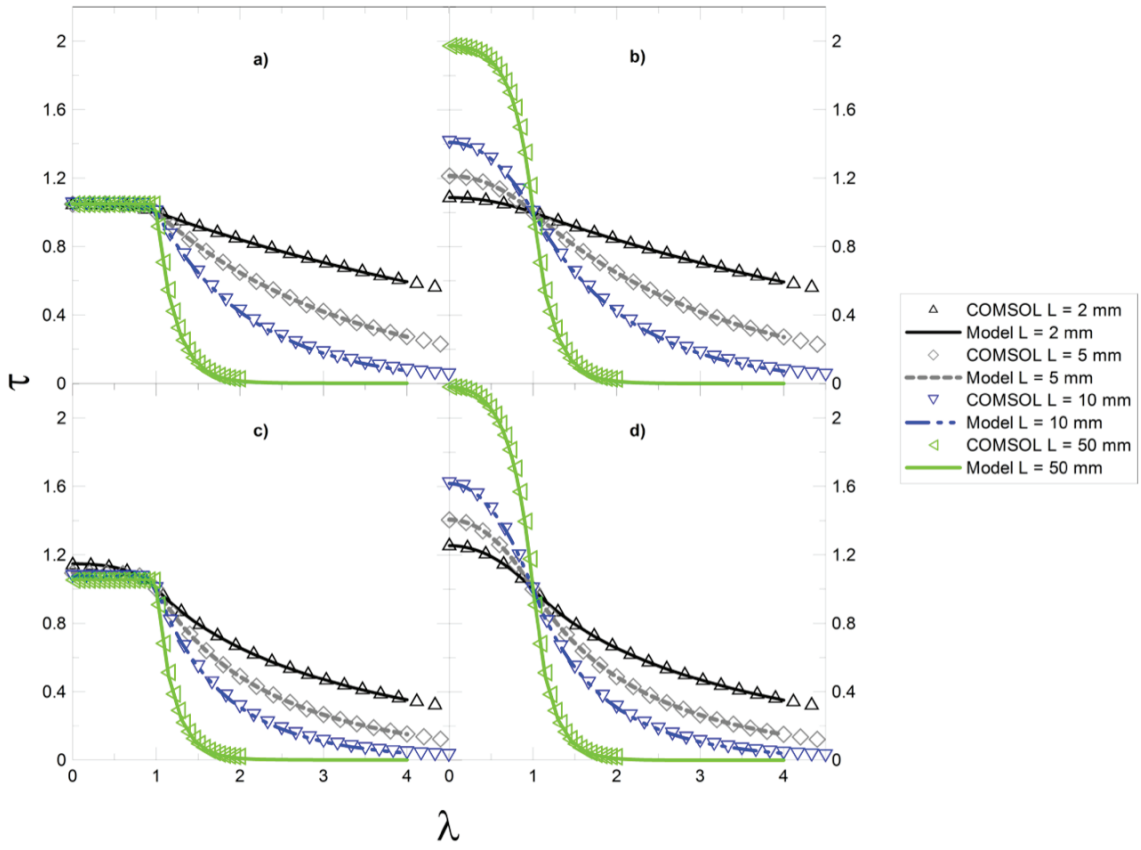

Figure 2.12: Validation of the 1D solution (two-region fin model) with the 2D numerical solutions using COMSOL Multiphysics 4.2a. Panels a) and b) show the dimensionless temperature profiles in Cartesian coordinates with the T_i and q_o'' heat sources respectively; c) and d) show these solutions in cylindrical coordinates.

Note that in the two types of profiles, and the respective coordinate systems, the objective with the q_o'' heat source is temperature uniformity while that of the T_i heat source is a greater rate of heat transfer. Temperature uniformity appears easiest to achieve with rectangular heat sources rather than circular ones (Fig.2.12b has a greater extension of τ in the fin region, $\lambda \geq 1$, and lower peak values in the heated region, $0 \leq \lambda \leq 1$ than does Fig.2.12d, and greater still for L = 0.1 mm in Fig.2.7 in section 2.2.5). An increased rate of heat transfer is most easily accomplished with circular heat sources since larger magnitudes of slope at $\lambda = 1$ in cylindrical coordinates than those in Cartesian coordinates for the same values of L indicate greater capacities for heat transfer in the fin region (greater fin region heat conduction in Fig.2.12c than in Fig.2.12a). The comparison of slopes at $\lambda = 1$, $d\tau/d\lambda$, are only valid for the same value of L since their equivalence to the

relative magnitudes of *dT/dx* or *dT/dr* relies on a fixed scale of λ (equivalence of $d\tau/d\lambda$ to *dT/dx* or *dT/dr* in section 2.2.5).

In design, however, parameter selection is usually dictated by the limiting cases. So, good long-term heat storage PCM encapsulation would have to improve heat transfer rates for rectangular expanding crystal fronts (of course performing even better for circular expanding crystal fronts) and a multi-ply cook-pot would have to improve temperature uniformity for circular wound heating elements (the element portions in the middle having the strongest curvature while the outside portion would begin to resemble rectangular elements).

Validation was also performed on the basis of heat accumulation in transient models in order to evaluate the argument presented in section 2.2.1 for using the two-region fin model in pseudo steady-state analysis. The values of the heat transfer rate in the finite element model transient solution and the two-region fin model steady-state solution were used in Fig.2.13 to identify the impact of heat accumulation on the two-region fin model predictions. The transient finite element model in Cartesian coordinates had a constant rate of heated length expansion ($\dot{L} = 3\frac{\text{mm}}{\text{min}}$), while the cylindrical model had both a solution with the same imposed rate of heated length expansion ($\dot{L} = 3\frac{\text{mm}}{\text{min}}$) and another with a constant rate of heated area expansion ($\dot{A} = 150\frac{\text{mm}^2}{\text{min}}$).

It is only during the first interval, in either pane of Fig.2.13, that a discernable difference is observed between the steady-state heat transfer rate of the two-region fin model and the transient solutions in COMSOL (either Cartesian or cylindrical), for which the logical reason is the need for heat accumulation for the system to depart from the initial conditions. For the results in cylindrical coordinates (bottom pane in Fig.2.13), however, the higher initial rates of heated length expansion ($\dot{L}$) from the imposed fixed rate of area expansion ($\dot{A}$) than the observed from the transient solution with the fixed rate of heated length expansion ($\dot{L}$) were inconsequential to the comparison between the finite element transient solutions and the steady-state two-region fin model. Thus, high accuracy validation was achieved for the valid use (recall section 2.2.1) of the two-region fin model in pseudo steady-state analysis.

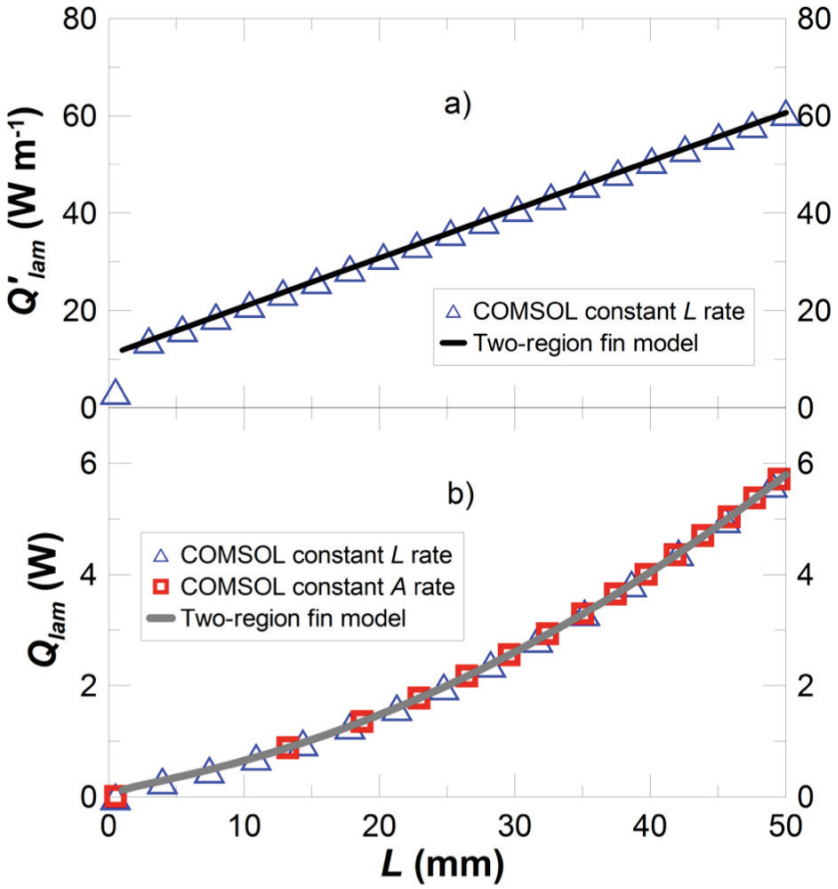

Figure 2.13: Validation of the two-region fin model with respect to the 2D transient solutions obtained in COMSOL Multiphysics 4.2a. Panel a) shows the solutions in Cartesian coordinates and a prescribed transient of constant $\dot{L}$ = 3 mm min^{-1}; b) shows the solutions in cylindrical coordinates and the prescribed transients $\dot{L}$ = 3 mm min^{-1} and $\dot{A}$ = 150 mm^2 min^{-1}.

2.4 TWO-REGION FIN MODEL IN DESIGN

The two-region fin model therefore provides sufficiently detailed and accurate solutions in the realm of its principal assumptions (section 2.2), which are reasonably inclusive of design situations arising from salt hydrate encapsulation for latent heat storage, multi-ply cookware and electronics cooling. The equations in either Cartesian or cylindrical coordinates are all explicit and easily implemented into spreadsheets and commercial modelling software.

In the cases where the applied finite heat source is a heat flux device, obtaining uniform dimensionless temperature profiles in the heated region and far reaching profiles in the fin region are the objectives and plots such as in Figs.2.7, 2.8 and 2.12 should be studied. In the case of salt hydrate encapsulation, the design metric is η, which should be

maximized to a practical extent using the plots in Fig.2.14 that cover large sections of the possible solution domain in dimensionless variables (Ω_γ and Ω_κ) in order to select a design basis. Design constraints would either restrict the value of Ω_γ (Eq.(2.68) relating the path length of heat spreading, most importantly the selection of L, t_1, and k_1) or Ω_κ (Eq.(2.69) relating to the thermally resistive layers and convective cooling, so R, t_3, and k_3), for which a suitable range of values of the unconstrained variable would be selected to yield the desired values of η, then obtaining the exact parameters from the variable definitions in Eqs.(2.68) and (2.69). For instance, using the Tetra Brik laminate film that was used in the finite element model, but with $k_1 = 260$ W m^{-1} K^{-1} (Perry and Green, 2008) and $h = 50$ W m^{-2} K^{-1} ($\Omega_\kappa = 210$), one could expect heat transfer gains between 960 and 19% in Cartesian coordinates and 5700 and 42% in cylindrical coordinates, respectively, both for 1 mm $\leq L \leq$ 50 mm ($0.0093 \leq \Omega_\gamma \leq 23$).

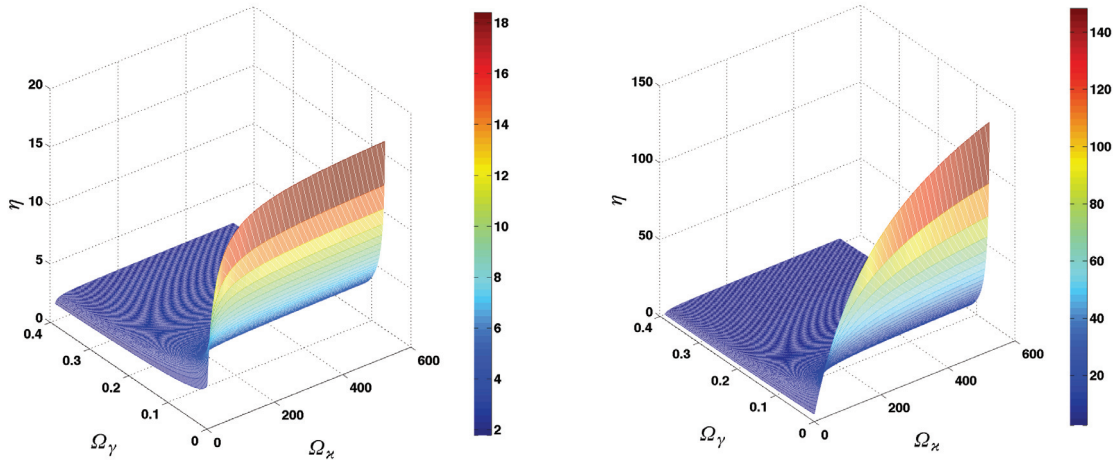

Figure 2.14: Effectiveness, η, domain maps in dimensionless coordinates Ω_γ and Ω_κ for Cartesian (left) and cylindrical coordinates (right).

One could even consider applying the two-region fin model to laminate systems having only two-layers (q_o'' finite heat sources only) or more than three layers of metals, or polymers and metals. The model would remain valid so long as there is a single inner layer with significantly higher thermal conductivity than all the others such that assumption #4 still holds. All adjacent layers that are non-heat spreading can be combined into a lumped resistance (R) for the top layer and a lumped conductivity for the bottom layer (k_3).

CHAPTER 3: EXPERIMENTAL VALIDATION

3.1 INTRODUCTION

The following sections give detailed accounts of the validation experiments that were performed to confirm two-region fin model behaviour in real laminate films. These were conducted under conditions of natural convection and forced external convection for cooling the top surface of the laminate while also heating the bottom surface with either thin rectangular heaters or thin circular heaters.

3.2 EXPERIMENTAL METHODS

Experiments were conducted for the constant heat flux boundary condition using rectangular, flexible silicone rubber, fibreglass insulated heaters and circular, thin Kapton® heaters from Omega Engineering Inc. (controlled by a STACO 0-140VAC VARIAC, ± 0.5V), resting plainly behind a flattened laminate film secured to a sheet of 1" thick polystyrene foam insulation (backing and border clamped thereto). Figure 3.1 shows this arrangement for mounting laminate films for the constant heat flux experiments.

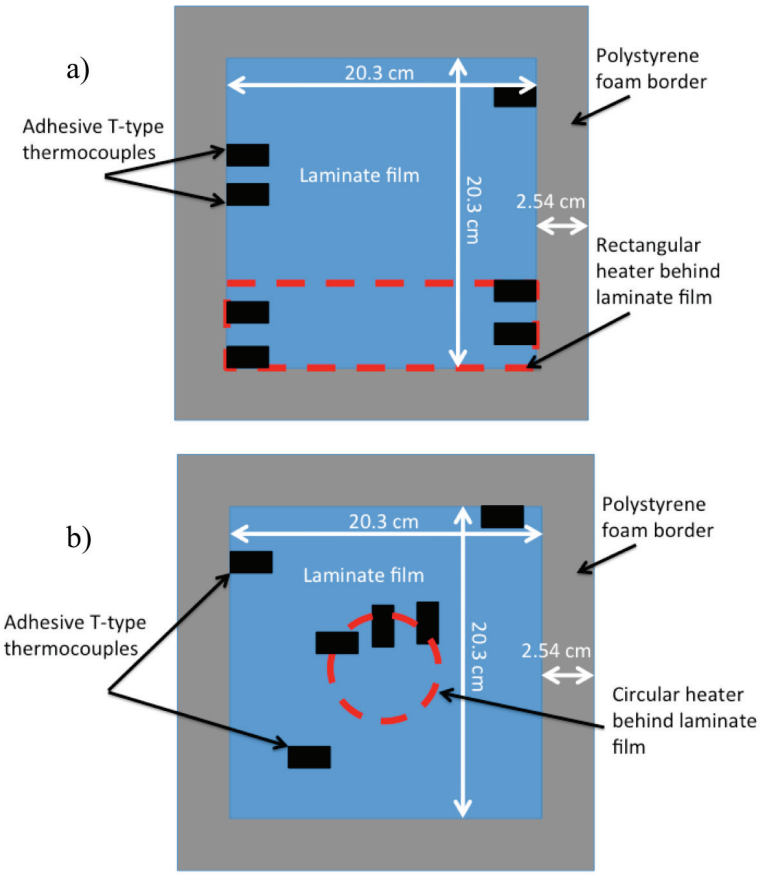

Figure 3.1: Laminate film test mount schematics: a) mounted laminate with rectangular heater; b) mounted laminate with circular heater.

The laminate film was put in place on the foam sheet first using electrical tape along its edges (trapping only a very thin layer of air underneath the laminate film), then clamped in place with the foam border (the laminate film slightly exceeding the inner dimensions of the foam border, but not protruding from the mounting frame). The exposed laminate surface was allowed to exchange heat through either natural or external forced convection.

Class 1, T-type thermocouples adhered to the surface of the laminate (affixed with integrated transparent adhesive strips, model SA1XL-T from Omega Engineering Inc.) recorded the surface temperatures in order to calibrate infrared thermographic images from an Indigo Merlin IR camera. Image intensities along cut lines were used to construct temperature profiles after calibration. Thermocouples on the surface of the laminate distorted local temperature fields (adding thermal resistance greater than that of the film), so they were kept along the outer edges of the film. Figure 3.2 shows the arrangement of

thermocouples and their impact on the local temperature field. Experimental validation was performed for rectangular heat sources of heated lengths (L) 25.4, 50.8, and 76.2 mm and rated power density of 0.39 W cm^{-2}. Circular heat source validation was performed using 50.8 and 76.2 mm diameter ($2L$) heaters and rated power densities of 1.6 and 0.39 W cm^{-2}, respectively.

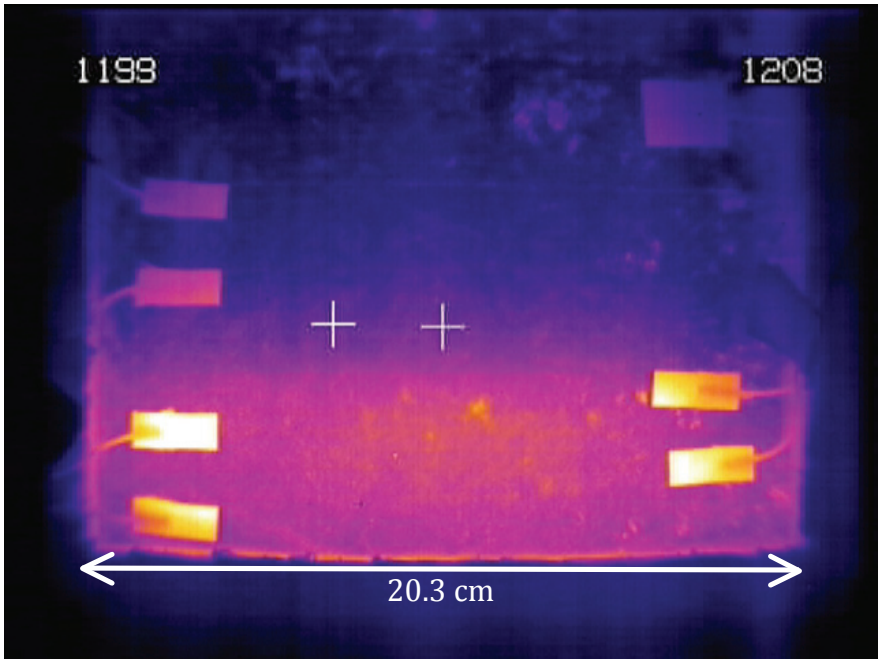

Figure 3.2: IR thermographic image showing thermocouples on Tetra Pak laminate film using an L = 50.8 mm rectangular heater. The crosshairs and numbers on the image were from internally calibrated profiles unrelated to the experiment.

Some calibration was necessary for experiments using cooling of the free surface by natural convection (vertical exposure, heater on the bottom). Natural convection experiments were run with the heater at the top during commissioning trials, but these did not appear promising since there always appeared a region of even higher temperatures within a few millimeters from the top of the film (Fig.3.3). This was thought to occur due to the protruding polystyrene foam that secured the boarder of the laminate film sample, which would confine a separate natural convection boundary layer flow from the principal one rising along the length of the sample film. Conducting the experiments with the heater on the bottom alleviated this condition.

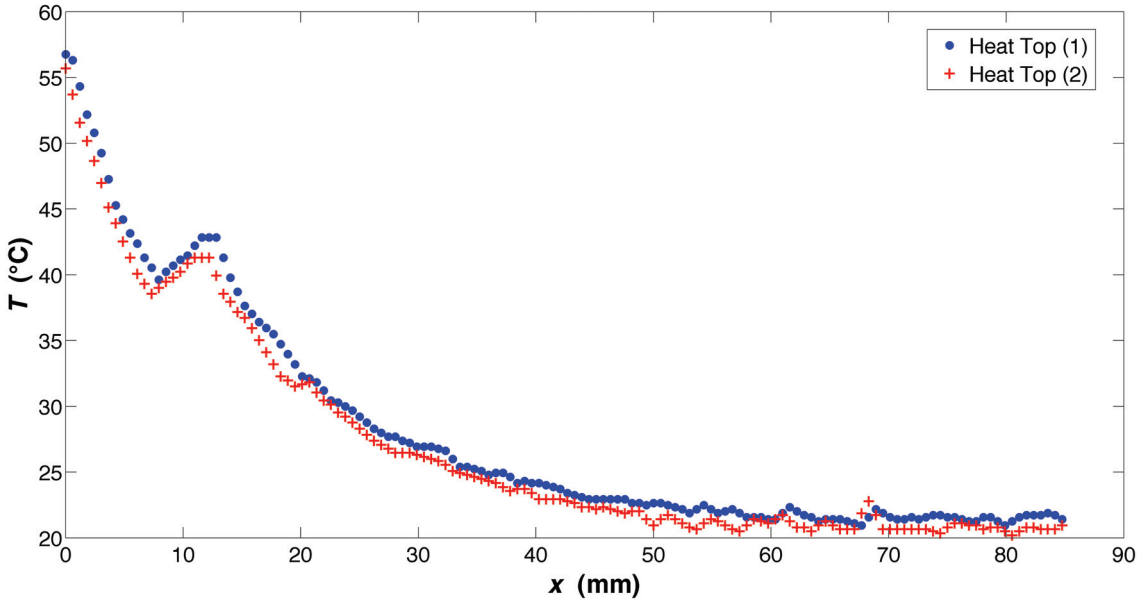

Figure 3.3: Measured temperature profiles from experiments with the heater placed at the top of the laminate film sample assembly with natural convection only. The apparent anomaly in the principal convection current was always located within ~10 mm from the top of the film (polystyrene border).

Only one rectangular heater experiment and all the circular heater experiments were performed using external, impinging forced convection. Natural convection could not be used in the evaluation of circular heaters since radial uniformity of the system could not be ensured in this condition (1D conduction condition). Airflow for forced cooling was supplied by a duct fan positioned nearly perpendicular to the heated film to avoid obstructing the IR camera.

The laminate films under examination were all sourced from used aseptic cartons, in this case 1 and 2 L Tetra Brik, which were separated from the outer paperboard and polyethylene layers by water immersion and light agitation/rubbing at room temperature for 35 min. This process mimics high consistency hydropulping done in paper mills to recycle the paperboard from cartons (see section 4.2). Other samples were obtained from the high consistency hydropulper at Klabin's paper mill in Piracicaba, Brazil.

The thermal conductivity of the laminate films measured at 30˚C in a Mathis Instruments TC30 was 0.41±0.05 W m^{-1} K^{-1}; the thermal conductivity of polyethylenes (used in films) is between 0.33 and 0.46 W m^{-1} K^{-1} (Smith, 1998) while that of Al is 260 W m^{-1} K^{-1} (Perry and Green, 2008). The TC30 determines the thermal conductivity of film or block samples at ambient pressure and 30˚C by measuring the rise in surface

temperature over a short period, with constant heat flux, and applying a three-parameter calibration based on a series of standards (e.g. insulating foam with $k = 0.03051$ W m^{-1} K^{-1}, pyrex with $k = 1.15$ W m^{-1} K^{-1}, Delrin® with $k = 0.3768$ W m^{-1} K^{-1}, and Torlon® with $k = 0.5428$ W m^{-1} K^{-1} (Mathis, 2002)).

3.2.1 DATA ACQUISITION

Continuous data gathering was accomplished with the use of a National Instruments CompactDAQ and a NI 9213, sixteen-port thermocouple module operated via LabView 2011. Digital video capture from the IR camera was imported with Pinnacle Studio HD v14. Still-frames were extracted, noting their timestamps.

Heat fluxes were determined by reading the supplied voltage from the VARIAC (integrated digital voltmeter) and calculating the heat flux from the rated heater power in the function $q''_o = \frac{PV^2}{(115\text{V})^2}$, where P and V are the rated power and supplied voltage, respectively. This was the method recommended by the heater manufacturer. Although this method is an indirect measurement of heat flux and neglects changes in the heat wire resistance at higher temperatures, albeit small, it shall be later shown that the effect on the model fit to experimental temperature measurements does not require absolute heat flux accuracy.

Thermographic video still-frames and thermocouple data were imported into Matlab R2011a for which the video frame timestamps were used to extract the thermocouple data with the nearest recorded time intervals. Pixel information in proximity to the thermocouples in the thermographic still-frames was recorded and converted from RGB format to grayscale using the built-in features of the Image Processing Toolbox in Matlab: the function *improfile* to extract the pixel data from cursor selections on the active picture and *rgb2gray* to apply the built-in algorithm to integrate RGB data to single grayscale intensities in the range 0-255. The thermocouples adhered to the surface of the sample laminate represented the only known temperatures prior to IR-thermocouple calibration, so their data were taken to identify the temperatures associated with the pixel intensities recorded in their locations on the IR-thermographs. IR calibration was performed in this manner, giving linear plots of thermographic pixel intensity (grayscale) and temperature for each thermographic frame (Fig.3.4).

Calibrations were only valid for each individual thermographic frame and associated timestamp since the IR camera produced a unique colour scale for each frame.

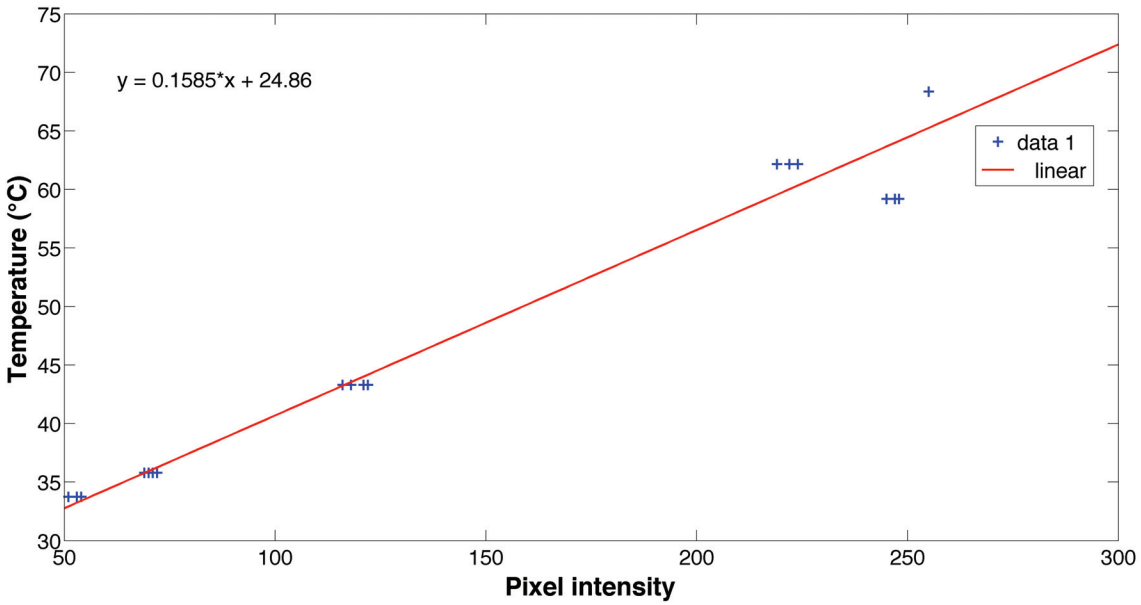

Figure 3.4: Calibration plot of IR thermographic grayscale intensity (pixel intensity) and thermocouple temperature measurements. This calibration corresponds to measurements for an L = 76.2 mm naturally cooled rectangular heater operated at 0.059 W cm^{-2} and gave an R^2 value of 0.9974.

The calibration in Fig.3.4 is typical of all those performed in the course of the experiments. Smaller deviations and a better quality of fit were always observed at the lower measured temperatures, while the opposite was true at the highest temperatures; both temperature limits would depend on the actual range measured in the IR thermograph. One can notice the inherent difficulty in making IR measurements nearing the scale maximum, since grayscale intensities can only occupy the integer range 0-255. It is important, then, that the desired measurement be contained well within the middle of the calibrated range and that the measured temperature range does not severely diminish the grayscale resolution.

3.3 RECTANGULAR HEAT SOURCES

3.3.1 NATURAL CONVECTION

The temperature profiles measured by IR thermography for the Al foil of the laminate pouches (LDPE being transparent to IR), naturally cooled and with heaters operated at 0.059 W cm^{-2}, are shown in Fig.3.5. Predictions from the two-region fin model are also

shown in Fig.3.5 for the same experimental conditions. Note that sudden spikes in any of the temperature profiles measured by infrared thermography in this thesis are due to the presence of residual paperboard fibres in the cut-lines that were extracted in Matlab, which have significantly different infrared properties than the does Al foil being measured.

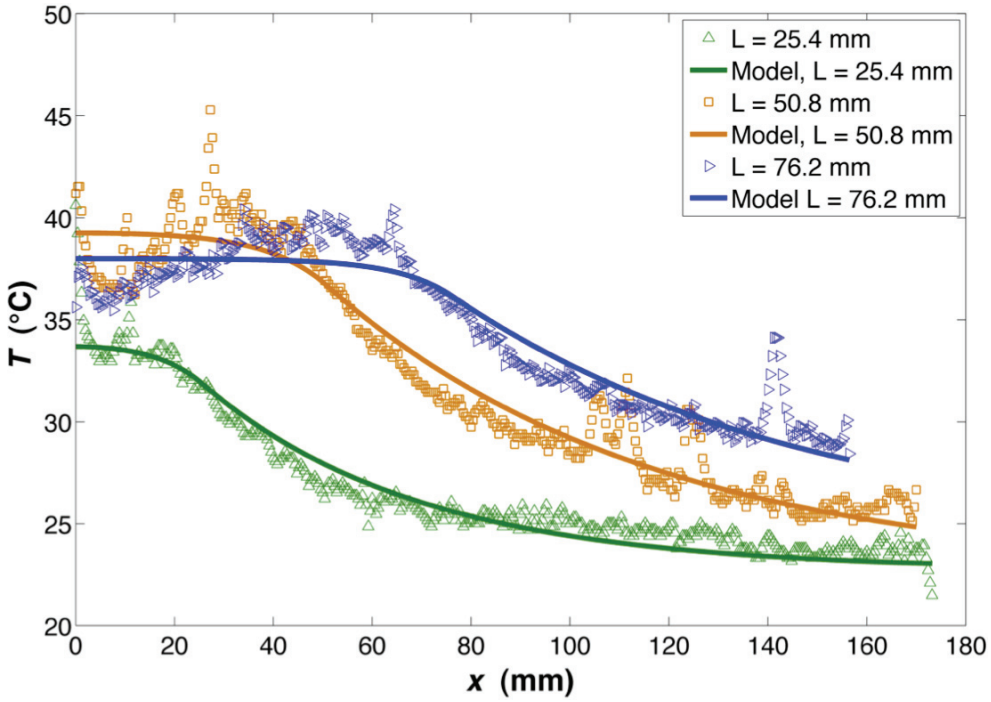

Figure 3.5: Experimental validation of the two-region fin model in Cartesian coordinates using two adjustable heat transfer coefficients to achieve best fit in conditions of natural convection (section 2.2.4). All heaters operated at 0.059 W cm^{-2}.

The model predictions were obtained by adjusting the value of the heat transfer coefficient in both the heated and unheated regions, h_h and h_f, separately, in a least-squares method of best fit (using *fminsearch* for two-parameter optimization in Matlab). Although h_h and h_f are not themselves predicted, since they vary in the system due to the local intensity of natural convection, the model assumes h_h and h_f are uniform over each of their respective regions (see section 2.2.4) and makes no attempt to determine them from equations. Obtaining h_h and h_f by best fit still satisfies the energy balance and avoids further error from convection correlations, therefore providing a better evaluation of temperature, as well as compensating for inaccuracies in the measurement of heat flux (section 3.2.1). Undervaluation of the measured heat flux would cause the least-squares determination of h_h and h_f to predict lower values of the convection coefficients in order

to satisfy the imposed energy balance in the two-region fin model, while the opposite would occur due to overvaluation of the measured heat flux.

Since the samples were mounted vertically, with the heat source on the bottom, natural convection favoured the lowest regions, while promoting higher temperatures in the farther reaches of the heated region (as can be seen in Fig.3.5) and imposing low convective cooling in the unheated region.

Table 3.1 shows the values of the natural convection heat transfer coefficients for the model results in Fig.3.5 that were determined by two-parameter least-squares optimization in Matlab. The highest values are naturally in the heated regions, h_h's, and the highest value overall was found for the heater with the smallest heated length, L, which corresponds well with natural convection theory for vertical cooled surfaces with constant heat flux whereby h is inversely proportional to the characteristic length of the system. However, the overall rate of heat transfer increases with the size of the system, despite decreasing values of h. The natural convection heat transfer coefficients listed in Table 3.1 are also in the correct order of magnitude for natural convection in air at ambient conditions.

Table 3.1: Two-region fin model natural convection heat transfer coefficients determined by least-squares two-parameter optimization in Matlab for the profiles in Fig.3.5.

L (mm)	h_h (W m^{-2} K^{-1})	h_f (W m^{-2} K^{-1})
25.4	52.9	2.72
50.8	35.6	1.22
76.2	43.2	1.03

The temperature measurements in the heated regions in Fig.3.5 were subject to calibration uncertainties (details in section 3.5) between 1.3 and 2.0˚C for the 76.2 mm heater, 1.5 and 1.8˚C for the 50.8 mm heater, and 1.9 and 2.0˚C for the 25.4 mm heater. IR calibrations improved at the cooler temperatures of the unheated region: uncertainties were between 0.5 and 1.3˚C, 1.0 and 1.8˚C, and 1.8 and 1.9˚C for the 76.2 mm, 50.8 mm, and 25.4 mm heaters, respectively. Error propagations from the two-region fin model (details in section 3.5), due to position, AC voltage and temperature uncertainties, were between 0.57 and 0.75˚C, 0.60 and 0.83˚C, and 0.51 and 0.66˚C for the 76.2 mm, 50.8 mm, and 25.4 mm heaters, respectively. Therefore, predicted temperature profiles

matched closely with those from IR measurements and predictions were contained well within the measured temperature profile uncertainties.

Overall validation of the Cartesian coordinates two-region model with natural convection was achieved with medium to high accuracy with respect to the appearance of good two-region fin model fit to the features of the experimental data, obtaining values of h_h and h_f in the correct order of magnitude, and the width of the overlapping model error propagations by measurement uncertainties. Specifically, high accuracy validation was achieved for the two-region fin model predictions of the fin region temperatures, while medium accuracy was achieved for the heated region two-region fin model predictions. These validation criteria formed the bases for all of the subsequent validation exercises in this chapter.

3.3.2 FORCED CONVECTION

Laminate heating with a rectangular heater and cooled by forced convection was evaluated for the 76.2 mm heater only. The result, shown in Fig.3.6, was intended to produce a result more closely related to the conditions of channel flow as would be encountered in cases of long term PCM heat storage. However, the method of exerting external forced convection normal to the laminate's surface could not ensure complete homogeneity of the convection coefficient so the model fit for the two-region fin model was still performed using h_h and h_f. The values determined by least-squares were $h_h = 65.8$ W m^{-2} K^{-1} and $h_f = 14.0$ W m^{-2} K^{-1}, clearly showing that convection cooling was more effective under external forced convection than natural convection (see Table 3.1).

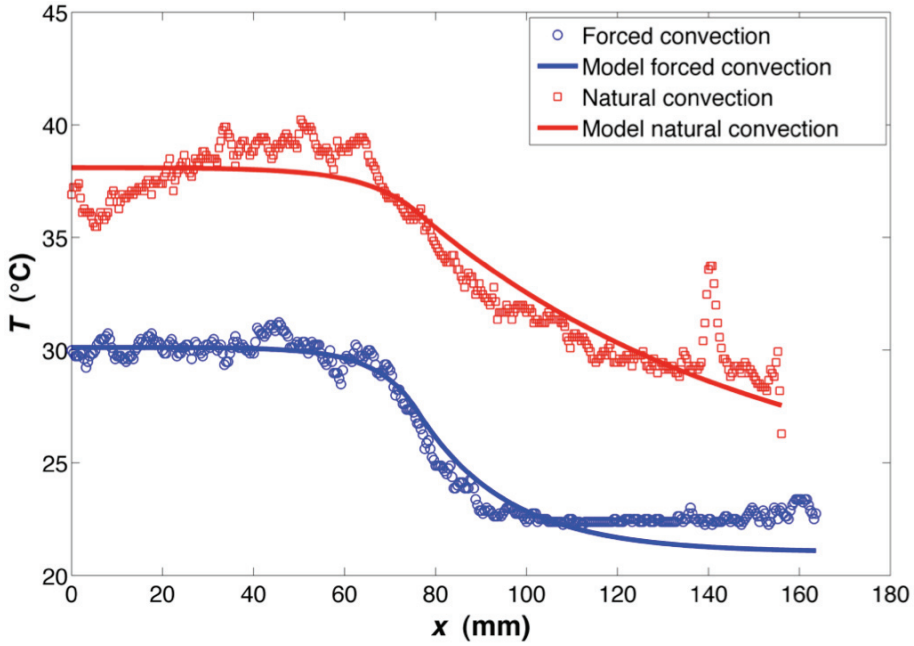

Figure 3.6: Experimental validation of the two-region fin model in Cartesian coordinates for the 76.2 mm heater only, operated at 0.059 W cm^{-2}, and with either natural or external forced convection.

The most apparent feature, or lack thereof, of the 1D temperature profile with forced convection in Fig.3.6 is the improved uniformity in the heated region. Forced convection induces greater confinement of the boundary layer flow next to the polystyrene frame protruding around the sample, thus abating the profile inhomogeneity always present with natural convection (section 3.3.1). Consequently, the two-region fin model produces a better fit in the heated region of Fig.3.6, with forced convection, than with natural convection in Fig.3.5. The fit to the descending slope in the fin region also appears to have improved due to forced convection, but the lower plateau of the forced convection profile diverges and remains at a higher temperature than the ambient temperature measured directly by thermocouple. It was noted, however, that this disagreement could be eliminated by substituting the far-end temperature from the measured profile with forced convection for the ambient temperature recorded separately by thermocouple. It is likely the latter was adversely affected by the lower quality of the IR-thermocouple calibration, being subject to large uncertainties, around 2.8˚C over the entire profile domain in Fig.3.6. A principal reason was the sharp decline in thermocouple temperatures from the heated region to the fin region, such that intermediate temperatures could not be recorded and used in the calibration. Instead, the calibration relied most heavily on the

domain limit values of all of the experiments. The two-region fin model error propagation was minor compared to the IR-thermocouple calibration uncertainty, only ranging between 0.50 and 0.58˚C.

The model prediction therefore remained within the region of measurement uncertainty. Two-region fin model validation for forced convection in Cartesian coordinates was achieved with medium to high accuracy, although having greater accuracy in the heated region than was achieved for natural convection (section 3.3.1).

3.3.3 CONSTANT TEMPERATURE VALIDATION

Validation for constant heat flux was deemed sufficient to claim good predictive strength of constant temperature finite heat sources (change in boundary condition only), relating to the objective of supercooled PCM encapsulation. Constant temperature heat source experiments were not conducted due to the difficulty of using liquid heat transfer fluid at high flow rate to simulate a PCM over a fixed area and maintaining a fixed temperature. In contrast, constant heat flux experiments are simple to prepare and operate and do not require the use of liquids.

The temperature profiles in the heated region with T_i are simpler than with q''_o. The most important temperature profile features for the model to predict are the slope at the inflection point ($x = L$, edge of the heated boundary) and the temperature decay in the unheated region (fin region), shown in Fig.3.5 and 3.6. Qualitative fit of the two-region fin model predictions to the slope of the measured temperature profiles at their inflection points and the temperature profiles in the fin region, as well as their respective widths of the model error propagations overlapped by the measurement uncertainties were used in the validation assessments for constant heat flux. Their validation accuracies were consistent with the medium to high accuracy experimental validations reported in this chapter.

3.4 CYLINDRICAL HEAT SOURCES

Temperature profiles for the circular heaters ($2L$ = 50.8 and 76.2 mm) with forced external convection necessitated judgments to correctly ascertain the true diameter of the heater behind the laminate film in the IR thermographs. The direction of the 1D heat conduction in the case of rectangular heaters could be easily inferred from the heater

orientation to the vertical, but could not be ascertained for the circular heaters (see Fig.3.1). The location of the heaters' diameter at 0˚ from the horizontal needed to be determined as well as possible since IR thermography does not reveal physical features very well. Figure 3.7 shows thermographs of the two sizes of heaters used for validation, and drawing the largest possible horizontal line across each heated circle in a Matlab figure window indicated the closest diameter that could be extracted from the images using the function *improfile*. The profiles were fit to the models using the radii, so only half the cut line could be used to extract a profile.

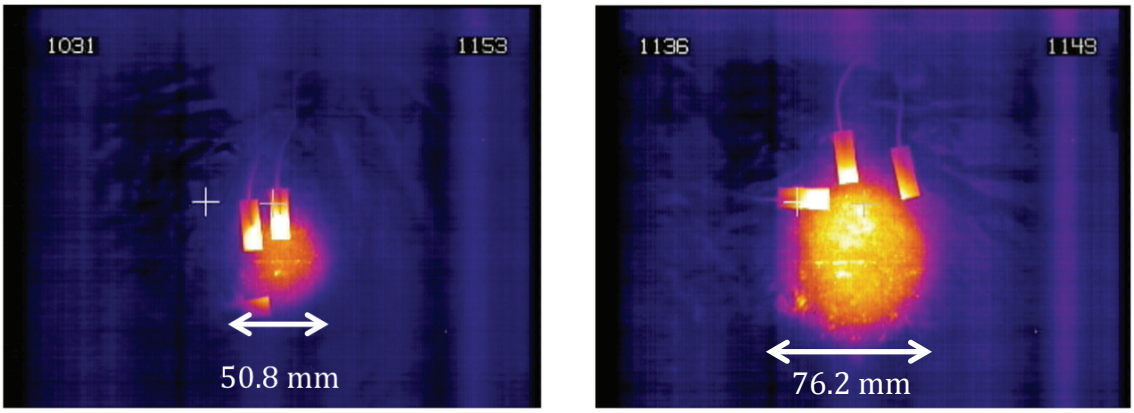

Figure 3.7: IR thermographic images of the 2*L* = 50.8 mm (*left*) and 76.2 mm (*right*) circular heaters with external forced convection.

The results of the temperature profiles that were measured for the 2*L* = 50.8 mm circular heaters at 0.11 and 0.19 W cm^{-2} as well as the model predictions obtained by the method of least squares, still using the separate values of h_h and h_f, are shown in Fig.3.8.

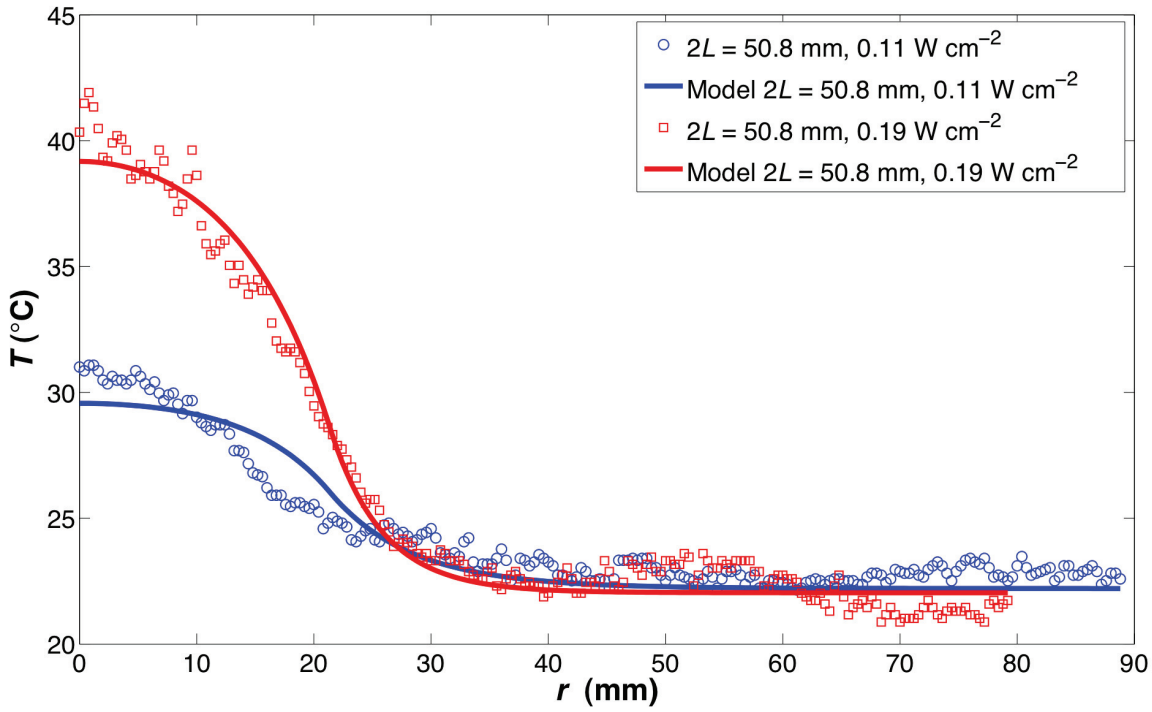

Figure 3.8: Experimental validation of the two-region fin model in cylindrical coordinates for $2L$ = 50.8 mm heater using two adjustable heat transfer coefficients to achieve best fit in conditions of forced convection. Heaters were operated at 0.11 and 0.19 W cm^{-2}, as indicated.

Table 3.2 shows the values of h_h and h_f in for the two-region fin model in Fig.3.8 determined by least-squares in Matlab. Their values are much greater than they were for natural convection in Table 3.1 and still in the correct order of magnitude for external forced convection (impinging flow) with air at ambient conditions. Note, however, that the values listed for the heater operated at 0.19 W cm^{-2} in Table 3.2 appear counter intuitive, since h_f is larger than h_h, but they are nonetheless in the correct order of magnitude overall. This apparent error in the determination of h_f and h_h for the heater operated at 0.19 W cm^{-2} was likely caused by a minor overestimation of the heated region boundary position, $r = L$ input to the model. This effect is seen in Fig.3.8 from the slight over-prediction of the two-region fin model temperatures in the heated region approaching $r = L$ and under-predictions in the fin region just past $r = L$. Another reason for the discrepancy could be the fact that the temperature profile for the heater operated at 0.19 W cm^{-2} in Fig.3.8 was prone to greater measurement uncertainty (details to follow) than for the heater profile at 0.11 W cm^{-2}.

Table 3.2: Two-region fin model external forced convection (impinging flow) heat transfer coefficients determined by least-squares two-parameter optimization in Matlab for the model profiles in Fig.3.8.

P (W cm^{-2})	h_h (W m^{-2} K^{-1})	h_f (W m^{-2} K^{-1})
0.11	138	69.8
0.19	96.3	187

The circular heaters were all placed in the center of the sample laminate film mounted on polystyrene foam for the experiments recorded in Fig.3.8, so flow characteristics arising from edges next to the heated areas did not interfere with their thermographic measurements. Just as for the rectangular heater measured under external forced convection, described in section 3.3.2, forced convection resulted in uniformly smooth temperature profiles. However, the use of circular heaters increased the magnitude of slope of the temperature profiles in the heated region compared to those from rectangular heaters – resembling the shape of domes rather than plateaux. Clearly, the radially increasing Al foil cross-section has a measurable impact on the fin region heat transfer, affecting the heated region acutely.

The quality of the fit in Fig.3.8 was noticeably better for the heater operated at 0.19 W cm^{-2} since the higher temperatures gave increased resolution of the temperature profile over the measurement uncertainty, making the slope easier to fit with the model. Both the heater powered at 0.11 and 0.19 W cm^{-2} had model error propagations that were bound by their measurement uncertainties. Measurement uncertainties were between 1.4 and 2.9˚C (entire domain, increasing from low to high temperatures) for the heater at 0.11 W cm^{-2}; uncertainties in the heated region were between 2.6 and 5.2˚C and between 1.9 and 2.6˚C in the fin region for the heater at 0.19 W cm^{-2}. Two-region fin model error propagations were between 0.50 and 0.62˚C and 0.50 and 1.2˚C for the heaters at 0.11 and 0.19 W cm^{-2}, respectively.

The temperature profiles measured from $2L$ = 76.2 mm circular heaters at 0.12, 0.14, and 0.19 W cm^{-2} are shown in Figure 3.9.

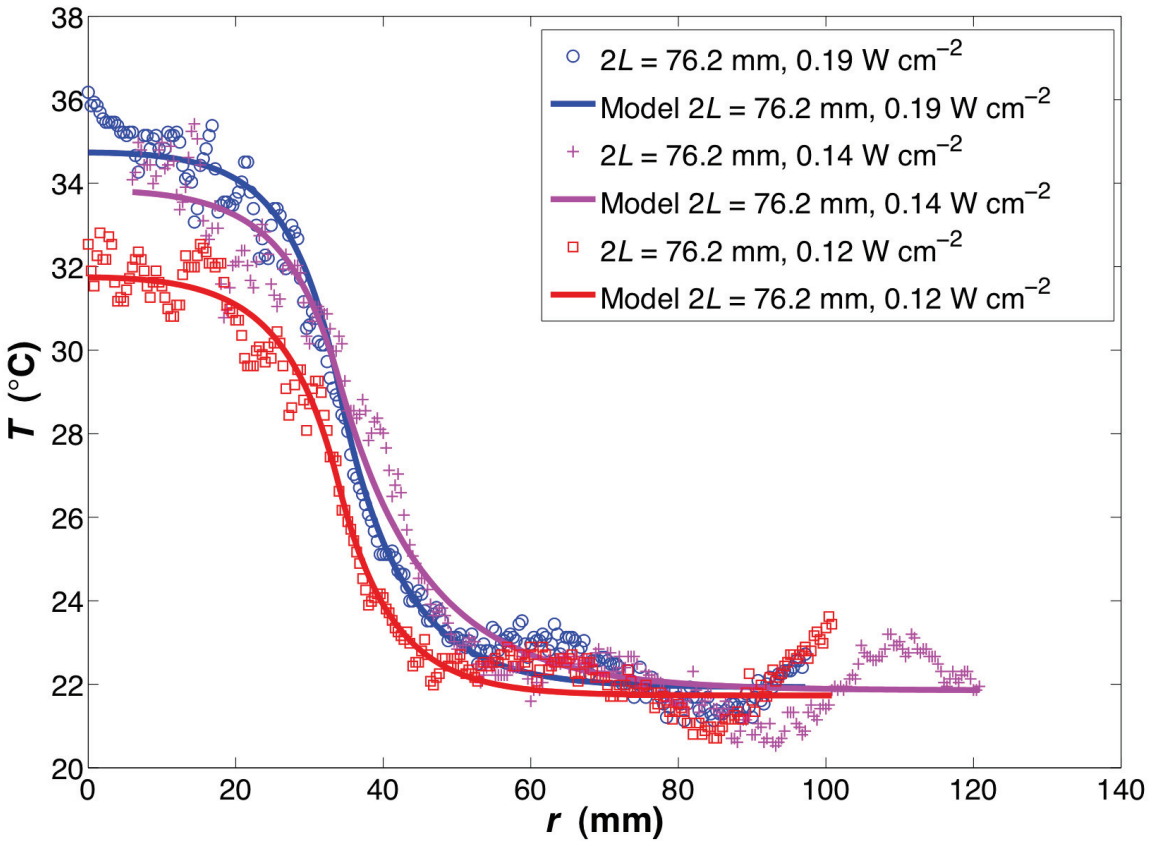

Figure 3.9: Experimental validation of the two-region fin model in cylindrical coordinates for $2L$ = 76.2 mm heater using two adjustable heat transfer coefficients to achieve best fit in conditions of forced convection. Heaters were operated at 0.12, 0.14 and 0.19 W cm^{-2}, as indicated.

Table 3.3 shows the values of h_h and h_f for the two-region fin model in Fig.3.9 determined by least-squares in Matlab. Once again, the values of h_h and h_f determined by least-squares are in the correct order of magnitude for external forced convection (impinging flow) with air at ambient conditions; in fact, they are very close to the values listed in Table 3.2 under similar conditions.

Table 3.3: Two-region fin model external forced convection (impinging flow) heat transfer coefficients determined by least-squares two-parameter optimization in Matlab for the model profiles in Fig.3.9.

P (W cm^{-2})	h_h (W m^{-2} K^{-1})	h_f (W m^{-2} K^{-1})
0.12	126	85.3
0.14	123	27.7
0.19	151	61.3

The high quality of the fit to each measured temperature profile in Fig.3.9 was uniformly achieved, adapting very well to the changing features with increasing heater power. The domes of the heated regions retained much of the curvature that was noted in Fig.3.8, but these were all flatter at the peaks, obviously an important feature of the larger circular heaters.

Note that the complete profile measured at 0.14 W cm^{-2} was difficult to ascertain, hence there is an absence of measurements between 0 and 5 mm in Fig.3.9. Nonetheless, this did not diminish the confidence to assess validation.

Measurement uncertainty in the heated region was between 1.6 and 2.1˚C, 2.4 and 3.1˚C, and 2.3 and 3.6˚C for the heater operated at 0.12, 0.14, and 0.19 W cm^{-2}, respectively, while the fin region uncertainty was between 1.0 and 1.6˚C, 1.3 and 2.4˚C, and 1.9 and 2.3˚C. Error propagation was between 0.50 and 0.63˚C, 0.50 and 0.62˚C, and 0.50 and 0.68˚C for the heater operated at 0.12, 0.14, and 0.19 W cm^{-2}, respectively, therefore proving that the model profiles were bound by the experimental profiles once again. The overall validation of the two-region fin model in cylindrical coordinates was observed as medium to high accuracy and equally applies to cases of constant temperature, as was stated in section 3.3.3.

3.5 UNCERTAINTY AND ERROR PROPAGATION

All physical measurements carry uncertainty, and so their ranges must be selected appropriately in order to draw meaningful observations from experiment. However, the use of measurements in model-based calculations requires even greater scrutiny since the relationship between the input measurement uncertainties and the computed error of the result can be coupled with increasing or even decreasing gain depending on other independent input variables and conditions.

The treatment of measurement uncertainty precedes that of model error propagation. The principal results of this project are those from the measured temperature profiles used for model validation, therefore the uncertainties were only those of temperature (IR-thermocouple) and position. The linear distance giving the position on the sample (x or r) was inferred from the number of pixels in the thermographic still-frames, corresponding to known physical dimensions. User judgment was a necessary part of the image analysis in Matlab, so these calibrations were repeated with every experiment in

order to calculate their 95% confidence intervals. Camera position was rarely altered, so these calibrations converged to an average of 0.4±0.05 mm per pixel.

The individual calibrations of thermocouple temperature and pixel intensity (recall Fig.3.4 in section 3.2.1) required more rigorous determination of uncertainty, since each calibration was used to obtain the individual temperature profiles used for validation. Each thermocouple calibration was performed over a small interval of pixels covering the thermocouple junction. Therefore, confidence intervals > 95% (2σ) could be calculated for the residuals between pixel data around each thermocouple and the lines of best fit used in the IR-thermocouple calibrations, and subsequently compounded with the uncertainty for Class 1, T-type thermocouples, being ±0.5˚C. These were plotted against the thermocouple temperatures and a least squares linear fit was applied (Fig.3.10). The least squares was added as a guide since the uncertainties could not otherwise be applied to the domain range of the validation temperature plots and the uncertainties typically followed an increasing trend from low temperatures to the highest ones (noted in section 3.2.1).

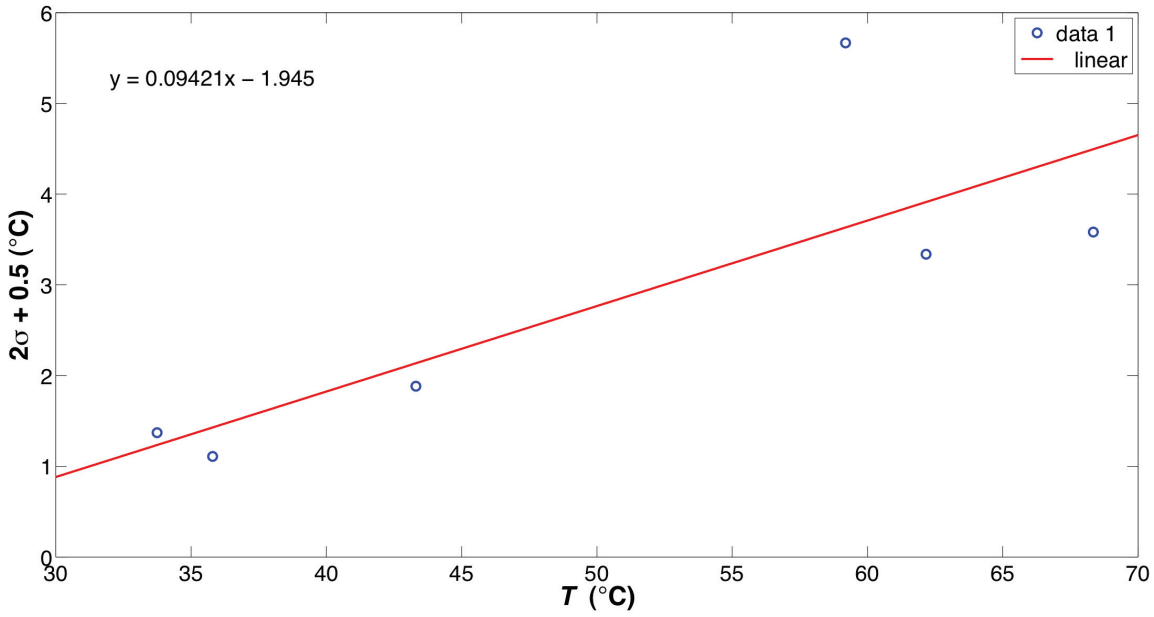

Figure 3.10: Uncertainty plot for the calibration data in Figure 3.4: L = 76.2 mm rectangular heater with natural convection, operated at 0.059 W cm^{-2}, gave an R^2 equal to 0.9274. 2σ represents the confidence interval of the residuals calculated between the IR-thermocouple calibration data and the least-squares line of best fit in Fig.3.4 with 0.5˚C added to it to allow for the T-type thermocouple uncertainty.

Model error propagation analysis, on the other hand, included thermocouple and position uncertainties and a few others, but relied on their relationship in the total differential of the dependent variable T. Regardless of the domain range or the coordinate system of the two-region fin model, the magnitude of the total differential of T is:

$$dT = \sqrt{\left(\frac{\partial T}{\partial V}dV\right)^2 + \left(\frac{\partial T}{\partial T_{\text{inf}}}dT_{\text{inf}}\right)^2 + \left(\frac{\partial T}{\partial t_1}dt_1\right)^2 + \left(\frac{\partial T}{\partial t_2}dt_2\right)^2 + \left(\frac{\partial T}{\partial x}dx\right)^2 + \left(\frac{\partial T}{\partial L}dL\right)^2}, \quad (3.1)$$

where V, T_{inf}, t_1, t_2, x (or r), and L are the linearly independent contributions of measurement uncertainty. These were each fixed and their values were: $dV = \pm 0.5$ V, $dT_{inf} = \pm 0.5$°C, $dt_1 = dt_2 = \pm 0.005$ mm, $dx = dr = \pm 0.05$ mm, and $dL = \pm 0.5$ mm. The list of all the partial differentials of T in Eq.(3.1) and of all the subsequent equation parameters in the two-region fin model is too lengthy for this section, so their detailed mathematical formulations can all be found in Appendix B: Error Propagation Analysis.

A first sample representation of this analysis is seen in Fig.3.11, in which the labels "dT" signify the products of the partial derivatives and their respective differentials in Eq.(3.1) with respect to the symbols written in subscript.

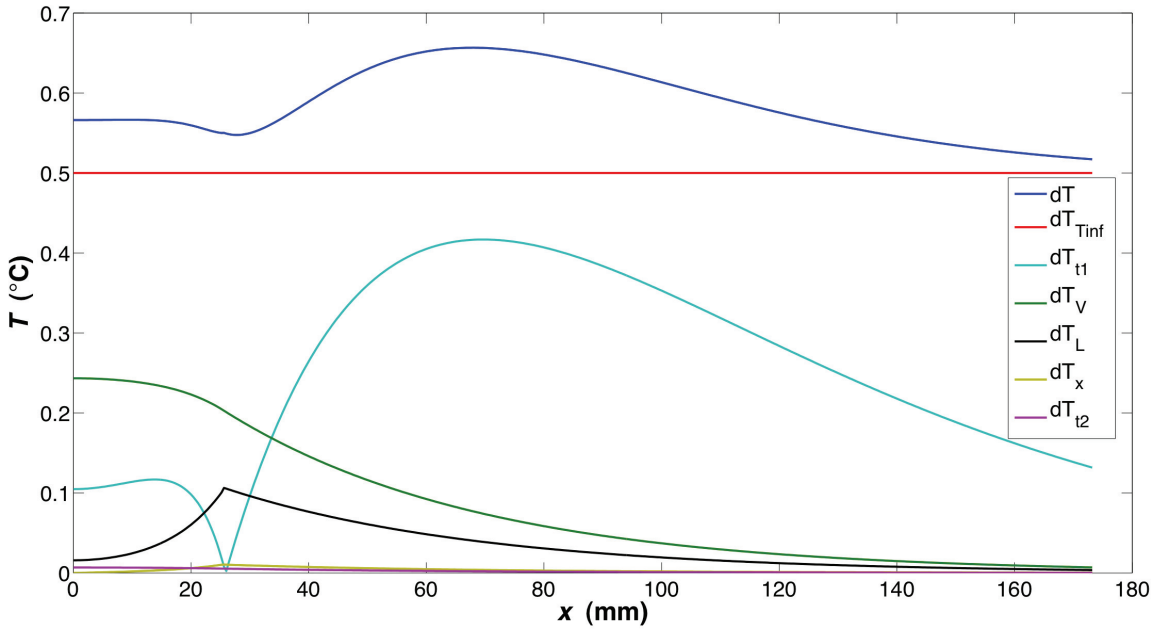

Figure 3.11: Error propagation analysis for T in the Cartesian two-region fin model. Result shown for L = 25.4 mm, 0.059 W cm^{-2}, and natural convection.

Since the error propagation is for the predicted two-region film model temperature, T, then it is understood that the thermocouple uncertainty for T_{inf} would dominate under

most circumstances (seen in Appendix B: Error Propagation Analysis). All four figures here, Fig.3.11 to 3.14, show this property, but additional components also increase in amplitude with the changing conditions of each experiment.

The other noteworthy contributions to the overall error of T are V (meaning q_o''), t_1, and L. The effect of V on T is confined to the heated region only, and remains always greatest at the domain origin. The greater the heating power, the greater the effect of V, but this can still be subdued with larger convection coefficients, h, or any combination of conditions causing reduced T in the heated region. Conditions in Fig.3.11 and 3.12 differ mainly by L and consequently the magnitude of the temperatures in the heated regions, causing the effect of V on T to increase; Fig.3.12 and 3.13 differ by the magnitude of convection coefficients, causing a reduction in the heated region temperature, thus decreasing the extent of the effect of V on T.

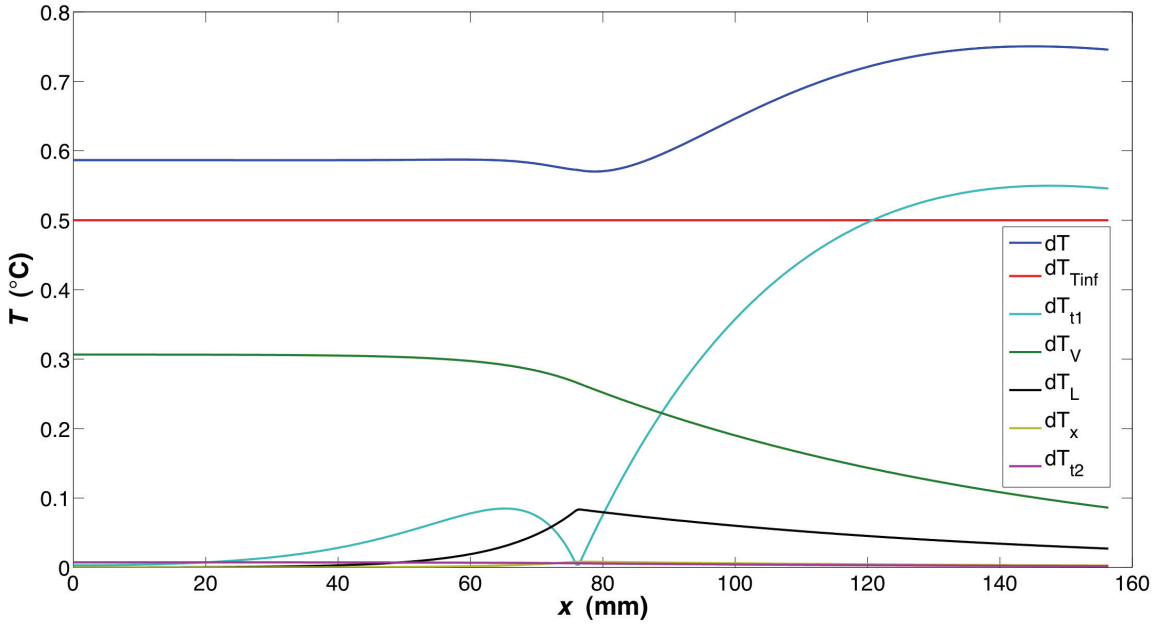

Figure 3.12: Error propagation analysis for T in the Cartesian two-region fin model. Result shown for L = 76.2 mm, 0.059 W cm^{-2}, and natural convection.

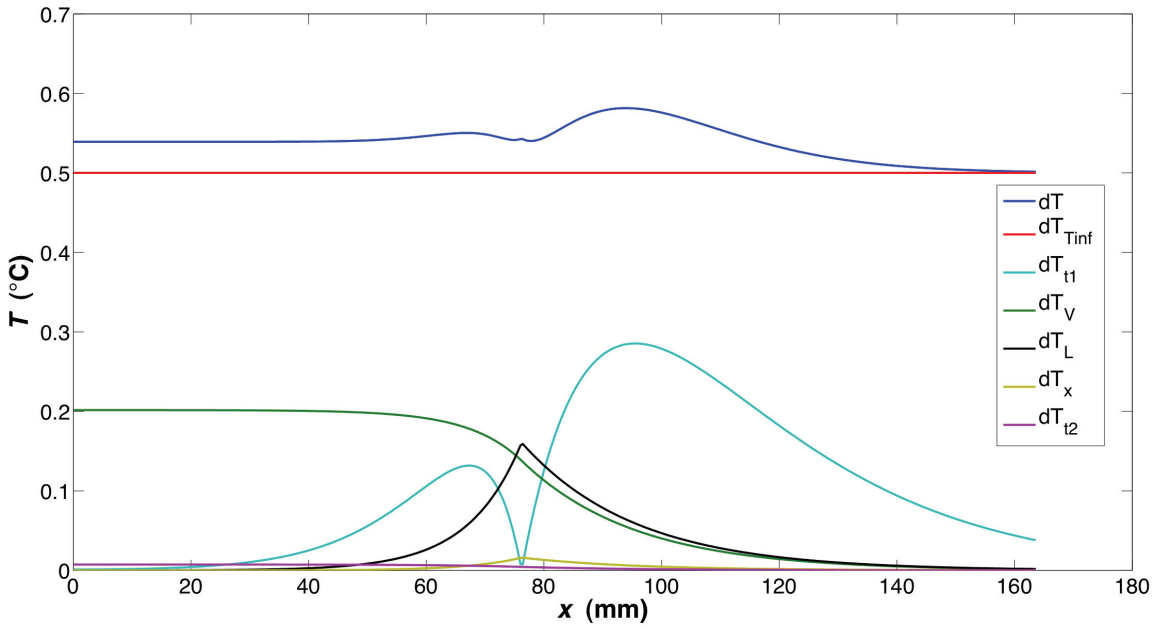

Figure 3.13: Error propagation analysis for *T* in the Cartesian two-region fin model. Result shown for *L* = 7.62 cm, 0.059 W cm^{-2}, and external forced convection.

The change from Cartesian to cylindrical coordinates also brings about a reduction in the effect of V on T in the heated region due to the increase in cross-section with radial expansion. Although they are not identical on the basis of L, Fig.3.13 and 3.14 emphasize the importance of radial expansion in cylindrical coordinates since the effect of V is reduced in Fig.3.14 despite the higher heat flux (also higher heated region temperature). The effect of high thermal conductivity metal core thickness (t_1) on T is also linked to this same cause. Greater effect of t_1 on T is observed in the heated region when there is greater tendency for axial conduction in the metallic core; Fig.3.11 to 3.13 (Cartesian) each show a subdued effect of t_1 in the heated region while Fig.3.14 (cylindrical) shows a pronounced effect. The same can be said about the effect of t_1 in the fin region, but it can also increase in magnitude due to poor convection (low h) since this causes the axial conductive heat flux to decay more slowly in the metallic core.

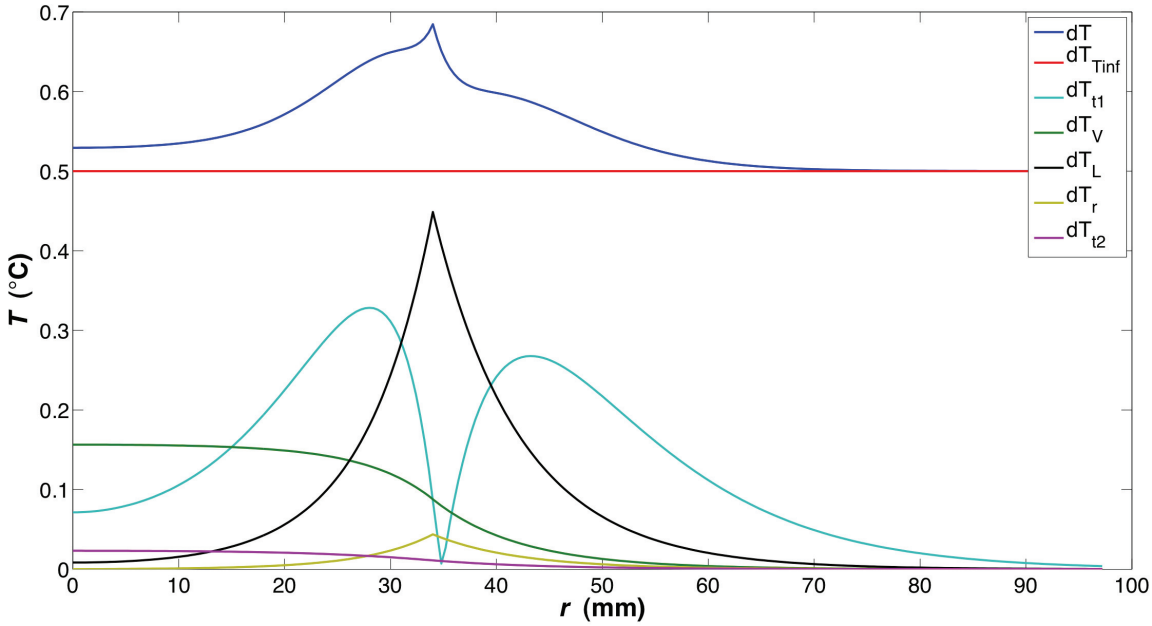

Figure 3.14: Error propagation analysis for *T* in the cylindrical two-region fin model. Result shown for 2*L* = 76.2 mm, 0.19 W cm^{-2}, and forced convection.

Lastly, the effect of L on T is most pronounced in all conditions of larger fin heat flux, hence conditions giving larger magnitude of slope to T at x or $r = L$. The effect is inherently greater in cylindrical coordinates (Fig.3.14) while there is not likely to be much difference between the various conditions in Cartesian coordinates (Fig.3.11 to 3.13) since the fin heat transfer rate, Q_{fin}', is limited by saturation (recall Eq.(2.54)).

3.6 TWO-REGION FIN HEAT TRANSPORT

Experiments conducted with thin laminate films composed of LDPE and Al that were procured from hydropulped Tetra Brik cartons and heated from behind by either thin rectangular heaters or thin circular heaters confirmed the anticipated behaviour from the two-region fin model in both the Cartesian and cylindrical coordinate systems. The equations all performed well to capture the temperature profiles as they were recorded by IR-thermography and the two-region fin model profiles were always bound by the experimental uncertainty for the measured temperature profiles in 1D. In fact, all validations were judged medium to high accuracy, which bodes well for using the two-region fin model in design. Medium accuracy validations were those that represented the features of the temperature profiles well, but lacked accuracy on the temperature predictions themselves, whereas high accuracy validations had both good representation of the features and good temperature prediction accuracy.

As was pointed out in section 2.3, circular heat sources benefit greatly from the capacity to dissipate heat in the fin region with increased effectiveness as the active surface area for heat transfer increases proportionally to r^2. Figures 3.8 and 3.9 represent experiments with circular heaters that were all operated at higher power than for the external forced convection experiment with a rectangular heat source in Fig.3.6, yet they were all at low temperatures, comparable to the rectangular heater experiment. It is clear that the greater ability to dissipate heat with radially increasing surface area was observed. Likewise, the slope of the temperature profile for the external forced convection experiment with the rectangular heater in Fig.3.6 is lower in magnitude than any of the slopes of the temperature profiles shown in the circular heater experiments in Fig.3.8 and 3.9. This again confirms the finding of section 2.3, that temperature uniformity in a laminate body can be more easily achieved using rectangular heat sources than with circular ones.

CHAPTER 4: LAMINATE FILM RECLAMATION

4.1 INTRODUCTION

In the prior chapters, it has been shown that there are heat transfer enhancing benefits in laminate films due to heat spreading; the extent of these benefits can be quantified using the two-region fin model. It is now equally important to assess potential material resources that could become useful for the fabrication of long-term heat storage PCM encapsulation.

Aseptic cartons (Fig.4.1) are the only immediately exploitable post-consumer resource of laminate films available in sufficient quantities in the global marketplace[4] that could be identified. The most viable markets based on collection rates are Germany (67% (Elopak, 2008)), Norway and Sweden (63% (Elopak, 2008)), Canada (45% in 2010, 38% in 2011 (Carton Council of Canada, 2011 and 2012)), Austria (36% (Elopak, 2008)), Brazil (23% in 2005 (Pedroso and Bastos, 2006)), and China (13% (Tetra Pak, 2011)), while Tetra Pak alone uses more than 0.75 Mt/y of laminate film in its packages (Tetra Pak, 2011). Since it is estimated that 20% of all cartons were recycled worldwide in 2010 (Tetra Pak, 2011), there must be more than 0.2 Mt of available laminate film from carton recycling annually.

[4] Aseptic cartons are produced worldwide primarily by Tetra Pak, Elopak, and SIG Combibloc.

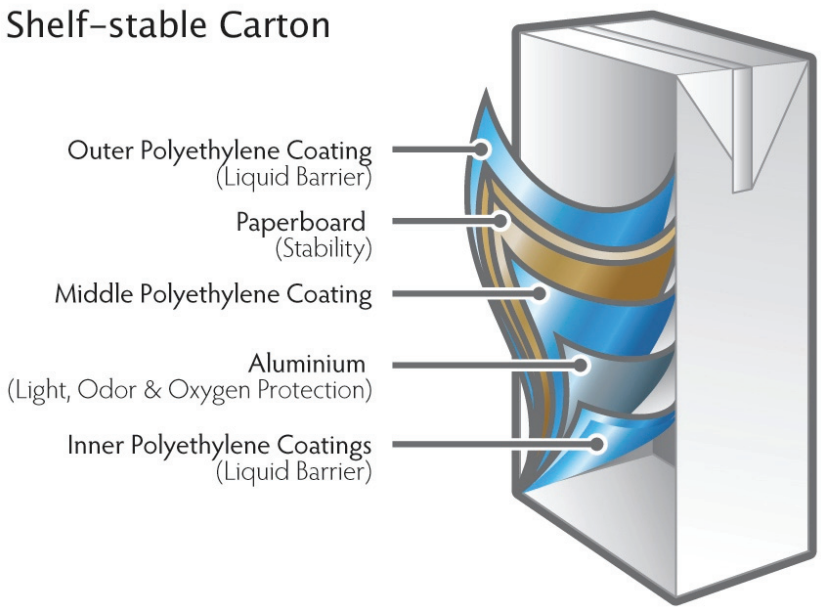

Figure 4.1: Aseptic carton diagram approved for educational distribution by the Carton Council of Canada (explicit consent for reproduction is given on the website of the Carton Council of Canada (2012)).

The effort involved in carton collection and sorting is the foremost reason to consider their laminate sheets as a viable waste resource. They must already be handled separately from other papers and plastics since the primary material component, liquid paperboard (~74%wt in Canada (Carton Council of Canada, 2012)), must be pulped separately in order to maintain the production rates and quality of the other post-consumer pulp feedstocks. Likewise, aseptic cartons cannot be recovered with conventional thermoplastic packaging due to the presence of the paperboard. However, suitable end-of-life options for the laminate film after pulping are not always obvious or even implemented, despite accounting for 55-58% of the embodied energy of the packaging (Table 4.1) with only ~26% of the packaging mass.

Table 4.1: Embodied energy calculations for aseptic cartons.

	Paperboard	Polyethylene	Al
Mass fraction[a]	0.74	0.22	0.04
Embodied energy of materials (MJ kg^{-1})[b]	24.2-32.0	77-85.0	200-240
Processing energy (MJ kg^{-1})[b]	0.475-0.525	2.4-2.7	2.4-2.9
Total component embodied energy (MJ kg^{-1})	18-24	17-19	8.1-9.7
Embodied energy fraction	0.42-0.45	0.37-0.40	0.18

[a] Carton Council of Canada (2012)

[b] Ashby (2009)

4.2 CARTON RECYCLING

The first stage in the separation of PE/Al laminate sheets from the paperboard in aseptic cartons is very simple if all cartons are without added wet-strength (e.g. paper towel has added wet-strength but toilet paper typically does not). The extraction of the paperboard is done by hydropulping, which is the method of extracting pulp by water immersion and simultaneous agitation (Fig.4.2). Hydropulping processes vary as either batch or continuous, and high, medium, or low consistency (relating to the pulp fibres (Abreu, 2000)). This process takes around 30 minutes, independent of the size of the process so long as all cartons are submerged and agitated, and usually does not require heated process water (the water can be ~50˚C from the mechanical process input alone (Abreu, 2000; Elopak, 2008)). In fact, hand-pulping 1 and 2L Tetra Brik aseptic cartons in Canada is not very difficult and can be accomplished in cold domestic water with light agitation for 35 minutes (Fig.4.3), probably due to especially low wet-strength, although other aseptic cartons might require some heated water.

Figure 4.2: Top-view of a high consistency batch hydropulper at the Klabin mill in Piracicaba, Brazil. The brown pulp seen here is the result of unbleached liquid paperboard made primarily from eucalyptus fibres, used in the production of Kraft liner at the Klabin mill. The walls of the vessel are baffled and the process accepts full bails of carton waste (see Fig.4.4), processing around 32,000 t of aseptic cartons per year (Pedroso and Bastos, 2006).

Figure 4.3: Hydropulping 1 and 2L Tetra Brik aseptic cartons by hand in a washbasin in domestic cold water from Halifax, NS. These cartons produced a white pulp.

The condition of the laminate can vary with the process, since the agitation method and power, residence time, feedstock preparation (see bails in Fig.4.4), and screening (Fig.4.5) are specific to the mill and marketplaces they serve.

Figure 4.4: Bailed aseptic cartons feedstock at the Klabin mill in Piracicaba, Brazil.

Figure 4.5: Detrashing screens downstream of the hydropulper used to recover process water in Piracicaba, Brazil.

Nonetheless, intact laminate sheets can be obtained from normal hydropulping operations (Fig.4.6), and their integrity could be improved by careful processing (e.g. hydropulping by hand, Fig.4.7).

Figure 4.6: Laminate films from hydropulping in Piracicaba, Brazil.

Figure 4.7: Laminate films from hydropulping by hand in Halifax, NS.

4.3 LAMINATE FILM

The utility of the laminate films recovered from aseptic cartons will depend on all their physical properties, not just their heat transfer benefits. Laminate films for long-term heat storage PCMs pouches must be leak-proof (e.g. by heat sealing with perhaps a secondary lamination to other recovered films) and be able to withstand the service conditions (transportation, storage, volume change of the PCM, external fluid flow for heat exchange) over an anticipated lifetime. For the latter, material strength characteristics must be taken into consideration.

Dimensionally speaking, the laminate films from the large-scale batch process at the mill in Piracicaba, Brazil and from hydropulping by hand in Halifax are identical: overall 0.1 mm thick (two LDPE layers of 40 μm and one Al foil of 20 μm) and at least 10x20 cm^2 when flattened and left unopened. Their thermal conductivities measured in a TC30 were comparable (section 3.2), so their compositional uniformity could be mostly assured.

The listed tensile strength of LDPE is between 0.4-16 MPa (Smith, 1998), while the tensile strength of pure casting Al alloy is 80 MPa (Smith, 1998). Assuming these properties hold in a parallel arrangement and using the film component thicknesses mentioned above, the anticipated tensile strength would be around 16 MPa; the Al foil would effectively impart the same maximum strength as the LDPE but with much less elongation (greater stiffness). Laminate films made with LDPE and Al would be made stronger under tension with increasing Al foil relative thickness. This would also increase the two-region fin heat transfer effectiveness, η, by decreasing the value of Ω_γ (recall Fig.2.8). The polyethylene, on the other hand, improves the film integrity under flexural strain.

Alternatively, films could be made with stronger polymers, e.g. high-density polyethylene (21-38 MPa (Smith, 1998)), polypropylene (27-40 MPa (Smith, 1998)), or polyester (170-230 MPa (DuPont Teijin Films, 2012)). Lane (1978, 1980) used 0.18 mm R-2 retort films, containing both polyethylene and polyester layers, with a tensile strength equal to 50 MPa for eutectic salt hydrate encapsulation (non-supercooling). Using the same approximation for the tensile strength as above, Lane's R-

2 retort film would have an anticipated tensile strength of 40 MPa. Such a method would therefore appear representative of a sample laminate film.

Lane (1978) also commented on the advantage of LDPE layers for the formation of strong lap seams, rather than weak pouch seams, despite the lower barrier qualities (diffusion of vapour/gases and liquids) and lower tensile strength reported just above. Promising waste resources of this kind that could be exploited for long-term PCM heat storage encapsulation, if separate collection was implemented, are laminate pouches for automotive polymer Li-ion batteries and laminate dry pet food bags. These are all designed to be more rugged than aseptic carton laminate films and typically come in large sizes.

4.4 RECYCLING ECOSYSTEM

Ultimately, the viability of a resource recovery effort relies on the economic rate of return that can be reasonably achieved. In Brazil, Klabin plant engineers confirmed that the price of the recycled pulp is insufficient to produce a reasonable profit from recycling aseptic cartons, and that establishing commercial partnerships for the sale of the laminate film is essential to the profitability of the industry. The sale of laminate films to their partners (mainly EET, a subsidiary of TSL Ambiental Brazil) to produce agglomerated pellets of the polyethylene and Al for injection moulding (mainly office wares, Fig.4.8), for moulded roof shingles (replacement for ceramic roof shingles), or for the separation/decomposition of the raw materials under inert atmosphere at 600˚C producing Al flakes and paraffin oil, allowed Klabin to remain in the business of pulping aseptic cartons. In the report on the plasma recovery (12,000˚C non-oxidizing plasma) of Al and paraffin (thermally decomposed polyethylene) by Pedroso and Bastos (2006), paper recovery would lose US$38/t of bailed cartons, but would expect to gain US$225/t of bailed cartons from the sale of Al ingots and paraffin, resulting in a net gain of US$187/t. Even so, the plasma process proved too costly after all, so EET (the plant operator, part of TSL Ambiental) opted for a lower-temperature process to produce only Al flakes at 600˚C rather than ingots, but also allowing for the agglomeration of the laminate films to sell for pelletization and for making roof shingles. The sale of laminates to EET makes the paper recovery nearly cost neutral for Klabin, while the end-producers of the plastic products made from carton regranulate (agglomerated and pelletized polyethylene and Al

from cartons) gain around US$200/t from the sale of roof shingles. Dunai (2009) also confirms that niche market sales of the recovered carton materials must be identified to generate profit for mills in Indonesia.

Figure 4.8: Promotional office wares provided by Tetra Pak Brazil. The plastic components are all produced from laminate film regranulate recovered by Klabin and EET.

Further evidence of the direct relationship between the ability for an aseptic carton recycling ecosystem to flourish and the necessary profitability driven from laminate film sales, is that both Canadian paper mills pulping cartons – Norampac in Burnaby, BC (Vancouver Observer, 2011) and Atlantic Packaging in Scarborough, ON – ceased their operations by the end of 2011. A phone call to Atlantic Packaging revealed that the company opted instead to sell their cartons from municipal curbside collections in Canada to markets in South Korea and Japan.

An even more direct benefit would be gained from exploiting the other potential laminate waste resources that do not yet have separate collection (e.g. automotive polymer Li-ion batteries and dry pet food bags). Uses for the laminates would be the sole revenue in the waste recovery ecosystem, especially where none already exists, and there would be little to no pre-processing cost as there is for hydropulping aseptic cartons.

4.5 RECLAIMED LAMINATES FOR LONG-TERM PCM HEAT STORAGE ENCAPSULATION

The successful use of reclaimed laminates for long-term PCM heat storage encapsulation depends strongly on the relationship between waste availability (separate collection and high collection rates), material characteristics (thickness and composition of layers and size of original packaging), post-consumer thermal properties (two-region fin behaviour) and mechanical properties (tensile strength and overall integrity) as well as cleanliness, ease of forming new sealed packages, and overall recycling economics. Of those laminate waste resources readily available and in sufficient quantities, laminate films from post-consumer aseptic cartons are promising materials and have demonstrated a very strong relationship for the recycling economics and the number of valuable uses for the laminate, since the paper recovery from hydropulping is rarely profitable (except where virgin pulp is scarce, e.g. Japan and South Korea).

Gentle hydropulping (similar to hydropulping by hand) produces good quality laminate films from aseptic cartons, but other good quality films can be obtained from current hydropulping operations in large paper mills. Other promising laminate waste resources do not require hydropulping as a pre-processing step, are more rugged than aseptic carton laminate films, and come in large sizes. However, these materials lack the collection infrastructure and cultural effort to do so. It is clear that a profitable end-use must first be identified, of which long-term PCM heat storage encapsulation could be a viable option in some markets (e.g. Canada).

Improved long-term heat storage technologies could finally help displace much of the Canadian household consumption of hydrocarbon fuels for space heating and water heating (71.0% of all household energy consumption (NRCAN, 2012)), especially since a long-standing barrier to heat storage deployment has been the persistent need to keep a secondary heating system, since conventional short-term solar hot water heating systems cannot reliably provide greater than a 50% solar fraction (Bédard and Leduc, 2011; Pinel et al., 2011). Long-term heat storage systems using modular supercooled salt hydrate PCM heat storage units that are shipped to customers could conceivably attain the coveted 100% solar fraction and finally present heat storage from renewable energy as a viable option to Canadians as well as others in northern climates.

CHAPTER 5: CONCLUSIONS AND FUTURE WORK

5.1 CONCLUSIONS

A model is proposed to improve the accurate predictions of heat transfer and temperature profiles from heat spreading, due to non-uniform heating, in multilayered composite bodies. Representative examples of multilayered composites are a laminate film of stacked PE/Al/PE and a multi-ply cookpot. The model, called the two-region fin model, provides accurate solutions in both Cartesian and cylindrical coordinates for the representation of either a phase change material (PCM, such as a supercooled salt hydrate) or an electric heat source applied to the surface of a laminate body in 2D. Non-dimensional equations are also presented in both Cartesian and cylindrical coordinates, and all of the equations are explicit, with no unspecified variables or functions, so their use in calculations is straightforward.

The method exploits the fact that the heat spreading behaviour in the high conductivity metal core dominates the conduction heat transfer observed in the system, reducing complexity from 2D to 1D heat conduction in the metal core with resistive dissipation through the remaining thermally resistive layers. This aspect is unique to the two-region fin model amongst all other multilayer composite heat conduction models in the literature, due to the fact that the model solution is split over two neighbouring domains: the heated region and the fin region. The equations were solved for steady-state heat transfer; however, provisions are provided to use the two-region fin model in pseudo steady-state analysis. Both the reduction from 2D to 1D heat conduction and the provisions offered for pseudo steady-state analysis are validated using a finite element model of a 2D laminate film solved in both Cartesian and cylindrical coordinates. These included steady-state and transient cases (i.e., heated boundary growth), the use of either constant temperature or constant heat flux boundary conditions for heat input to the system, and a forced convection boundary condition on the opposite surface for cooling. The validation resulted in very good agreement, therefore achieving high accuracy validation for the 1D approach and the provision for pseudo steady-state analysis.

Experimental validation was also carried out using thin rectangular and circular electric heating elements and laminate films made of LDPE and Al obtained from hydropulping 1 and 2 L Tetra Brik aseptic cartons. Surface temperature measurements by

IR-thermography were used to fit two-region fin model temperature profiles using a two-parameter least-squares approach in Matlab. Validation for the rectangular heaters was performed with both natural and forced external convections, while validation for the circular heaters were done with forced external convection only, because radial uniformity could not be adequately ensured with natural convection. Each of these exercises resulted in medium to high accuracy validation for the prediction of exact temperature profiles in the laminate. The validation accuracies were also extended to cases in which constant temperature heat sources are used, i.e. supercooled salt hydrate PCMs, since the temperature profiles are actually simpler to predict in those cases.

Two-region fin model analyses using either temperature profile plots and/or heat transfer effectiveness, η, domain maps give designers the ability to assess a material's performance either for the goal of improved temperature uniformity (temperature profile plots) or improved heat transfer rates (η domain maps). These methods of analysis were presented. For the goal of improving temperature uniformity using electric heating elements, rectangular heat sources give the best performance, while circular heat sources perform best to increase the rate of heat transfer from supercooled salt hydrate PCMs. Rates of heat transfer for circular PCM heat sources can be improved by 5700 to 42% for heat sources in the range $1\text{ mm} \leq L \leq 50\text{ mm}$, respectively, and for systems where $h = 50\text{ W m}^{-2}\text{ K}^{-1}$ and $k_1 = 260\text{ W m}^{-1}\text{ K}^{-1}$.

Potential laminate waste resources that could be used for making supercooled salt hydrate long-term heat storage pouches for space and/or domestic hot water heating with improved heat discharge capabilities were identified. The most accessible resource to date is from aseptic carton recycling. These are already collected separately from other waste materials in many countries and regions throughout the world, and the laminate films remaining after hydropulping are often unused, even incinerated or land-filled. The case of aseptic carton recycling in Brazil, by partners Klabin and EET in Piracicaba, SP and Tetra Pak Brazil, uncovered the economic benefit that could be gained from identifying value-added end-uses for the waste laminates, making the profitability of the recycling enterprise much greater than with hydropulping alone. Canadian hydropulping mills have ceased their operations due to the lack of profitable end-uses for the recovered paper alone, so valuable end-uses for the laminate would be needed to return aseptic

carton recycling operations to Canada. Suitable end-uses are essential, which is why this research proposes to use the laminate waste materials, provided that they are of good quality, as heat storage pouches for low-temperature domestic heat storage. This has been an increasingly important sector in Canada, with the average energy use for space heating and domestic hot water equal to 71.0% of all Canadian household energy consumption during the period of 1990-2009 (NRCAN, 2012). It is the hope that other waste resources that could be of even higher quality than aseptic cartons might also be used to make long-term heat storage pouches for supercooled salt hydrate PCMs. Of these, automotive polymer Li-ion battery pouches and dry pet food bags have been identified.

5.2 RECOMMENDATIONS AND FUTURE WORK

It is recommended to evaluate the fabrication of heat storage pouches for supercooled salt hydrate PCMs from the reclaimed laminate waste materials to aim for good, reliable operation over many repeated charge/discharge cycles. The present work makes no assurances as to the mechanical durability of laminate pouches under repeated cycling.

The comparison of heat transfer rate measurements from nucleated salt hydrates in laminate pouches and in simple thermoplastic pouches is also recommended to further test the heat transfer improvements that can be obtained from the heat-spreading behaviour in laminate pouches. These measurements should also be compared to the upper and lower bound estimates (cylindrical and Cartesian, respectively) of the heat transfer rate from the two-region fin model. Numerical simulations should then be developed and validated to increase the pace of laminate, long-term, heat storage pouch evaluation under various scenarios of forced convection, degrees of supercooling, and nucleation trigger placement and number thereof in the individual pouches.

Future work should continue in the areas of control scheme development to operate supercooled salt hydrate heat stores effectively, to reliably implement nucleation triggering mechanisms into heat storage pouches, and to develop modular heat storage system development suitable for a production-distribution paradigm.

REFERENCES

ABHAT A. (1983) "Low temperature latent heat thermal energy storage: heat storage materials," Solar Energy, Vol. 30, pp.313-332.

ABREU M. (2000) "Recycling the fibres on Tetra Pak cartons," Tetra Pak Canada Inc.

AGYENIM F., HEWITT N., EAMES P., and MERVYN S. (2010) "A review of materials, heat transfer and phase change problem formulation for latent heat thermal energy storage systems (LHTESS)," Renewable and Sustainable Energy Reviews, Vol. 14, pp.615-628.

ARAKI N., FUTAMURA M., MAKINO A., and SHIBATA H. (1995) "Measurements of thermophysical properties of sodium acetate hydrate," International Journal of Thermophysics, Vol. 16, pp. 1455-1466.

ASHBY M.F. (2009) "Materials and the environment," Elsevier: Oxford, UK, 385 pages.

ANTHONY A.E.M., BARRETT P.F., and DUNNING P.K. (1990) "Verification of a mechanism for nucleating crystallization of supercooled liquids," Materials Chemistry and Physics, Vol. 25, pp.199-205.

AVELLA M., AVOLIO R., BONADIES I., CARFAGNA C., ERRICO M.E., and GENTILE G. (2009) "Recycled multilayer cartons as cellulose source in HDPE-based composites: compatibilization and structure-properties relationships," Journal of Applied Polymer Science, Vol. 114, pp.2978-2985.

BÉDARD N. and LEDUC M.A. (2011) "Bilan d'opération de systèmes solaires thermiques au LTE," Infobec (ASHRAE Quebec Chapter), Vol. 35, pp.7-12.

BERNARDES A.M., ESPINOSA D.C.R., and TENÓRIO J.A.S. (2004) "Recycling of batteries: a review of current processes and technologies," Journal of Power Sources, Vol. 130, pp.291-298.

CARTON COUNCIL OF CANADA, accessed November 30, 2011 and May 1st, 2012. http://www.recyclecartons.ca/recycling.html

CASTILLO F.A.S., LABERTY-ROBERT C., and PORTAL J. (2002) "Advances in the recovering of spent lithium battery compounds," Journal of Power Sources, Vol. 112, pp.247-254.

DE MONTE F. (2002) "An analytic approach to the unsteady heat conduction processes in one-dimensional composite media," International Journal of Heat Mass Transfer, Vol. 45, pp.1333-1343.

DESGROSSEILLIERS L., MURRAY R., SAFATLI A., MARIN G., STEWART J., OSBOURNE N., WHITE M.A., and GROULX D. (2011) "Phase change material selection in the design of a latent heat energy storage system coupled with a domestic hot water solar thermal system," Proceedings of the American Society of Heating, Refrigerating and Air-Conditioning Engineers (ASHRAE) Conference, Montreal, QC, 8 pages.

DRAKE LANDING SOLAR COMMUNITY, accessed on July 11th, 2012. http://www.dlsc.ca/

DUNAIS M-A. (2009) "Cost benefit analysis of aseptic carton recycling in Bandung, Indonesia," Nicholas School of the Environment, Durham, NC, Duke University, MEM, 31 pages.

DUPONT TEIJIN FILMS, Mylar Datasheet, accessed July 10th, 2012. http://www.dupontteijinfilms.com/filmenterprise/Datasheet.asp?ID=302&Version=US

ELOPAK (2008) "Collection of beverage cartons," Oslo, Norway, 22 pages.

ELOPAK (2009) "Elopak environmental report," Oslo, Norway, 28 pages.

ESPINOSA D.C.R., BERNARDES A.M., and TENÓRIO J.A.S. (2004) "An overview on the current processes for the recycling of batteries," Journal of Power Sources, Vol. 135, pp.311-319.

FARID M.M., KUDHAIR A.M., RAZACK S.A.K., and AL-HALLAJ S. (2004). "A review on phase change energy storage: materials and applications," Energy Conversion and Management, Vol. 45, pp.1597-1615.

FURBO S. and SCHULTZ J.M. (2007) "State of development of the work with seasonal PCM heat storage at the Department of Civil Engineering, Technical University of Denmark (DTU)," in "A Report of IEA Solar Heating and Cooling programme - Task 32: Advanced storage concepts for solar and low energy buildings," STREICHER W. (Ed.), International Energy Agency.

GARG H.P., MULLICK S.C., and BHARGAVA A.K. (1985) "Solar thermal energy storage," D. Reidel Publishing Company, 642 pages.

GRANT T., JAMES K.L., LUNDIE S., and SONNEVELD K. (2001) "Stage 2 report for life cycle assessment for paper and packaging waste management scenarios in Victoria," Eco Recycle Victoria, 140 pages.

GROLL W.A. (2001) "Method for making a copper core five-ply composite for cookware," US Patent 6267830B1.

GROLL W.A. (2005) "Bonded metal components having uniform thermal conductivity characteristics and method of making same," US Patent 6926971B2.

HALIFAX REGIONAL MUNICIPALITY, Solar City Initiative, accessed July 11th, 2012. http://www.halifax.ca/solarcity/

HAJI-SHEIKH A. and BECK J.V. (2002) "Temperature solution in multi-dimensional multi-layer bodies," International Journal of Heat and Mass Transfer, Vol. 45, pp.1865-1877.

HAJI-SHEIKH A., BECK J.V., and AGONAFER D. (2003) "Steady-state heat conduction in multi-layer bodies," International Journal of Heat and Mass Transfer, Vol. 46, pp.2363-2379.

HIRANO S. and SAITOH T.S. (2002a) "Growth rate of crystallization of disodium hydrogenphosphate dodecahydrate," Journal of Thermophysics and Heat Transfer, Vol. 16, pp.135-140.

HIRANO S. and SAITOH T.S. (2002b) "Influence of operating temperature on efficiency of supercooled salt thermal energy storage," 37th Annual Intersociety Energy Conversion Engineering Conferences, pp.684-689.

HIRANO S. and SAITOH T.S. (2009) "Long-term performance of latent heat thermal energy storage using supercooling," Proceedings of ISES Solar World Congress 2007: Solar Energy and Human Settlement, pp.2741-2745.

ZHANG J-F., YAN D-H., and LI Z-H. (2009) "The recycling of the Tetra-Pak packages: research on the wet process separation conditions of aluminum and polythene in the Tetra-Pak packages," 3rd International Conference on Bioinformatics and Biomedical Engineering, 6 pages.

KARAKAS A., TUNC M., and CAMDALI Ü. (2010) "Thermal analysis of thin multi-layer metal films during femtosecond laser heating," Heat and Mass Transfer, Vol. 46, pp.1287-1293.

KENISARIN M. and MAHKAMOV K. (2007) "Solar energy storage using phase change materials," Renewable and Sustainable Energy Reviews, Vol. 11, pp.1913-1965.

KHUDHAIR A. and FARID M.M. (2004) "A review on energy conservation in building applications with thermal storage by latent heat using phase change materials," Energy Conversion and Management, Vol. 45, pp.263-275.

LANE G.A., KOTT A.C., WARNER G.L., HARTWICK P.B., and ROSSOW H.E. (1978) "Macro-encapsulation of heat storage phase-change materials for use in residential buildings: report ORO/5217-8," Dow Chemical Company, Midland, MI.

LANE G.A. (1980) "Low temperature heat storage with phase change materials," International Journal of Ambient Energy, Vol. 1, pp.155-168.

LANE G.A. (1983) "Solar heat storage: background and scientific principles," CRC Press, Vol. 1, 248 pages.

LANE G.A. (1985) “PCM science and technology: the essential connection,” ASHRAE Transactions, Vol. 91, pp.1897-1909.

LIU K-C. (2007) “Analysis of thermal behavior in multi-layer metal thin films based on hyperbolic two-step model,” International Journal of Heat and Mass Transfer, Vol. 50, pp.1397-1407.

LOPES C.M.A, GONÇALVES M.d.C., and FELISBERTI M.I. (2007) “Blends of poly(ethylene terephthalate) and low density polyethylene containing aluminium: A material obtained from packaging recycling,” Journal of Applied Polymer Science, Vol. 106, pp.2524-2535.

MARK J.E. (2009) “Polymer data handbook (2nd edition),” Oxford University Press.

MATHIS INSTRUMENTS LTD. (2002) “TC-30™ Manual: Windows 2000 Version 5.30.”

MATYSIAK S. and WOŹNIAK C. (1987) “On the modelling of heat conduction problem in laminated bodies,” Acta Mechanica, Vol. 65, pp.223-238.

MOURAD A.L., GARCIA E.E.C., VILELA G.B., and VON ZUBEN F. (2008) “Influence of recycling rate increase of aseptic carton for long-life milk on GWP reduction,” Resources, Conservation and Recycling, Vol. 52, pp.678-689.

MURRAY R., DESGROSSEILLIERS L., STEWART J., OSBOURNE N., MARIN G., SAFATLI A., GROULX D., and WHITE M.A. (2011) “Design of a latent heat energy storage system coupled with a domestic hot water solar thermal system,” World Renewable Energy Congress 2011, Linköping, Sweden, 8 pages.

NAQAVI I.Z., YILBAS B.S., and KHAN O. (2003) “Laser heating of multilayer assembly and stress levels: elasto-plastic consideration,” Heat and Mass Transfer, Vol. 40, pp.25-32.

NIST CHEMISTRY WEBBOOK, Ethene Homopolymer, accessed July 10th, 2012. http://webbook.nist.gov/cgi/cbook.cgi?ID=C9002884&Mask=2

NATURAL RESOURCES CANADA (NRCAN) (2012) “Energy use data handbook: 1990-2009,” Government of Canada, 169 pages.

OGOH W. (2010) “Numerical study of the effects of fins and thermal fluid velocities on the storage characteristics of a cylindrical latent heat energy storage system,” Department of Mechanical Engineering, Halifax, NS, Dalhousie University, MASc, 114 pages.

PINEL P., CRUICKSHANK C.A., BEAUSOLEIL-MORRISON I., and WILLS A. (2011) “A review of available methods for seasonal storage of solar thermal energy in residential applications,” Renewable and Sustainable Energy Reviews, Vol. 15, pp.3341-3359.

PEDROSO M.C. and BASTOS JR. A.F. (2006) “Recycling of aseptic carton packages in Brazil: a case study of sustainable supplychain,” Global Conference on Sustainable Product Development and Life Cycle Engineering, São Carlos, Brazil.

PERRY R. and GREEN D. (2008) “Perry’s chemical engineers’ handbook, eighth edition,” McGraw-Hill Professional, Access Engineering.

RA D-I. and HAN K-S. (2006) “Used lithium ion rechargeable battery recycling using Etoile-Rebatt technology,” Journal of Power Sources, Vol. 163, pp.284-288.

RODRIGUEZ M.E., NARROS G.A., and MOLLEDA J.A. (1995) “Wastes of multilayer containers as substrate in composting process,” Journal of the Air and Waste Management Association, Vol. 45, pp.156-160.

SANDNES B. (2003) “Exergy efficient production, storage and distribution of solar energy,” Department of Physics. Oslo, Norway, University of Oslo, PhD, 170 pages.

SANDNES B. (2008) “The physics and the chemistry of the heat pad,” American Journal of Physics, Vol. 76, pp.546-550.

SCOTIAN WINDFIELDS (2009) “Case study: 21 Plateau – Killam Properties,” Halifax, NS, 2 pages.

SIBBITT B., MCCLENAHAN D., DJEBBAR R., THORNTON J., WONG B., CARRIERE J., and KOKKO J. (2011) “Measured and simulated performance of a high solar fraction district heating system with seasonal storage,” ISES Solar World Congress 2011, Kassel, Germany, 12 pages.

SINGH S., JAIN P.K., and RIZWAN-UDDIN (2008) “Analytical solution to transient heat conduction in polar coordinates with multiple layers in radial direction,” International Journal of Thermal Sciences, Vol. 47, pp.261-273.

SMITH E.H. (1998) “Mechanical engineer's reference book,” 12th ed., Elsevier.

STATISTICS CANADA (2008) “Canadian demographics at a glance,” Government of Canada ,Catalogue no. 91-003-X, 54 pages.

STATISTICS CANADA (2009) “Electric power generation, transmission and distribution (2007),” Government of Canada, Catalogue no. 57-202-X, 42 pages.

STATISTICS CANADA (2010) “Households and the environment: energy use (2007),” Government of Canada, Catalogue no. 11-526-S, 39 pages.

STESSEL R.I. (1996) “Disposable product design and recycling,” Proceedings of the 17th Biennial Waste Processing Conference, ASME.

SUN Y. and WICHMAN I.S. (2004) “On transient heat conduction in a one-dimensional composite slab,” International Journal of Heat and Mass Transfer, Vol. 47, pp.1555-1559.

TETRA PAK (2011) “Mission possible: sustainability update 2011,” Lund, Sweden.

TETRA PAK, accessed November 29, 2011. http://campaign.tetrapak.com/su2011/environment/naturalresources/seeing-the-wood-for.html#.

VANCOUVER OBERSERVER (2011) “100 jobs lost as Burnaby mill closes,” accessed February 13th, 2012. http://www.vancouverobserver.com/money/business/2011/09/20/100-jobs-lost-burnaby-mill-closes

VON ZUBEN F., ORSATO R.J., and WASSENHOVE L. (2007) “Turning waste into wealth,” International Commerce Review, Vol. 7, pp.116-123.

WEI L.L. and OHSASA K. (2010) “Supercooling and solidification behaviour of phase change material,” ISIJ International, Vol.50, pp.1265-1269.

WETTERMARK G., CARLSSON B., and STYMNE H. (1979) “Storage of heat: a survey of efforts and possibilities,” Swedish Council for Building Research, Stockholm, Sweden, 163 pages.

WOOLF L.D. (1985) “Graphite composite cookware,” US Patent 4541411.

XU J., THOMAS H.R., FRANCIS R.W., LUM K.R., WANG J., and LIANG B. (2008) “A review of processes and technologies for the recycling of lithium-ion secondary batteries,” Journal of Power Sources, Vol. 177, pp. 512-527.

YANG Y.S. (2001) “Trigger for a portable heat pack,” US Patent 6283116B1.

ZALBA B., MARíN J.M., CABEZA L.F., and MEHLING H. (2003) “Review on thermal energy storage with phase change: materials, heat transfer analysis and applications,” Applied Thermal Engineering, Vol. 23, pp.251-283.

APPENDIX A: MEASUREMENT UNCERTAINTIES FROM IR-THERMOCOUPLE CALIBRATIONS (SUPPLEMENTAL FIGURES)

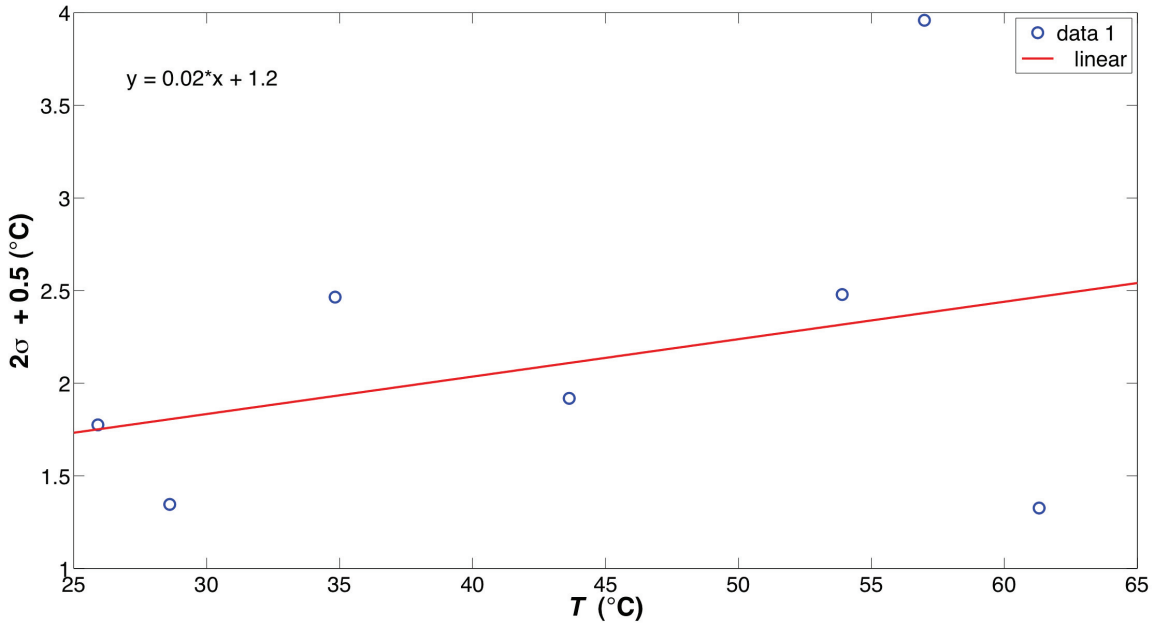

Figure A-1: Uncertainty plot for the calibration data in Figure 3.5: L = 25.4 mm rectangular heater with natural convection, operated at 0.059 W cm^{-2}, and gave an R^2 equal to 0.7821. 2σ represents the confidence interval of the calculated residuals from the IR-thermocouple calibration, also adding 0.5˚C for the T-type thermocouple uncertainty.

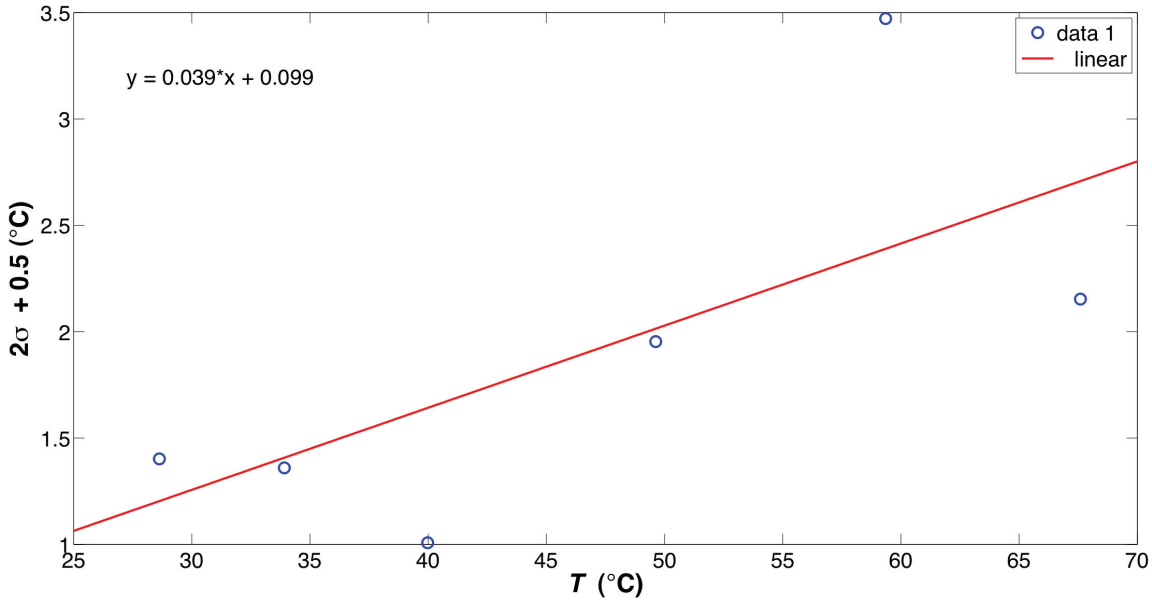

Figure A-2: Uncertainty plot for the calibration data in Figure 3.5: L = 50.8 mm rectangular heater with natural convection, operated at 0.059 W cm^{-2}, and gave an R^2 equal to 0.8728. 2σ represents the confidence interval of the calculated residuals from the IR-thermocouple calibration, also adding 0.5˚C for the T-type thermocouple uncertainty.

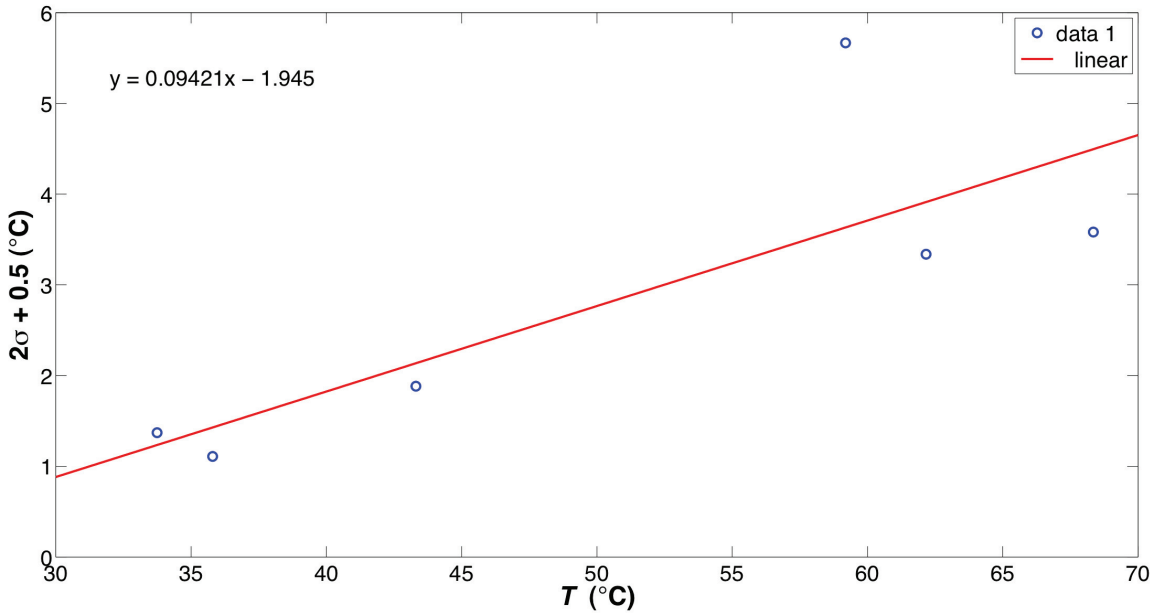

Figure A-3: Uncertainty plot for the calibration data in Figure 3.5: L = 76.2 mm rectangular heater with natural convection, operated at 0.059 W cm^{-2}, and gave an R^2 equal to 0.9274. 2σ represents the confidence interval of the calculated residuals from the IR-thermocouple calibration, also adding 0.5˚C for the T-type thermocouple uncertainty.

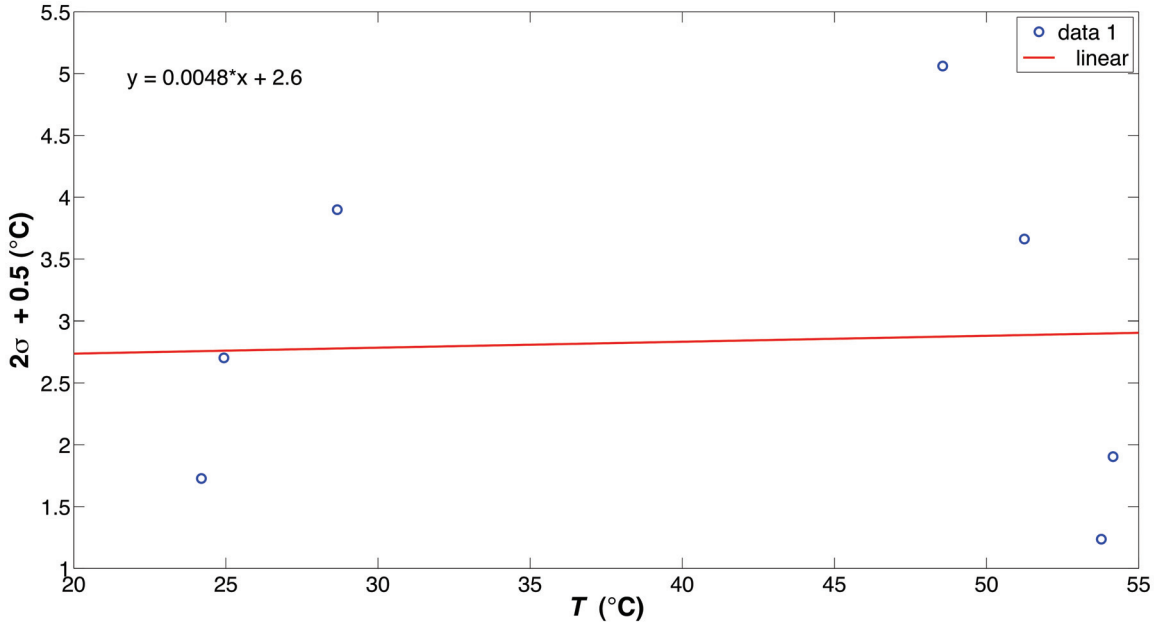

Figure A-4: Uncertainty plot for the calibration data in Figure 3.6: L = 76.2 mm rectangular heater with external forced convection, operated at 0.059 W cm^{-2}, and gave an R^2 equal to 0.8545. 2σ represents the confidence interval of the calculated residuals from the IR-thermocouple calibration, also adding 0.5˚C for the T-type thermocouple uncertainty.

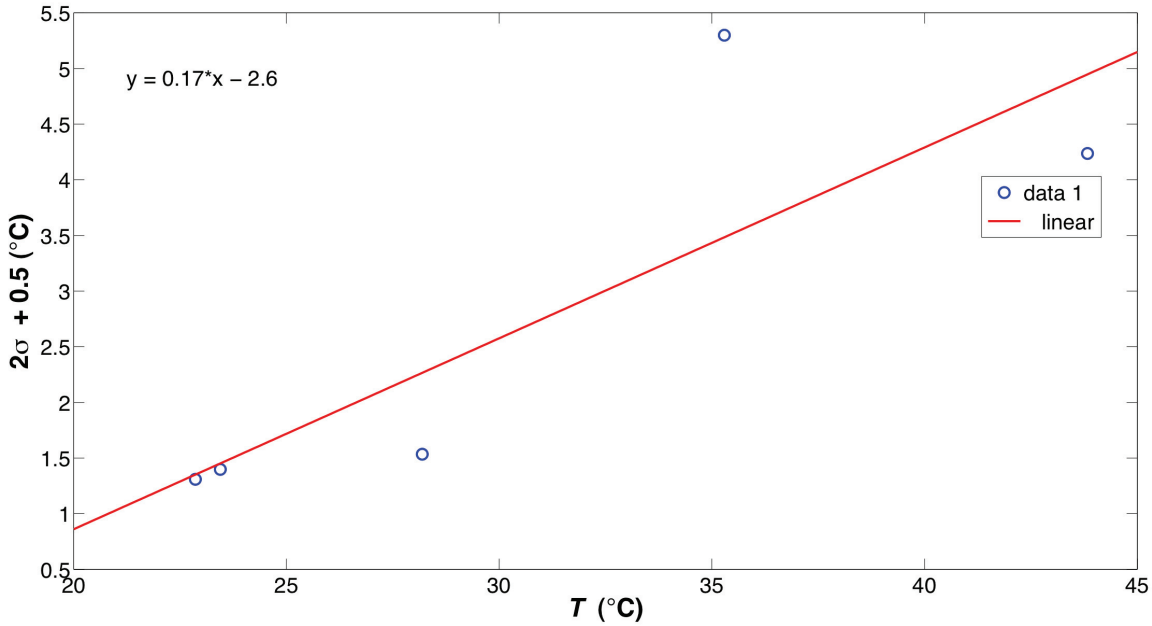

Figure A-5: Uncertainty plot for the calibration data in Figure 3.8: 2*L* = 50.8 mm circular heater with external forced convection, operated at 0.11 W cm^{-2}, and gave an R^2 equal to 0.9417. 2σ represents the confidence interval of the calculated residuals from the IR-thermocouple calibration, also adding 0.5°C for the T-type thermocouple uncertainty.

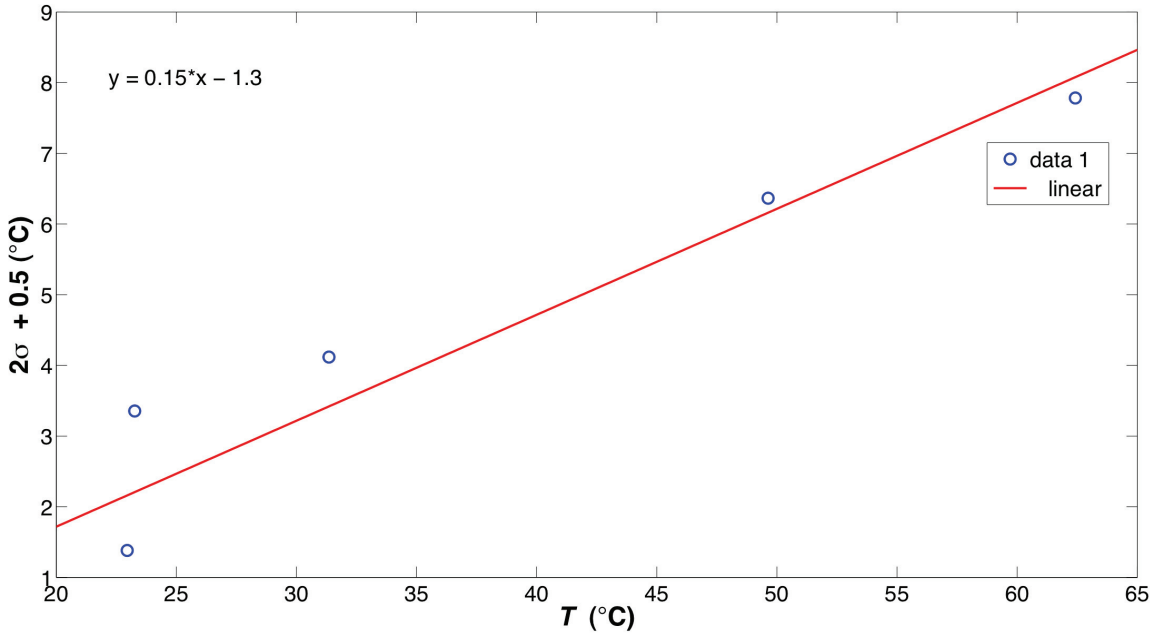

Figure A-6: Uncertainty plot for the calibration data in Figure 3.8: 2*L* = 50.8 mm circular heater with external forced convection, operated at 0.19 W cm^{-2}, and gave an R^2 equal to 0.9746. 2σ represents the confidence interval of the calculated residuals from the IR-thermocouple calibration, also adding 0.5°C for the T-type thermocouple uncertainty.

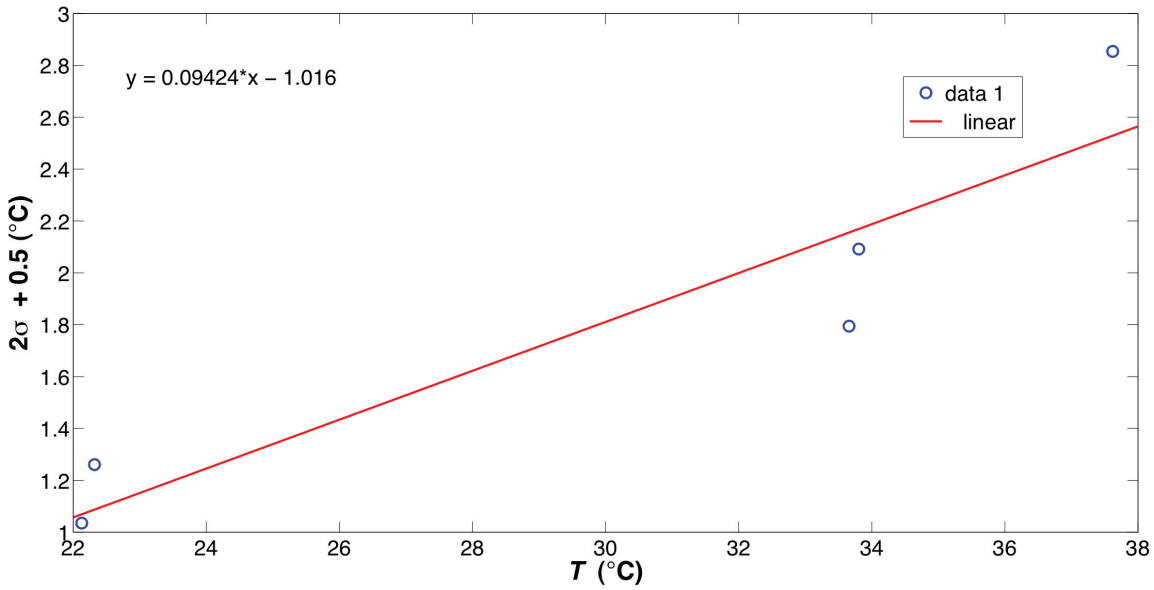

Figure A-7: Uncertainty plot for the calibration data in Figure 3.9: 2*L* = 76.2 mm circular heater with external forced convection, operated at 0.12 W cm^{-2}, and gave an R^2 equal to 0.8936. 2σ represents the confidence interval of the calculated residuals from the IR-thermocouple calibration, also adding 0.5°C for the T-type thermocouple uncertainty.

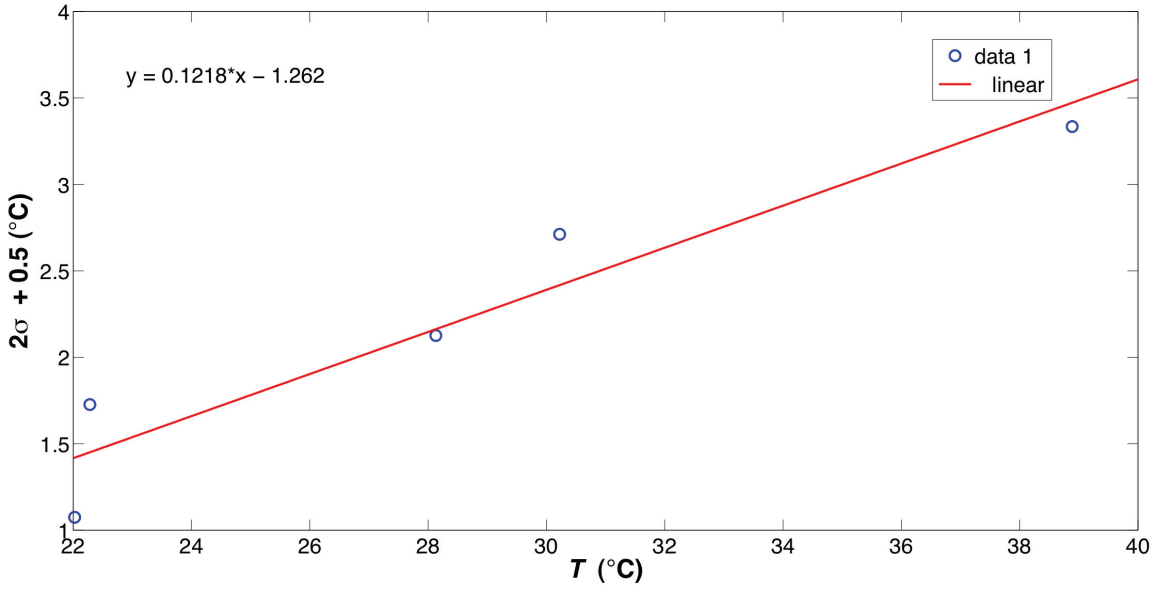

Figure A-8: Uncertainty plot for the calibration data in Figure 3.9: 2*L* = 76.2 mm circular heater with external forced convection, operated at 0.14 W cm^{-2}, and gave an R^2 equal to 0.9149. 2σ represents the confidence interval of the calculated residuals from the IR-thermocouple calibration, also adding 0.5°C for the T-type thermocouple uncertainty.

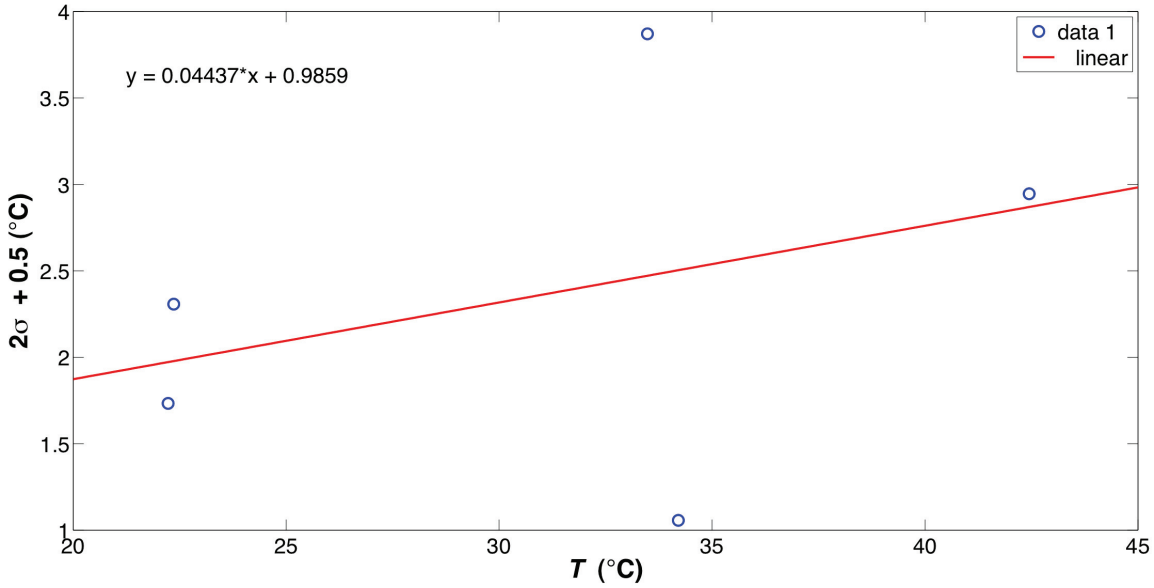

Figure A-9: Uncertainty plot for the calibration data in Figure 3.9: 2*L* = 76.2 mm circular heater with external forced convection, operated at 0.19 W cm^{-2}, and gave an R^2 equal to 0.7900. 2σ represents the confidence interval of the calculated residuals from the IR-thermocouple calibration, also adding 0.5°C for the T-type thermocouple uncertainty.

APPENDIX B: ERROR PROPAGATION ANALYSIS

Equations:

Cartesian Coordinates:

$$dT = \sqrt{\left(\frac{\partial T}{\partial V}dV\right)^2 + \left(\frac{\partial T}{\partial T_{\inf}}dT_{\inf}\right)^2 + \left(\frac{\partial T}{\partial t_1}dt_1\right)^2 + \left(\frac{\partial T}{\partial t_2}dt_2\right)^2 + \left(\frac{\partial T}{\partial x}dx\right)^2 + \left(\frac{\partial T}{\partial L}dL\right)^2}$$

Heated Region:

$$\frac{\partial T}{\partial V} = \frac{\partial T}{\partial T_o}\frac{\partial T_o}{\partial \beta}\frac{\partial \beta}{\partial V} + \frac{\partial T}{\partial \beta}\frac{\partial \beta}{\partial V}$$

$$\frac{\partial T}{\partial T_{\inf}} = \frac{\partial T}{\partial T_o}\left(\frac{\partial T_o}{\partial T_{\inf}} + \frac{\partial T_o}{\partial \beta}\frac{\partial \beta}{\partial T_{\inf}}\right) + \frac{\partial T}{\partial \beta}\frac{\partial \beta}{\partial T_{\inf}} = 1$$

$$\frac{\partial T}{\partial t_1} = \frac{\partial T}{\partial T_o}\left(\frac{\partial T_o}{\partial \alpha}\frac{\partial \alpha}{\partial t_1} + \frac{\partial T_o}{\partial \gamma}\frac{\partial \gamma}{\partial t_1}\right) + \frac{\partial T}{\partial \alpha}\frac{\partial \alpha}{\partial t_1}$$

$$\frac{\partial T}{\partial t_2} = \frac{\partial T}{\partial T_o}\left(\frac{\partial T_o}{\partial \beta}\frac{\partial \beta}{\partial t_2} + \frac{\partial T_o}{\partial \alpha}\frac{\partial \alpha}{\partial t_2} + \frac{\partial T_o}{\partial \gamma}\frac{\partial \gamma}{\partial t_2}\right) + \frac{\partial T}{\partial \beta}\frac{\partial \beta}{\partial t_2} + \frac{\partial T}{\partial \alpha}\frac{\partial \alpha}{\partial t_2}$$

$$\frac{\partial T}{\partial x} = \frac{\alpha\left(T_o - \beta\right)\sinh\left(\alpha x\right)}{\cosh\left(\alpha L\right)}$$

$$\frac{\partial T}{\partial L} = \frac{\partial T}{\partial T_o}\frac{\partial T_o}{\partial L} - \frac{\alpha\left(T_o - \beta\right)\cosh\left(\alpha x\right)}{\cosh\left(\alpha L\right)}\tanh\left(\alpha L\right)$$

$$\frac{dR}{dt_2} = \frac{1}{k_2}$$

$$\frac{dq_o''}{dV} = \frac{2PV}{115^2}$$

$$\frac{\partial T}{\partial T_o} = \frac{\cosh(\alpha x)}{\cosh(\alpha L)}$$

$$\frac{\partial T_o}{\partial \beta} = \frac{\alpha \tanh(\alpha L)}{\gamma + \alpha \tanh(\alpha L)}$$

$$\frac{\partial T_o}{\partial T_{\inf}} = \frac{\gamma}{\gamma + \alpha \tanh(\alpha L)}$$

$$\frac{\partial T_o}{\partial \alpha} = \left(\tanh(\alpha L) + \alpha L \operatorname{sech}^2(\alpha L)\right) \frac{(\beta - T_{\inf})\gamma}{\left(\gamma + \alpha \tanh(\alpha L)\right)^2}$$

$$\frac{\partial T_o}{\partial \gamma} = \frac{\alpha (T_{\inf} - \beta) \tanh(\alpha L)}{2\left(\gamma + \alpha \tanh(\alpha L)\right)^2}$$

$$\frac{\partial T_o}{\partial L} = \left(\alpha \operatorname{sech}^2(\alpha L)\right) \frac{(\beta - T_{\inf})\gamma}{\left(\gamma + \alpha \tanh(\alpha L)\right)^2}$$

$$\frac{\partial T}{\partial \beta} = 1 - \frac{\cosh(\alpha x)}{\cosh(\alpha L)}$$

$$\frac{\partial \beta}{\partial T_{\inf}} = 1$$

$$\frac{\partial \beta}{\partial R} = q''_o$$

$$\frac{\partial \beta}{\partial t_2} = \frac{\partial \beta}{\partial R} \frac{\partial R}{\partial t_2}$$

$$\frac{\partial \beta}{\partial V} = \frac{\partial \beta}{\partial q''_o} \frac{\partial q''_o}{\partial V}$$

$$\frac{\partial T}{\partial \alpha} = \frac{(T_o - \beta)}{\cosh^2(\alpha L)} \left[x \cosh(\alpha L) \sinh(\alpha x) - L \cosh(\alpha x) \sinh(\alpha L) \right]$$

$$\frac{\partial \alpha}{\partial R} = -\frac{1}{2} \frac{\alpha}{R}$$

$$\frac{\partial \alpha}{\partial t_2} = \frac{\partial \alpha}{\partial R} \frac{dR}{dt_2}$$

$$\frac{\partial \alpha}{\partial t_1} = -\frac{1}{2} \frac{\alpha}{t_1}$$

Fin Region: (only new equations from those above)

$$\frac{\partial T}{\partial V} = \frac{\partial T}{\partial T_o}\frac{\partial T_o}{\partial \beta}\frac{\partial \beta}{\partial V}$$

$$\frac{\partial T}{\partial T_{\inf}} = \frac{\partial T}{\partial T_o}\left(\frac{\partial T_o}{\partial T_{\inf}} + \frac{\partial T_o}{\partial \beta}\frac{\partial \beta}{\partial T_{\inf}}\right) + 1 - \mathrm{e}^{-\gamma(x-L)} = 1$$

$$\frac{\partial T}{\partial t_1} = \frac{\partial T}{\partial T_o}\left(\frac{\partial T_o}{\partial \alpha}\frac{\partial \alpha}{\partial t_1} + \frac{\partial T_o}{\partial \gamma}\frac{\partial \gamma}{\partial t_1}\right) + \frac{\partial T}{\partial \gamma}\frac{\partial \gamma}{\partial t_1}$$

$$\frac{\partial T}{\partial t_2} = \frac{\partial T}{\partial T_o}\left(\frac{\partial T_o}{\partial \beta}\frac{\partial \beta}{\partial t_2} + \frac{\partial T_o}{\partial \alpha}\frac{\partial \alpha}{\partial t_2} + \frac{\partial T_o}{\partial \gamma}\frac{\partial \gamma}{\partial t_2}\right) + \frac{\partial T}{\partial \gamma}\frac{\partial \gamma}{\partial t_2}$$

$$\frac{\partial T}{\partial x} = -\left(T_o - T_{\inf}\right)\gamma\,\mathrm{e}^{-\gamma(x-L)}$$

$$\frac{\partial T}{\partial L} = \frac{\partial T}{\partial T_o}\frac{\partial T_o}{\partial L} + \left(T_o - T_{\inf}\right)\gamma\,\mathrm{e}^{-\gamma(x-L)}$$

$$\frac{\partial T}{\partial T_o} = \mathrm{e}^{-\gamma(x-L)}$$

$$\frac{\partial T}{\partial \gamma} = -\left(T_o - T_{\inf}\right)\left(x - L\right)\mathrm{e}^{-\gamma(x-L)}$$

$$\frac{\partial \gamma}{\partial R} = -\frac{1}{2}\frac{\gamma}{R}$$

$$\frac{\partial \gamma}{\partial t_2} = \frac{\partial \gamma}{\partial R}\frac{dR}{dt_2}$$

$$\frac{\partial \gamma}{\partial t_1} = -\frac{1}{2}\frac{\gamma}{t_1}$$

Cylindrical Coordinates:

$$dT = \sqrt{\left(\frac{\partial T}{\partial V}dV\right)^2 + \left(\frac{\partial T}{\partial T_{\inf}}dT_{\inf}\right)^2 + \left(\frac{\partial T}{\partial t_1}dt_1\right)^2 + \left(\frac{\partial T}{\partial t_2}dt_2\right)^2 + \left(\frac{\partial T}{\partial r}dr\right)^2 + \left(\frac{\partial T}{\partial L}dL\right)^2}$$

Heated Region:

$$\frac{\partial T}{\partial V} = \frac{\partial T}{\partial T_o}\frac{\partial T_o}{\partial \beta}\frac{\partial \beta}{\partial V} + \frac{\partial T}{\partial \beta}\frac{\partial \beta}{\partial V}$$

$$\frac{\partial T}{\partial T_{\inf}} = \frac{\partial T}{\partial T_o}\left(\frac{\partial T_o}{\partial T_{\inf}} + \frac{\partial T_o}{\partial \beta}\frac{\partial \beta}{\partial T_{\inf}}\right) + \frac{\partial T}{\partial \beta}\frac{\partial \beta}{\partial T_{\inf}} = 1$$

$$\frac{\partial T}{\partial t_1} = \frac{\partial T}{\partial T_o}\left(\frac{\partial T_o}{\partial \alpha}\frac{\partial \alpha}{\partial t_1} + \frac{\partial T_o}{\partial \gamma}\frac{\partial \gamma}{\partial t_1}\right) + \frac{\partial T}{\partial \alpha}\frac{\partial \alpha}{\partial t_1}$$

$$\frac{\partial T}{\partial t_2} = \frac{\partial T}{\partial T_o}\left(\frac{\partial T_o}{\partial \beta}\frac{\partial \beta}{\partial t_2} + \frac{\partial T_o}{\partial \alpha}\frac{\partial \alpha}{\partial t_2} + \frac{\partial T_o}{\partial \gamma}\frac{\partial \gamma}{\partial t_2}\right) + \frac{\partial T}{\partial \beta}\frac{\partial \beta}{\partial t_2} + \frac{\partial T}{\partial \alpha}\frac{\partial \alpha}{\partial t_2}$$

$$\frac{\partial T}{\partial r} = \alpha\left(T_o - \beta\right)\frac{\mathrm{I}_1\left(\alpha r\right)}{\mathrm{I}_0\left(\alpha L\right)}$$

$$\frac{\partial T}{\partial L} = \frac{\partial T}{\partial T_o}\frac{\partial T_o}{\partial L} - \frac{\alpha\left(T_o - \beta\right)\mathrm{I}_0\left(\alpha r\right)\mathrm{I}_1\left(\alpha L\right)}{\mathrm{I}_0\left(\alpha L\right)^2}$$

$$\frac{dR}{dt_2} = \frac{1}{k_2}$$

$$\frac{dq_o''}{dV} = \frac{2PV}{115^2}$$

$$\frac{\partial T}{\partial T_o} = \frac{\mathrm{I}_0(ar)}{\mathrm{I}_0(aL)}$$

$$\frac{\partial T_o}{\partial \beta} = \frac{\alpha \mathrm{I}_1(\alpha L)\mathrm{K}_0(\gamma L)}{\alpha \mathrm{I}_1(\alpha L)\mathrm{K}_0(\gamma L) + \gamma \mathrm{K}_1(\gamma L)\mathrm{I}_0(\alpha L)}$$

$$\frac{\partial T_o}{\partial T_{\inf}} = \frac{\gamma \mathrm{K}_1(\gamma L)\mathrm{I}_0(\alpha L)}{\alpha \mathrm{I}_1(\alpha L)\mathrm{K}_0(\gamma L) + \gamma \mathrm{K}_1(\gamma L)\mathrm{I}_0(\alpha L)}$$

$$\frac{\partial T_o}{\partial \alpha} = \frac{\gamma(\beta - T_{\inf})\mathrm{K}_0(\gamma L)\mathrm{K}_1(\gamma L)\left[\mathrm{I}_0(\alpha L)\left(\frac{\alpha L}{2}\left(\mathrm{I}_0(\alpha L) + \mathrm{I}_2(\alpha L)\right) + \mathrm{I}_1(\alpha L)\right) - \alpha L \mathrm{I}_1(\alpha L)^2\right]}{\left(\alpha \mathrm{I}_1(\alpha L)\mathrm{K}_0(\gamma L) + \gamma \mathrm{K}_1(\gamma L)\mathrm{I}_0(\alpha L)\right)^2}$$

$$\frac{\partial T_o}{\partial \gamma} = -\frac{\alpha(\beta - T_{\inf})\mathrm{I}_0(\alpha L)\mathrm{I}_1(\alpha L)\left[\gamma L \mathrm{K}_1(\gamma L)^2 + \mathrm{K}_0(\gamma L)\left(\mathrm{K}_1(\gamma L) - \frac{\gamma L}{2}\left(\mathrm{K}_0(\gamma L) + \mathrm{K}_2(\gamma L)\right)\right)\right]}{\left(\alpha \mathrm{I}_1(\alpha L)\mathrm{K}_0(\gamma L) + \gamma \mathrm{K}_1(\gamma L)\mathrm{I}_0(\alpha L)\right)^2}$$

$$\frac{\partial T_o}{\partial L} = \frac{\alpha\gamma(\beta - T_{\inf})\left[\begin{array}{l}\mathrm{K}_1(\gamma L)\mathrm{I}_0(\alpha L)\left(\frac{\alpha}{2}\mathrm{K}_0(\gamma L)\left(\mathrm{I}_0(\alpha L) + \mathrm{I}_2(\alpha L)\right) - \gamma \mathrm{K}_1(\gamma L)\mathrm{I}_1(\alpha L)\right) \\ -\mathrm{I}_1(\alpha L)\mathrm{K}_0(\gamma L)\left(\alpha \mathrm{K}_1(\gamma L)\mathrm{I}_1(\alpha L) - \frac{\gamma}{2}\mathrm{I}_0(\alpha L)\left(\mathrm{K}_0(\gamma L) + \mathrm{K}_2(\gamma L)\right)\right)\end{array}\right]}{\left(\alpha \mathrm{I}_1(\alpha L)\mathrm{K}_0(\gamma L) + \gamma \mathrm{K}_1(\gamma L)\mathrm{I}_0(\alpha L)\right)^2}$$

$$\frac{\partial T}{\partial \beta} = 1 - \frac{\mathrm{I}_0(\alpha r)}{\mathrm{I}_0(\alpha L)}$$

$$\frac{\partial \beta}{\partial T_{\inf}} = 1$$

$$\frac{\partial \beta}{\partial R} = q_o''$$

$$\frac{\partial \beta}{\partial t_2} = \frac{\partial \beta}{\partial R}\frac{\partial R}{\partial t_2}$$

$$\frac{\partial \beta}{\partial V} = \frac{\partial \beta}{\partial q_o''}\frac{\partial q_o''}{\partial V}$$

$$\frac{\partial T}{\partial \alpha} = \frac{(T_o - \beta)}{\mathrm{I}_0(\alpha L)^2}\left[r \mathrm{I}_0(\alpha L)\mathrm{I}_1(\alpha r) - L \mathrm{I}_0(\alpha r)\mathrm{I}_1(\alpha L)\right]$$

$$\frac{\partial \alpha}{\partial R} = -\frac{\alpha}{2R}$$
$$\frac{\partial \alpha}{\partial t_2} = \frac{\partial \alpha}{\partial R}\frac{dR}{dt_2}$$
$$\frac{\partial \alpha}{\partial t_1} = -\frac{\alpha}{2t_1}$$

Fin Region: (only new equations from those above)

$$\frac{\partial T}{\partial V} = \frac{\partial T}{\partial T_o}\frac{\partial T_o}{\partial \beta}\frac{\partial \beta}{\partial V}$$
$$\frac{\partial T}{\partial T_{\inf}} = \frac{\partial T}{\partial T_o}\left(\frac{\partial T_o}{\partial T_{\inf}} + \frac{\partial T_o}{\partial \beta}\frac{\partial \beta}{\partial T_{\inf}}\right) + 1 - \frac{\mathrm{K}_0(\gamma r)}{\mathrm{K}_0(\gamma L)} = 1$$
$$\frac{\partial T}{\partial t_1} = \frac{\partial T}{\partial T_o}\left(\frac{\partial T_o}{\partial \alpha}\frac{\partial \alpha}{\partial t_1} + \frac{\partial T_o}{\partial \gamma}\frac{\partial \gamma}{\partial t_1}\right) + \frac{\partial T}{\partial \gamma}\frac{\partial \gamma}{\partial t_1}$$
$$\frac{\partial T}{\partial t_2} = \frac{\partial T}{\partial T_o}\left(\frac{\partial T_o}{\partial \beta}\frac{\partial \beta}{\partial t_2} + \frac{\partial T_o}{\partial \alpha}\frac{\partial \alpha}{\partial t_2} + \frac{\partial T_o}{\partial \gamma}\frac{\partial \gamma}{\partial t_2}\right) + \frac{\partial T}{\partial \gamma}\frac{\partial \gamma}{\partial t_2}$$
$$\frac{\partial T}{\partial r} = -\gamma(T_o - T_{\inf})\frac{\mathrm{K}_1(\gamma r)}{\mathrm{K}_0(\gamma L)}$$
$$\frac{\partial T}{\partial L} = \frac{\partial T}{\partial T_o}\frac{\partial T_o}{\partial L} + \frac{\gamma(T_o - T_{\inf})\mathrm{K}_0(\gamma r)\mathrm{K}_1(\gamma L)}{\mathrm{K}_0(\gamma L)^2}$$

$$\frac{\partial T}{\partial T_o} = \frac{\mathrm{K}_0(\gamma r)}{\mathrm{K}_0(\gamma L)}$$

$$\frac{\partial T}{\partial \gamma} = -\frac{(T_o - T_{\inf})}{\mathrm{K}_0(\gamma L)^2}\left[r\,\mathrm{K}_0(\gamma L)\mathrm{K}_1(\gamma r) - L\,\mathrm{K}_0(\gamma r)\mathrm{K}_1(\gamma L)\right]$$

$$\frac{\partial \gamma}{\partial R} = -\frac{\gamma}{2R}$$
$$\frac{\partial \gamma}{\partial t_2} = \frac{\partial \gamma}{\partial R}\frac{dR}{dt_2}$$
$$\frac{\partial \gamma}{\partial t} = -\frac{\gamma}{2t}$$

Figures:

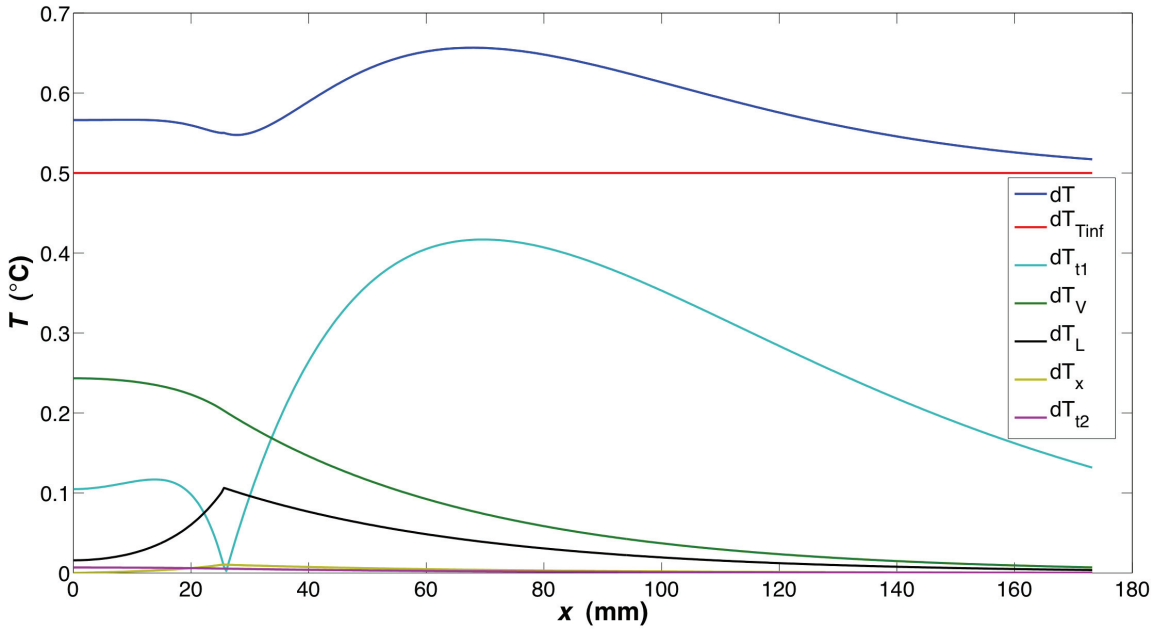

Figure B-1: Error propagation analysis for *T* in the Cartesian two-region fin model. Result shown for *L* = 25.4 mm, 0.059 W cm^{-2}, and natural convection.

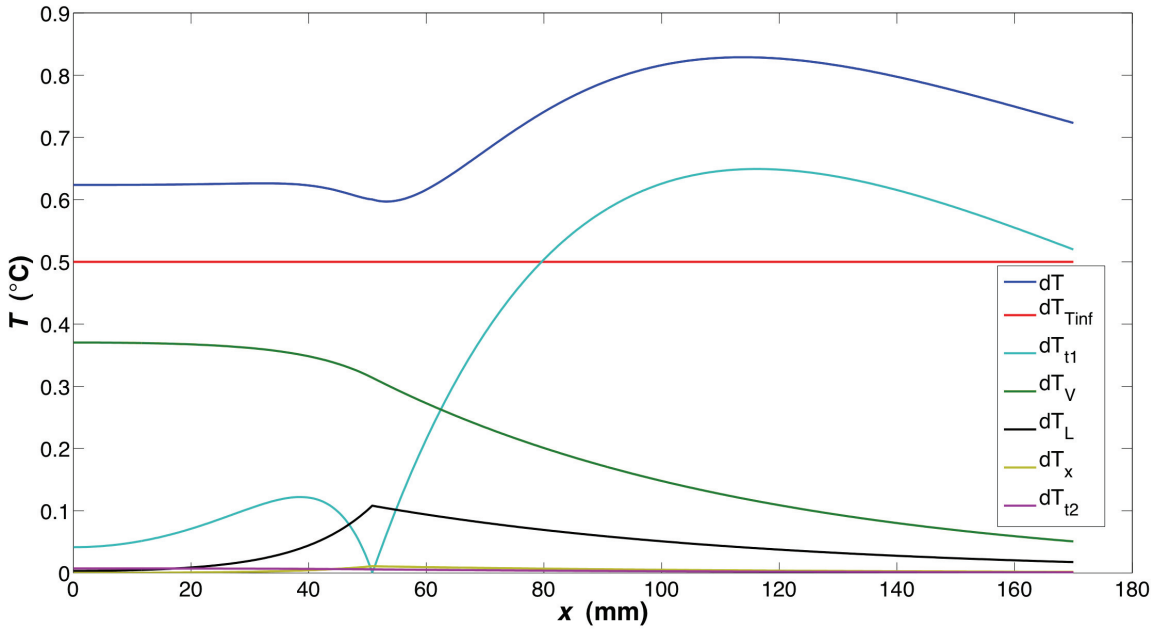

Figure B-2: Error propagation analysis for *T* in the Cartesian two-region fin model. Result shown for *L* = 50.8 mm, 0.059 W cm^{-2}, and natural convection.

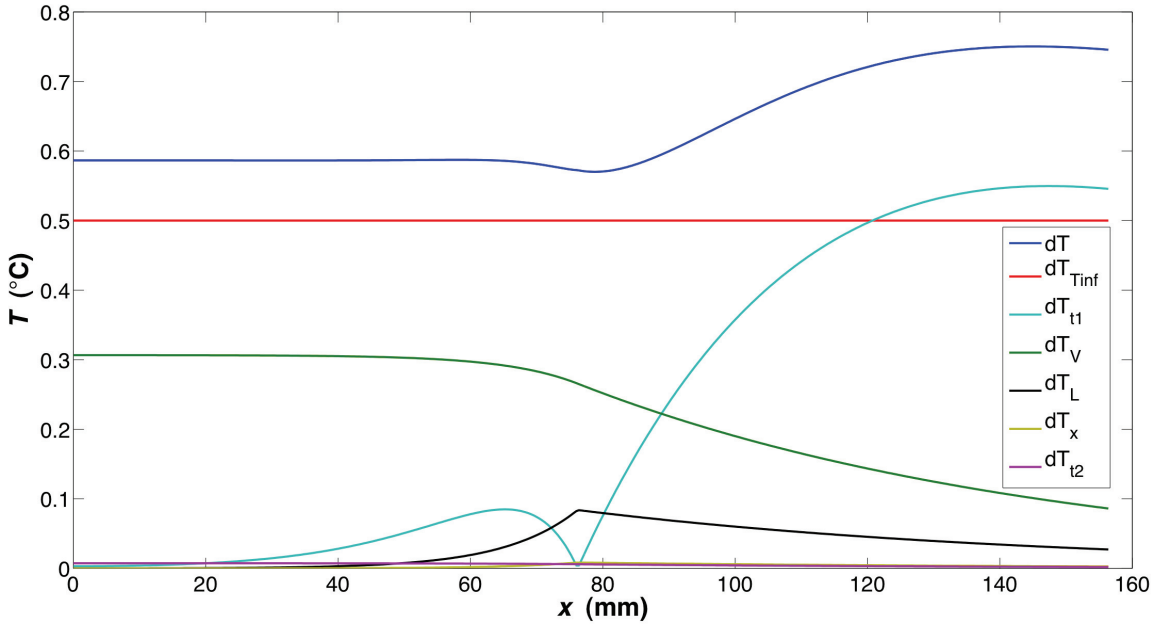

Figure B-3: Error propagation analysis for *T* in the Cartesian two-region fin model. Result shown for *L* = 76.2 mm, 0.059 W cm^{-2}, and natural convection.

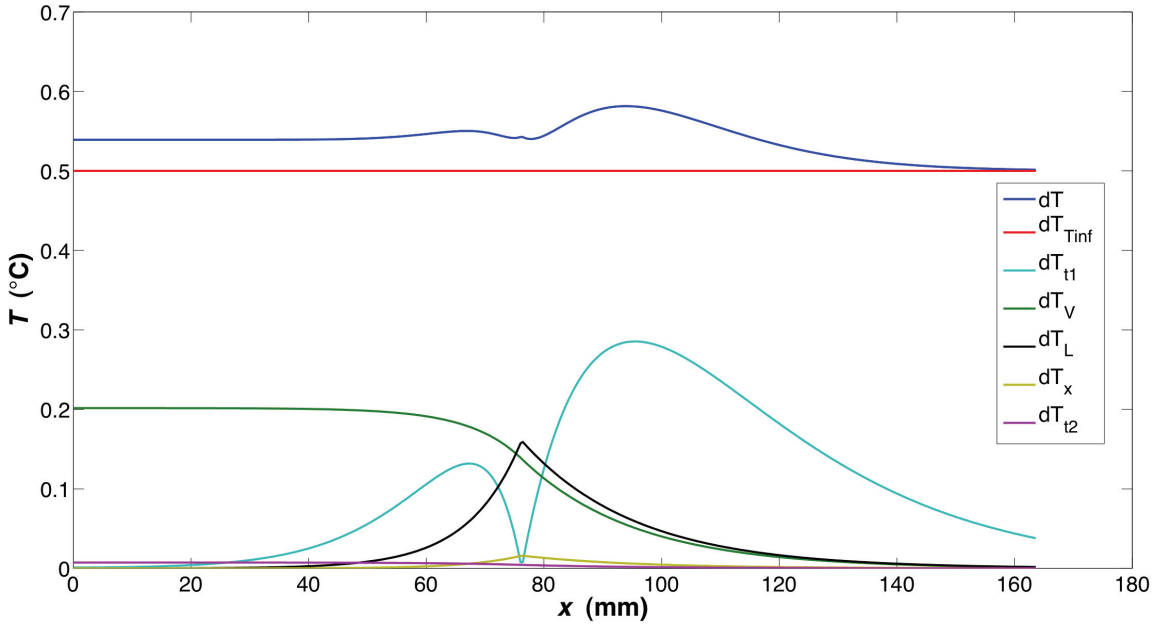

Figure B-4: Error propagation analysis for *T* in the Cartesian two-region fin model. Result shown for *L* = 76.2 mm, 0.059 W cm^{-2}, and external forced convection.

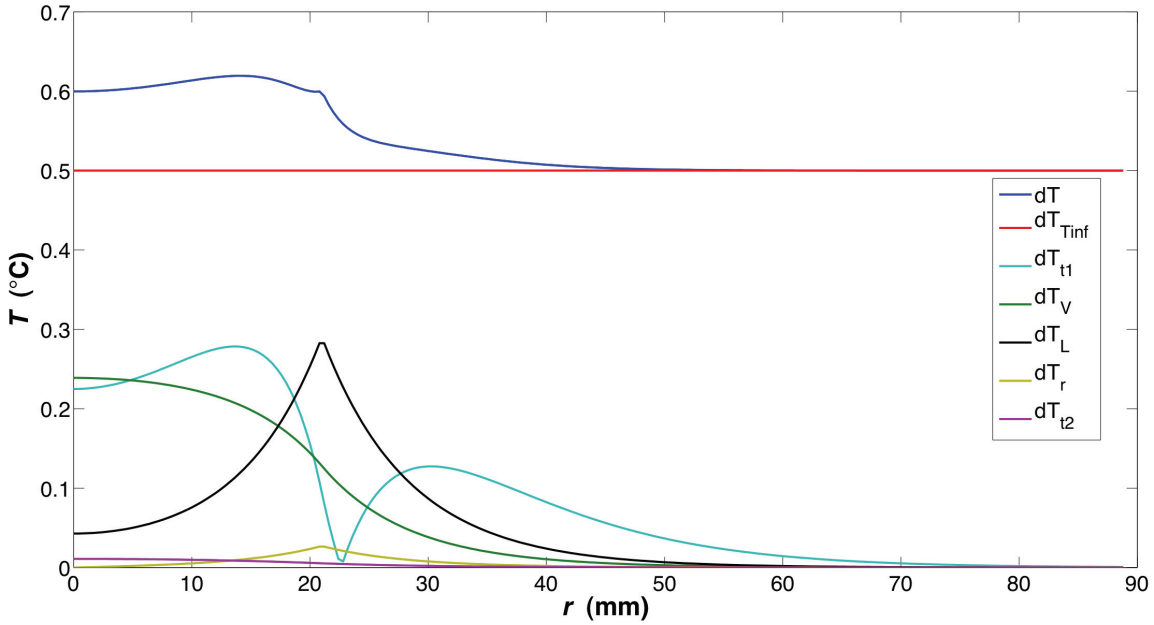

Figure B-5: Error propagation analysis for *T* in the cylindrical two-region fin model. Result shown for 2*L* = 50.8 mm, 0.11 W cm^{-2}, and external forced convection.

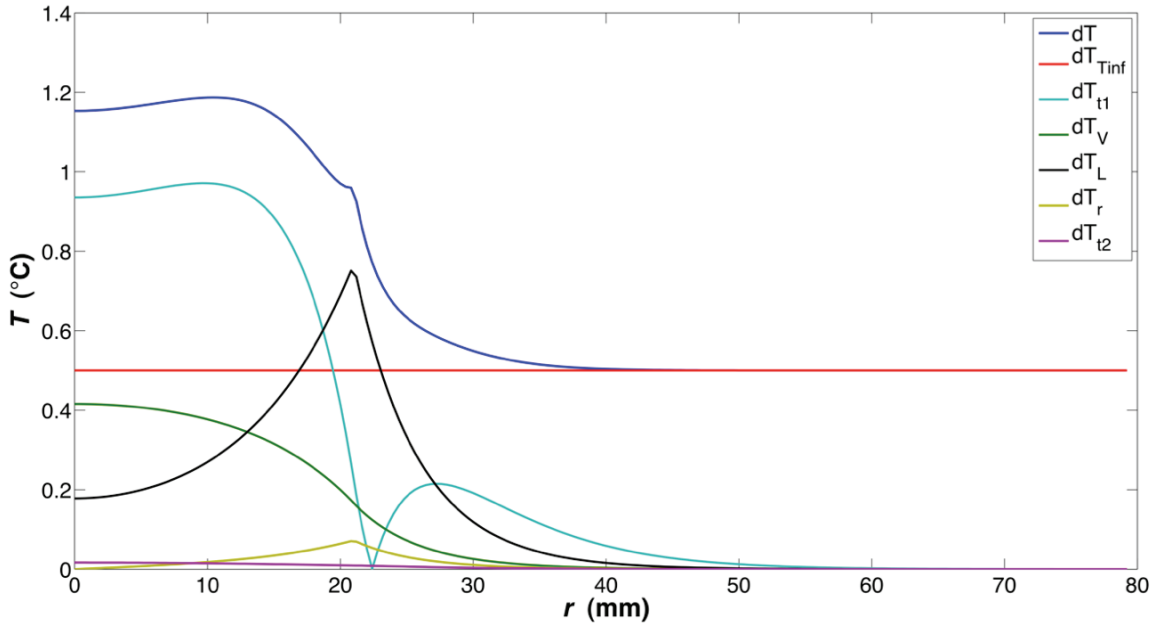

Figure B-6: Error propagation analysis for *T* in the cylindrical two-region fin model. Result shown for 2*L* = 50.8 mm, 0.19 W cm^{-2}, and external forced convection.

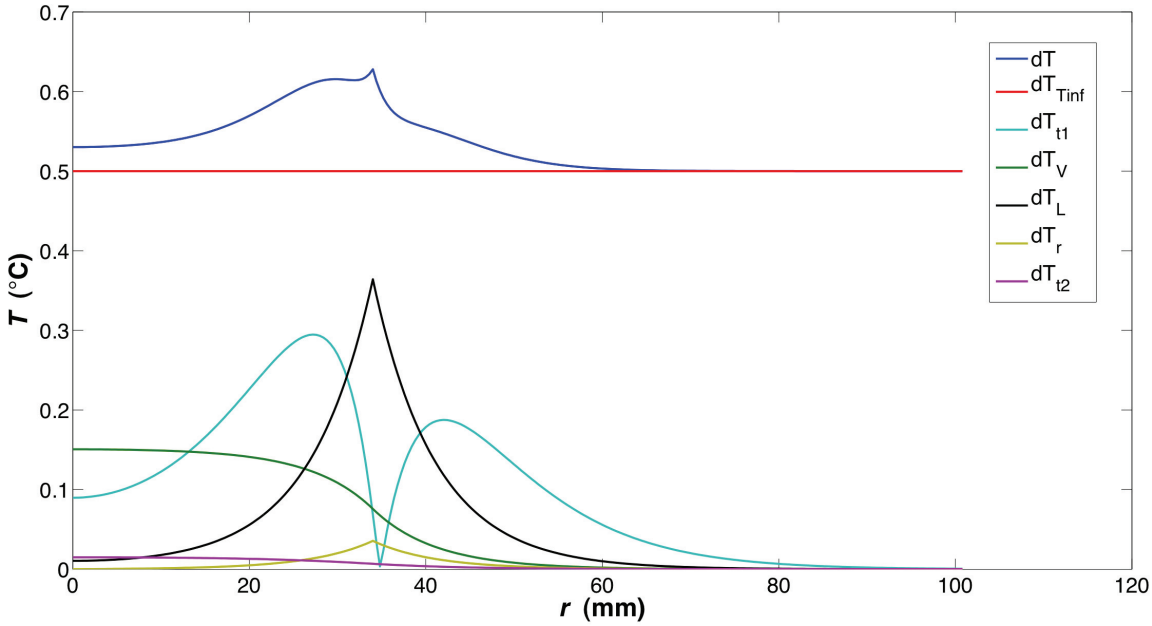

Figure B-7: Error propagation analysis for *T* in the cylindrical two-region fin model. Result shown for 2*L* = 76.2 mm, 0.12 W cm^{-2}, and external forced convection.

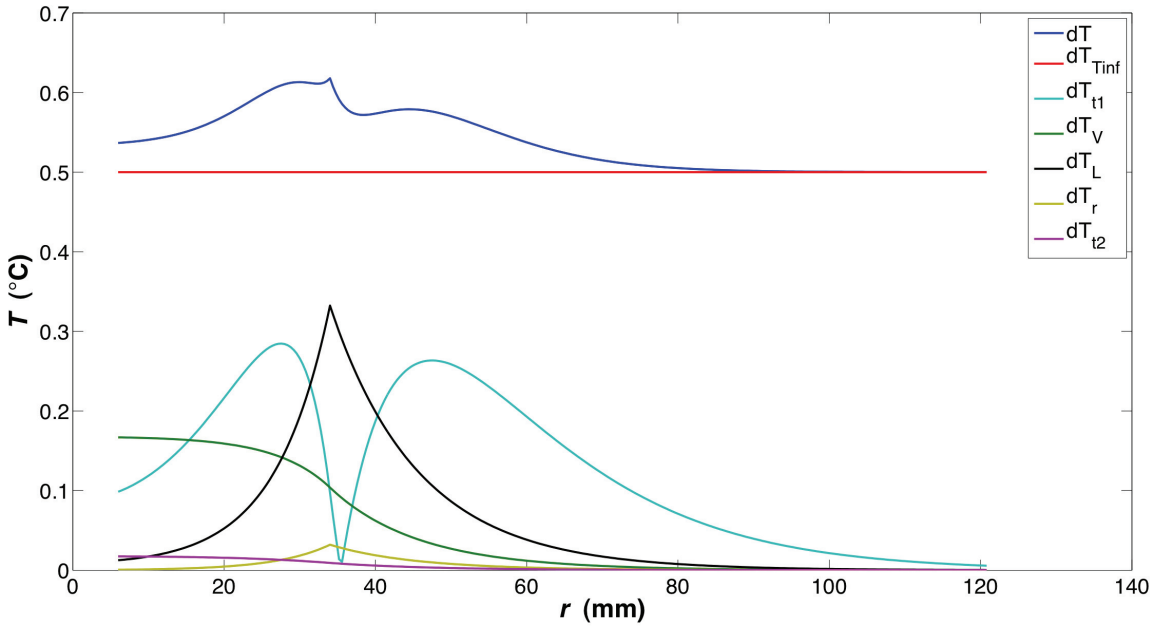

Figure B-8: Error propagation analysis for *T* in the cylindrical two-region fin model. Result shown for 2*L* = 76.2 mm, 0.14 W cm^{-2}, and external forced convection.

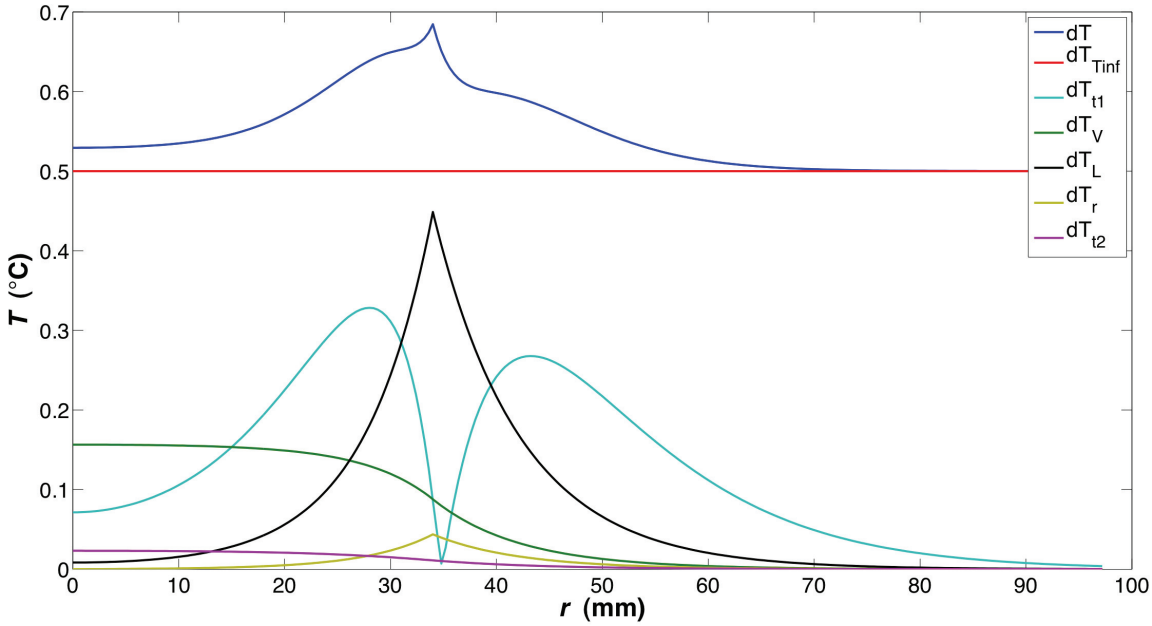

Figure B-9: Error propagation analysis for *T* in the cylindrical two-region fin model. Result shown for 2*L* = 76.2 mm, 0.19 W cm^{-2}, and external forced convection.